IMETUM

Zentralinstitut für Medizintechnik
Technische Universität München

Dissertation

David Johannes Scholz

Quantified pH Imaging via Nuclear Magnetic Resonance and Hyperpolarized ^{13}C-Bicarbonate Dissolution Dynamic Nuclear Polarization

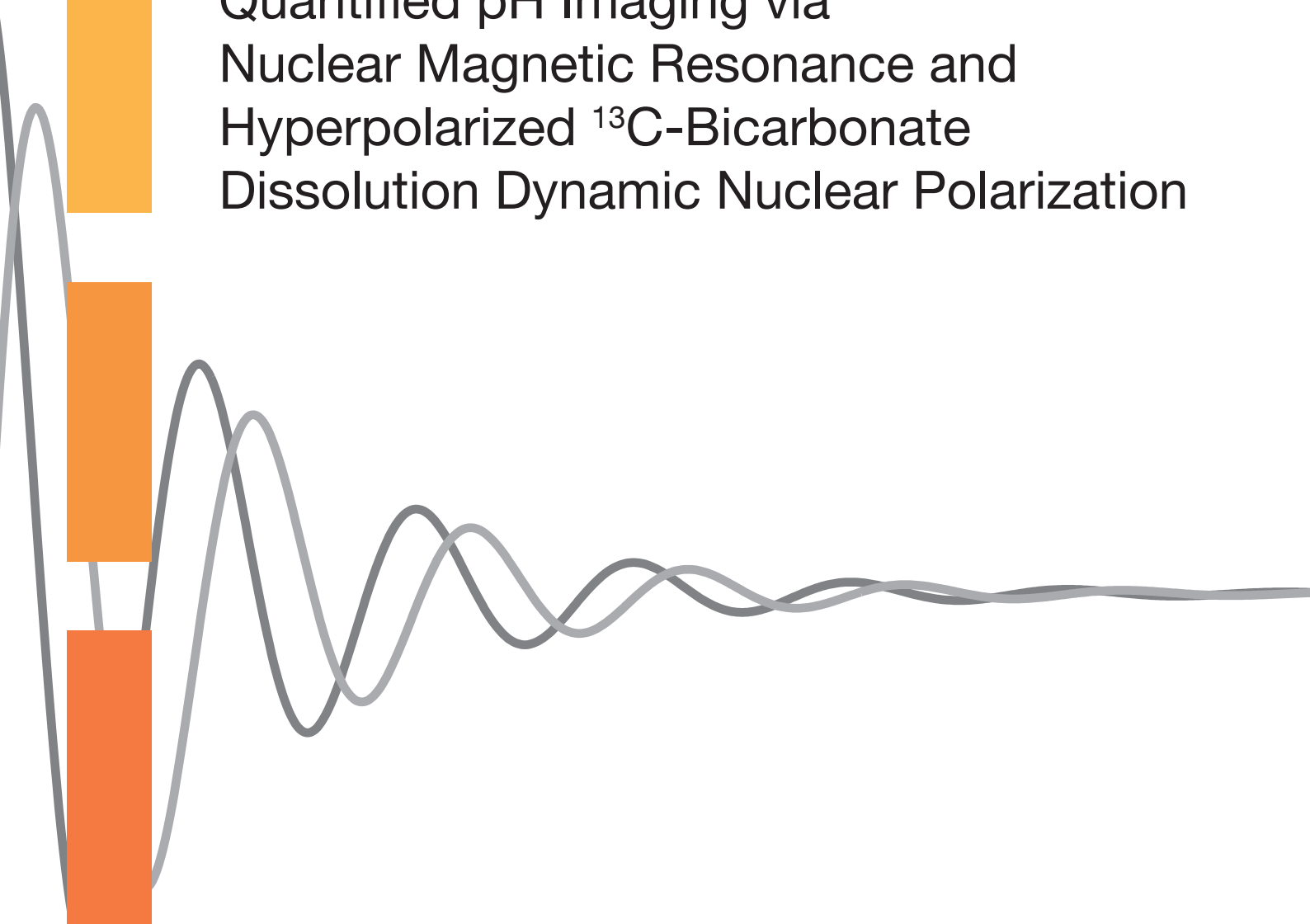

27. November 2014

Physik Department

Zentralinstitut für Medizintechnik

Quantified pH Imaging via Nuclear Magnetic Resonance and Hyperpolarized ^{13}C-Bicarbonate Dissolution Dynamic Nuclear Polarization

David Johannes Scholz

Vollständiger Abdruck der, von der Fakultät für Physik der Technischen Universität München zur Erlangung des akademischen Grades eines

Doktors der Naturwissenschaften (Dr. rer. nat.),

genehmigten Dissertation.

Vorsitzender:		Univ.-Prof. Dr. J. Leo van Hemmen
Prüfer der Dissertation:	1.	Univ.-Prof. Dr. Axel Haase
	2.	Univ.-Prof. Dr. Franz Pfeiffer

Die Dissertation wurde am 27.11.2014 bei der Technischen Universität München eingereicht und durch die Fakultät für Physik am 25.03.2015 angenommen.

Abstract

Magnetic resonance imaging (MRI) is a versatile and powerful tool to access a wide range of physical and biochemical properties and obtain relevant medical conclusions. Based on proton imaging, the method has undergone continuous development and presently, other magnetically active nuclei can be used for imaging. The breakthrough for non-proton nuclear magnetic resonance (NMR) imaging was achieved in 2003 with the development of "dissolution DNP" (dynamic nuclear polarization), which allows the hyperpolarization of ^{13}C-carbons and other magnetically active nuclei and the subsequent transition into a dissolved state without losing the enhanced signal intensities. Thereafter, biologically relevant molecules, such as pyruvate, alanine, and acetate, could be carbon-13 labeled, hyperpolarized, injected, and observed *in vivo* in an NMR imaging system. The non-invasive acquisition allows the observation of the distribution and metabolic conversion of the labeled molecules *in vivo* and therefore the characterization of diverse disorders, e.g., cancerogenous tissue. The development of different hyperpolarizable molecules led to the development of ^{13}C-bicarbonate as an *in vivo* pH marker in 2008. Although alteration of pH come along with disorders like tumors, alkalosis/acidosis, and inflammations, no clinical tool has yet been established to detect spatially resolved pH distributions in a non-invasive manner. pH detection via hyperpolarized ^{13}C-bicarbonate is highly signal-to-noise ratio (SNR) limited, which has thus far prevented a broader application of the technique.

In this work, the method was investigated and systematically improved in order to enhance the limited *in vivo* signal of the hyperpolarized ^{13}C-bicarbonate and create a robust method for pH imaging. The development process begins with theoretical simulations and quantifications of the sensitivity and proceeds to the chemically optimized conditioning of the sample and signal-optimized excitation pulses and acquisition techniques. This approach sufficiently improved the method's robustness, so that preclinical pH imaging at a clinical 3 T scanner could be performed. First, spatial *in vitro* pH distributions were measured, and the spatial distributions of hyperpolarized ^{13}C-bicarbonate in rat organs were determined. Subsequently, pH maps of acute metabolic alkalosis and induced sterile inflammations could be detected.

The optimization of the method provides a robust tool for future application in clinical pH imaging with non-invasive magnetic resonance tomography.

Zusammenfassung

Die Magnetresonanztomographie (MRT) ist ein vielseitiges und leistungsstarkes Werkzeug um unterschiedliche physikalische und biochemische Informationen zu gewinnen und medizinisch relevante Rückschlüsse daraus zu ziehen. Die grundsätzliche Methode der Protonenbildgebung wurde im Laufe der Jahre kontinuierlich weiter entwickelt, so dass heutzutage auch andere, magnetisch aktive Kerne zur Bildgebung genutzt werden können. Der Durchbruch der nicht Proton basierenden NMR gelang 2003 mit der Methode der sog. „Dissolution-DNP“ (engl.: dynamic nuclear polarization), die es ermöglicht ^{13}C-Kohlenstoffe, aber auch andere magnetisch aktive Kerne, zu hyperpolarisieren und in Lösung zu bringen, ohne dass die verstärkten Signalintensitäten verloren gehen. Von da an konnten biologisch relevante Moleküle wie z.B. Pyruvat, Alanin und Acetat markiert, hyperpolarisiert, injiziert und im Kernspintomographen räumlich dargestellt werden. Nicht-invasive Aufnahmen der markierten Moleküle erlauben es Verteilung und metabolische Konversion im Organismus zu verfolgen und so unterschiedliche Krankheiten, z.B. Tumorgewebe zu detektieren. Die Entwicklung unterschiedlicher hyperpolarisierbarer Moleküle führte 2008 zur Entwicklung von ^{13}C-Bicarbonat als Marker für die räumliche *in vivo* pH Verteilung. Obwohl verschiedene Krankheiten wie z.B. Tumore, Azidosen/Alkalosen und Entzündungen mit einem veränderten pH einhergehen, fehlen bisher in der klinischen Anwendung Werkzeuge, die den pH Wert nicht-invasiv und in räumlicher Verteilung darstellen können. Die Methode der pH Bildgebung mittels hyperpolarisiertem ^{13}C-Bicarbonat ist stark signalimitiert, was eine breite Anwendung bisher verhinderte.

In dieser Arbeit wird die Methode systematisch untersucht und verbessert um das bisher limitierte *in vivo* Signal des hyperpolarisierten ^{13}C-Bicarbonats zu verstärken und optimal zu nutzen um so eine robuste pH Bildgebung zu ermöglichen. Angefangen bei theoretischen Simulationen und Quantifizierung der Sensitivität, über die optimierte chemische Aufbereitung des Stoffes, bis hin zu signaloptimierten Anregungspulsen und Aufnahmetechniken wurde die Methode so weit verbessert, dass eine robuste präklinische pH Bildgebung an einem klinischen 3 T Kernspintomographen möglich ist. Zunächst wurde in *in vitro* Experimenten die räumliche pH Verteilung charakterisiert und die Verteilungen von hyperpolarisiertem ^{13}C-Bicarbonat in Organen gesunder Ratten gemessen. Anschließend konnten pH Verteilungen bei akuter metabolischer Alkalose und induzierte sterile Entzündung detektiert werden.

Die in dieser Arbeit optimierte Methode liefert ein robustes Werkzeug für zukünftige Anwendungen in der klinischen pH Bildgebung, mittels nicht invasiver Magnetresonanztomographie.

Contents

1. Introduction and motivation

The non-invasive method of nuclear magnetic resonance (NMR), either in the spectroscopic (MRS) but even more in the imaging domain (MRI), has evolved to be an indispensable tool in medical diagnostics. After the discovery of the quantum mechanical properties of nuclei in 1922 by *Stern* and *Gerlach* [1], the first spectroscopic applications developed by *Bloch* and *Purcell* [2,3] in 1946 were awarded the Nobel Prize in 1952. Subsequently, the method was mostly implemented for structural analysis of complex molecules. In 1973, *Mansfield* and *Lauterbur* [4,5] spatially encoded the acquired NMR information by varying magnetic field gradients and their work was recognized with the 2002 Nobel Prize. Thereafter, the promising method of spatial signal determination of *in vivo* compartments generated a vast variety of applied NMR techniques detecting a plethora of different parameters, including T_1-, T_2-, T_2^*-relaxations, blood flow, perfusion, brain activity and changes in diffusion. With the help of this previously inaccessible information, researchers were able to introduce new fields of diagnostics and improve treatment and therapy. Examples of the variety of novel medical imaging methods are the applications in the fields of diffusion and perfusion MRI [6,7], subsequently developed from this fast-acquisition real-time MRI of organs [8], and brain imaging applications with functional MRI (fMRI) [9,10]. The theoretical principles of NMR are described in chapter 2.1.1 followed by the advanced method of signal enhancement (chapter 2.1.2) the magnetization-preserving excitation method (chapter 2.1.3), and the frequency separation technique (chapter 2.1.4).

The developments in the field of hyperpolarization allow the *in vivo* detection of labeled molecules other than protons. Dissolution dynamic nuclear polarization (DNP) allows the following of pathways and conversion of the molecules directly and spatially resolved in time ranges, which cannot be observed by other methods [11,12]. NMR signals from ^{13}C-labeled molecules can be enhanced up to a factor of 10^4 and can be used to follow the distribution, metabolism, and conversion up to 120 seconds after injection. This technique constitutes the basis of the presented work, which uses hyperpolarized ^{13}C-bicarbonate to spatially measure pH *in vivo*.

pH functions as a key parameter in many important biochemical processes and its theoretical principles are presented in chapter 2.2.1. Electrochemical ionic gradients across cell membranes are established by different proton concentrations, which are used for ATP synthesis; this is the core of energy metabolism in any living system. Because many active cell-membrane transport mechanisms are dependent on the energy stored in the proton gradient, gradients of other ions are also dependent on proton gradients. Other fundamental biochemical mechanisms, like protein folding and enzymatic activities, are highly influenced by the proton concentration and, hence, pH. Thus, it is not surprising that alterations in pH are often associated with malignant changes in biological systems [13,14]. Therefore, it is desirable to detect pH *in vivo* because several disorders, like cancer, hypoxia, and

inflammation, show a direct influence by pH [15,16]. Since tumors benefit from the acidification of extracellular space in many ways, they acidify their direct extracellular environment due to the Warburg effect, which includes increased glycolytic activity, lactic acid production, and changes in perfusion [17-21]. Extracellular matrix degradation of healthy environmental tissue leads to available space, in which the tumor can proliferate [22,23]. Lower pH leads to increased angiogenesis [24,25] and tumor invasion [26] and helps the tumor to overcome cancer treatments, since many anti-cancer drugs are pH-sensitive [27]. To avoid self-damage, cancer cells have developed a higher resistance against acidic microenvironments [28].

Regarding non-invasive spectral pH determination, it is desirable to extend the method by the spatial dimension in order to obtain additional information. The ability to detect the pH distribution across a particular area of interest or determine regions of interest with respect to changes in pH has the potential to impact the diagnosis and therapy of tumors [29,30]. Most clinically established imaging modalities, e.g., fluorescence- [31], PET- [32-34], and magnetic resonance-based methods [35,36], endeavor to achieve spatial pH detection. Especially regarding MR, a variety of methods have been investigated [18]. Each method shows distinct advantages and limitations in signal-to-noise ratio (SNR), resolution, applicability, and pH-sensitivity; depending on the occurrence, *in vivo* distribution, and transport of the used tracer and nuclei, these methods are able to detect pH intracellularly, extracellularly, or both.

In ^{19}F magnetic resonance spectroscopy (MRS), the ^{19}F resonance allows the detection of intra- and extracellular pH by using a fluorinated vitamin B6 derivative [37]. ^{31}P MRS allows the detection of the resonance of inorganic phosphate ($^{31}P_i$), which mainly reflects intracellular pH [38,39]. To access extracellular pH, the pH-dependent chemical shifts of 3-aminopropylphosphate (3-APP) were measured in MCF-7 tumors in mice [40]. In ^{1}HMRS, MR spectroscopic imaging (MRSI) was used for the detection of the H_2 resonance of an imidazole compound (IEPA) leading to an extracellular pH estimation, which was subsequently confirmed for different cancer types *in vivo* [19,41,42]. In MR relaxometry, gadolinium-based contrast agents with a pH-dependent relaxivity were demonstrated to detect pH in kidneys [43,44] and rat brain glioma [45,46]. Very promising results with regard to high spatial resolution were achieved with chemical exchange saturation transfer (CEST) [47-49]. Here, local magnetization is depleted through an exchange of protons with bulk water [50], which allowed to map pH in murine melanoma models [51].

It has been shown that all these methods are capable of measuring pH. However, their main drawbacks are that they are inherently limited to preclinical imaging. This is mainly caused by the use of either toxic compounds or radiation, which does not allow any upscaling to larger targets. Additionally, they are dependent on the capability of correct concentration measurements of the used tracers.

A method introduced in 2008 by *Gallagher et al.* allows measuring pH *in vivo* using injected hyperpolarized bicarbonate, a non-toxic substance that naturally occurs in the body in high concentrations (25 mmol/L in blood), and is already applied in standard cancer treatment protocols [52]. The method is concentration-independent, since pH can be calculated just by

measuring the pH-dependent ratio of the signals of the ^{13}C-labeled bicarbonate and the formed $^{13}CO_2$. The pH determination is performed by using a derivation of the Henderson-Hasselbalch equation:

$$pH = pKa + log_{10}\frac{[HCO_3^-]}{[CO_2]}\ , \qquad (1)$$

where pKa (also known as pKs) is the negative decadic logarithm of the acidic dissociation constant and is assumed to be 6.17 *in vivo* [53,54]. Although the method has already been successfully applied on different targets [39,53,55], the overall number of publications using hyperpolarized ^{13}C-pH mapping is small and the quality of the acquired images in sensitivity and spatial resolution is low compared to ^{13}C-pyruvate, although many working groups have tried to establish the method for pH mapping.

The method is inherently limited by low SNR, even more than ^{13}C-pyruvate. The preparation and experimental procedures are not easily transferable from pyruvate-related work [56,57], owing to the impact of parameters such as pH and temperature. In the published work only minor attention has been thus far given to the systematic investigation of the method, including the preparation of the ^{13}C-bicarbonate and its influences during a hyperpolarized-dissolution DNP experiment with subsequent *in vitro* or *in vivo* application. The current absence of research on ^{13}C-bicarbonate pH mapping also concerns optimized nuclei excitation and signal acquisition, which is also addressed in this work. In order to increase the robustness of the method, it is necessary to systematically investigate the theoretical and practical limitations originating from all possible sources and push these limits to the maximum. The entire experimental procedure, ranging from the preparation of the compound to the execution of the dissolution DNP experiments, exhibits a variety of signal-depleting pitfalls that may reduce the hyperpolarized signal and, in turn, pH-mapping quality. Disregarding these influences leads to an increased signal attenuation, which is especially prohibitive in pH-imaging experiments, where $^{13}CO_2$ must be produced from ^{13}C-bicarbonate and subsequently imaged.

The scope of this work was to reevaluate bicarbonate pH mapping, starting with the optimization of the methodology (chapter 3) including the bicarbonate preparation (chapter 3.1), dissolution (chapter 3.2) and custom-tailored data analysis (chapter 3.3).

Subsequently, signal decay analysis was performed *in vitro* (chapter 4.1), including the study of different physical and chemical parameters. The development and application of novel MR acquisition techniques allows further signal preservation and the limits of the new acquisition techniques were investigated and quantified (chapter 4.2). After the method's optimization, the *in vivo* performance of bicarbonate and pH mapping was evaluated (chapter 4.3) and finally, pH mapping was performed for previously undetermined diseases (chapter 4.4).

2. Theory

Corresponding to the presented work, the theoretical background is divided into two major parts: The first part deals with physical background (chapter 2.1), the second part is focused on the biochemical background (chapter 2.2).

2.1. Physics

The physical background of this work is mainly founded on the principles of nuclear magnetic resonance (chapter 2.1.1). Subsequent advanced MR methods were used like hyperpolarization (chapter 2.1.2), spectral-spatial (SPSP) excitation (chapter 2.1.3) and IDEAL frequency separation (chapter 2.1.4).

2.1.1 Nuclear magnetic resonance

The principle of NMR is based on the splitting of the energy levels of magnetically active nuclides in an external magnetic field.
Otto Stern and *Walther Gerlach* showed in their Nobel prize-awarded experiment in 1922 the influence of quantum mechanic angular momentum [1] and its intrinsic quantized properties: A beam, consisting of silver particles was sent through an inhomogeneous magnetic field and subsequently deflected onto a photographic plate. In contrast to classical deflection, where the atoms should be homogenously distributed, the deflection pattern showed only two discrete distributions, indicating a quantized influence of the magnetic field to the atoms. This intrinsic quantum mechanic property was termed as *spin*.

2.1.1.1 *Spin*

Whether a nuclide is magnetically active or not is determined by the spin quantum number S, which is contributed to by the protons and the neutrons of the nuclide. The overall spin of a nuclide is composed by all components that have the intrinsic quantum property of spin (which are protons and neutrons, each with spin 1/2). S is ≠ 0, when the sum of the protons and neutrons (S=1/2) or both (S=1) is odd.
The nuclear spin angular momentum is defined as

$$\boldsymbol{S} = \hbar \boldsymbol{I} \quad (2)$$

where the reduced Planck's constant $\hbar = \frac{h}{2\pi}$ has been used. $\boldsymbol{I}$ is the spin operator for all spatial directions: $\boldsymbol{I} = (I_x, I_y, I_z)$. For a nuclear spin with quantum number I, the operator I_z shows 2I+1 eigenstates

$$\boldsymbol{I}^2|I,m\rangle = I(I+1)\hbar^2|I,m\rangle \quad (3)$$

$$\boldsymbol{I}_z|I,m\rangle = m\hbar|I,m\rangle \quad (4)$$

where the quantum number m can have quantized values of

$$m = -I, -I+1, \dots, I-1, +I \quad (5)$$

and I can have values of

$$I = 0, \frac{1}{2}, 1, \frac{3}{2}, \dots, 6 \quad (6)$$

in the case of a proton with $I = 1/2$. The magnetic moment μ is directly proportional to S, with:

$$\boldsymbol{\mu} = \gamma \boldsymbol{S} \quad (7)$$

γ is the gyromagnetic ratio, a nuclide-specific constant reflecting the sensitivity of the nucleus to an external magnetic field. When applying an external magnetic field in the z-direction, S_z shows whole- or half-integer multiples of Planck's constant:

$$S_z = m\hbar, \quad (8)$$

which leads to the magnetic moment in the z-direction:

$$\mu_z = \gamma m \hbar \quad (9)$$

2.1.1.2 *Zeeman effect*

The energy of a magnetic dipole in a homogenous magnetic field B_0 is given by:

$$E = -\mu B_0 = -\gamma m \hbar B_0 \quad (10)$$

Assuming a ½ -spin nuclide and a B_0 field in the z-direction, the energy levels split into:

$$E_{\pm\frac{1}{2}} = \pm\frac{1}{2}\gamma\hbar B_z \quad (11)$$

(see Figure 1) the magnetic moment of each nuclide precesses along the axis of the magnetic field with the Larmor frequency $\omega_0 = 2\pi\nu_0$, which reflects the resonance frequency of the nuclide and hence the crossover frequency between the energy levels

$$\Delta E = \gamma\hbar B_0 = \hbar\omega_0 \quad (12)$$

leading to a B_0-dependent Larmor frequency:

$$\omega_0 = \gamma B_0. \quad (13)$$

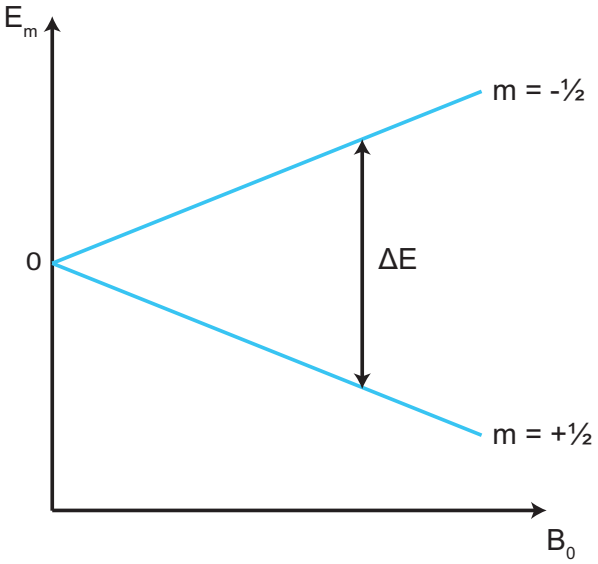

Figure 1: Splitting of the degenerate energy levels of a nucleus with (I=1/2) under the influence of a magnetic field B_0.

To transition between the two energy states, an external magnetic field B_1 is applied perpendicularly to B_0 with a Larmor frequency ω_0. For a proton with spin ½ and a magnetic field of strength 1 T, $\omega_0 = 42.6\ MHz$.

2.1.1.3 *Equilibrium and magnetization*

A spin ½ population N divides into a part with parallel orientation ($m = 1/2$), which is noted as $N_\uparrow$, and one with antiparallel orientation ($m = -1/2$), which is noted $N_\downarrow$, with respect to an applied external magnetic field B_0.

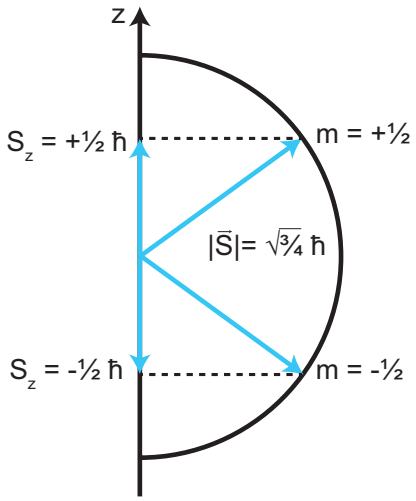

Figure 2: Quantization of the direction of the spin S of a nucleus I=1/2 in a homogenous magnetic field along the z-axis.

The orientation of the spins (see Figure 2) is dependent on the sign of the gyromagnetic ratio γ and directly proportional to the energy difference of the two Zeeman states. The ratio of the spin populations $N_\downarrow$ to $N_\uparrow$ is dependent on the temperature and follows the Boltzmann distribution:

$$\frac{N_\downarrow}{N_\uparrow} = e^{-\Delta E/k_B T} \qquad (14)$$

ΔE is usually orders of magnitude smaller than the thermal energy $E_{th} = k_B T$. However, applying a static magnetic field to a spin ensemble results in differences in the populations of the two energy states and hence a net magnetic moment M_0 in the direction of the magnetic field, which provides the signal that is obtained in a magnetic resonance experiment:

$$M_0 = N\frac{\gamma^2 \hbar^2 B_0 I(I+1)}{3k_B T} \qquad (15)$$

Assuming a magnetic field in the z-direction, there is only magnetization in the z-direction, M_z, whereas the transversal contributions in the x- and y-direction cancel out ($M_x = M_y = 0$).

2.1.1.4 *Bloch equation*

To simplify the description of this movement, *Felix Bloch* introduced in 1946 the equation of motion for macroscopic nuclear magnetization:

$$\frac{d\vec{M}}{dt} = \gamma(\vec{M}\times\vec{B}_{eff}) \quad (16)$$

This describes the change of the movement of the magnetization vector $\vec{M}$ in time when $\vec{B}_{eff} = \left(\vec{B}_0 + \frac{\omega_0}{\gamma}\right) + \vec{B}_1$ is the effective applied magnetic field. In a coordinate system rotating with the Larmor frequency ω_0, the contribution $\vec{B}_0 + \frac{\omega_0}{\gamma} = 0$, leading to $\vec{B}_{eff} = \vec{B}_1$. Hence, $\vec{B}_{eff}$ is only dependent on $\vec{B}_1$ as long as only $\vec{B}_0$ is applied. The application of a magnetic field $\vec{B}_1$ (e.g., a radio frequency pulse) that is perpendicular to $\vec{B}_0$ and oscillates with ω_0 leads to the rotation of $\vec{M}$. The angle of rotation α depends of the duration Δt of the irradiated field: $\alpha = \gamma\vec{B}_1\Delta t$. Therefore, different flip angles can be excited by using different RF irradiation times. Assuming that $\vec{B}_0$ in the z-direction results in a magnetization $\vec{M}_z$, maximum excitation is achieved with $\alpha = 90°$; thus, when irradiating the field $\vec{B}_1$ along the x-axis for $\Delta t = \frac{90°}{\gamma\vec{B}_1}$, the magnetization is rotated completely to $-\vec{M}_y$. The spin ensemble is equally distributed along the z-axis ($\vec{M}_z$ = 0) and shows phase coherence along the -y-axis. After the irradiation of the RF pulse, the system relaxes back to its thermodynamic equilibrium condition ($\vec{M} = \vec{M}_z, \vec{M}_{x,y} = 0$). This relaxation component is added to the Bloch equation (see equation (16)) to fully describe the movement of the magnetization:

$$\frac{d\vec{M}_x}{dt} = \gamma(\vec{M}\times\vec{B})_x - \frac{M_x}{T_2} \quad (17)$$

$$\frac{d\vec{M}_y}{dt} = \gamma(\vec{M}\times\vec{B})_y - \frac{M_y}{T_2} \quad (18)$$

$$\frac{d\vec{M}_z}{dt} = \gamma(\vec{M}\times\vec{B})_z - \frac{M_0 - M_z}{T_1} \quad (19)$$

The added terms describe the paramagnetic spin relaxation due to the interaction with the environment (spin-lattice relaxation, T_1) and with each other (spin-spin relaxation, T_2). Thus, the relaxation of the magnetization in each direction can be described as exponential decay for M_x, M_y:

$$M_x(t) = M_x(0)e^{\left(-\frac{t}{T_2}\right)} \quad (20)$$

$$M_y(t) = M_y(0)e^{\left(-\frac{t}{T_2}\right)} \quad (21)$$

and exponential convergence for M_z:

$$M_z(t) = M_z(0)e^{\left(-\frac{t}{T_1}\right)} + M_0(1 - e^{\left(-\frac{t}{T_1}\right)}) \quad (22)$$

where M_0 is the initial magnetization at thermal equilibrium. Due to susceptibility effects and field inhomogeneities, transversal relaxation is $T_2^* < T_2$ in real experiments.

2.1.1.5 *Magnetic resonance imaging*

Paul Lauterbur and *Peter Mansfield* introduced the basic principles of NMR signal detection in multiple spatial dimensions in 1973 [4,5] and they were rewarded for this work in 2003

with the Nobel Prize in physiology or medicine. The spatial determination of the NMR signal is possible owing to the application of an additional constant magnetic field gradient $\vec{G}(x,y,z)$. The additional field contributions impact the resonance frequencies in a spatially located manner (compare equation (13)):

$$\omega_0(r) = \gamma(B_0 + \vec{G}\cdot\vec{r}) = \gamma(B_0 + G_x\cdot x + G_y\cdot y + G_z\cdot z) \quad (23)$$

Hence, different resonance frequencies can be connected with different gradient strengths and can therefore be spatially localized, as the following one-dimensional example will show.
Applying a gradient G_z along B_0 in the z-direction:

$$G = \begin{pmatrix} 0 \\ 0 \\ G_z \end{pmatrix} \quad (24)$$

leads to an excitation of only spins at the corresponding position on the z-axis, since only spins of Larmor frequency:

$$\omega_0(z) = \gamma(B_0 + G_z\cdot z) \quad (25)$$

are excited. Because real pulses have a certain shape with a bandwidth $\Delta\omega$, a corresponding slice thickness can be excited with:

$$\Delta z = \frac{\Delta\omega}{\gamma\cdot G_z} \quad (26)$$

Owing to different Larmor frequencies originating from the z-gradient, excited spins can be located along the z-axis (see Figure 3). Any shifts or changes of the gradients lead to changing of the slice position and thus can be used to acquire and locate signals along the z-axis. This provides the name of the method: slice-selection.

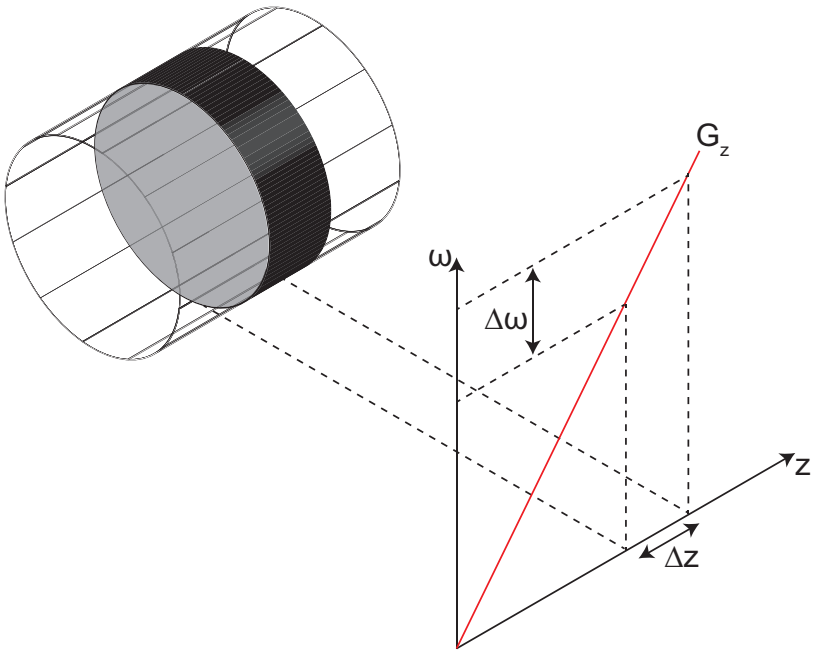

Figure 3: Slice selection using a gradient in the z-direction and the corresponding Larmor frequencies. The resonance frequencies change along the gradient, which allows them to separately excite spins within a frequency band $\Delta\omega$ and corresponding spatial slice thickness Δz.

To add the spatial encoding of the slice, additional gradients in the x- and y-directions must be applied perpendicularly to z-axis. The in-plane spin-density distribution $\rho(x, y)$ can be decomposed into individual spatially dependent frequency components. The signal intensity $S(t)$ is obtained by integrating the sum of the transverse magnetization over the entire slice:

$$S(t) = \iiint \rho(r) e^{i\gamma G r t}\, dr. \quad (27)$$

Introducing a reciprocal space vector k [58], which is the conjugate variable of the real space vector r:

$$k = \frac{\gamma G t}{2\pi} \quad (28)$$

allows to describe the signal intensity $S(k)$ as a Fourier transform (FT) of the spin-density distribution $\rho(r)$:

$$S(k_x, k_y) = \iint \rho(x, y) e^{i(k_x x + k_y y)}\, dx dy \quad (29)$$

$$\rho(x, y) = \iint S(k_x, k_y) e^{-i(k_x x + k_y y)}\, dk_x dk_y\,. \quad (30)$$

This allows to acquire an image by measuring the MR signal's k-space (k_x, k_y) and subsequently applying the inverse Fourier transformation to obtain the spin-density distribution in real space (x, y) [59]. Normally, this is performed by using a fast Fourier transformation (FFT) [60]. A proper filling of the k-space map is required, which can be realized by using frequency and/or phase encoding steps. Here, the Larmor frequencies of the spins are modified by a certain frequency or phase shift that allows the separation of the signal-contributing spins in all spatial directions.

Different readout trajectories can be used to fill and sample the k-space. Usually, Cartesian shapes are employed, but a plethora of more advanced shapes can also be used, like radial sampling and spirals. Those schemes exhibit a higher sampling density in the k-space center for time-efficient image acquisition owing to undersampling of the k-space with only a few encoding steps.

2.1.2 Hyperpolarization

According to equation (14), it is evident that spin populations are not equally distributed at thermal equilibrium. The excess of spins at one level is characterized by the polarization level P:

$$P = \frac{N_\uparrow - N_\downarrow}{N_\uparrow + N_\downarrow} \quad (31)$$

which can be written for thermal equilibrium as

$$P = tanh\left(\frac{\gamma \hbar B_0}{2 k_B T}\right) \quad (32)$$

with relation to the magnetic field B_0, temperature T, and Boltzmann constant k_B. The polarization level is directly connected to the magnetic moment of an ensemble of spins.

$$M = \frac{1}{2} N \gamma \hbar P \quad (33)$$

where N denotes the number of spins. The polarization level at $3\,T$ and at room temperature is $P = 10^{-6}$, which means that only 1 spin out of 1 million exceeds equilibrium. This low polarization level directly affects the measureable magnetic moment and is, assuming a constant number of spins, the only parameter that can enhance the net signal. Compared to other spectroscopic methods (e.g., optical methods) magnetic-resonance-based acquisition suffers in sensitivity because of this inherent limitation of low polarization. Since polarization is dependent on the magnetic field B_0, many efforts have been made in the past decades to increase the static magnetic field strength. However, the field strengths of standard clinical MRI scanners range from 0.5 to $3\,T$, whereas higher field strengths are limited to scientific scanners and spectroscopic systems. Thus, increasing the polarization level is the only way to increase the net magnetization and different techniques have been developed to increase the population of one spin state. Different techniques, like spin exchange optical pumping (SEOP) [61-69], parahydrogen-induced polarization (PHIP) [70-72], methods using high magnetic fields and low temperature [73,74], and dissolution DNP [11,12,75,76], can be used to increase the SNR.

In this work, the method of dissolution DNP was implemented to increase the polarization level of the investigated nucleus. This increase is essential because we need to observe the magnetic signal of ^{13}C-carbons instead of ^{1}H. Hydrogen is highly abundant in biological samples and fully present in the magnetically active form. In addition, protons have the highest gyromagnetic ratio ($42.576\,\frac{MHz}{T}$), thus leading to optimal conditions to antagonize the low inherent sensitivity of NMR. Observing ^{13}C-carbons is more difficult. In general, carbon concentrations are lower compared to protons and the magnetically active isotope ^{13}C shows a much lower abundance (1.1%). In addition, the gyromagnetic ratio of carbon is only a fourth of that of the proton ($10.705\,\frac{MHz}{T}$). This results in a massive reduction in sensitivity in an NMR measurement. Considering the low abundance and low γ, ^{13}C measurements only achieve 0.0176% of the sensitivity of a proton-NMR measurement.

The effect of DNP allows to enhance the sensitivity of a given nucleus in NMR/MRI and was first predicted for metals by *Albert Overhauser* in 1953 [77]. Later, *Carver* and *Slichter* experimentally confirmed *Overhauser's* assumptions [78]. For electrons in liquids, *Abgragam* and *Proctor* described the "solid effect" [79]. For low temperatures (<4 K), electron-spin polarization is more than three orders of magnitude larger ($\approx 100\%$), than nuclear spin polarization ($\approx 0.1\%$). This is caused by the larger gyromagnetic ratio of electrons ($28024.944\,\frac{MHz}{T}$). In addition, the relaxation of electrons is orders of magnitude faster ($T_{1,e} \approx 1\,ms$) than nuclear relaxation; this provides the opportunity to transfer the polarization level of electrons to nuclei by the hyperfine interaction using microwave irradiation with a frequency close to that of the corresponding electron paramagnetic resonance (EPR). Polarization levels can be increased up to 100% for protons and 50% for carbons. The different microwave-based DNP processes can be divided into the Overhauser effect (OE), the solid effect (SE), the cross effect (CE), and thermal mixing (TM), but no quantitative all-embracing description of DNP has been found so far [80,81].

For the hyperpolarized liquid state analysis, it is important to maintain the solid-state polarization of, e.g. a ^{13}C compound when the sample unfreezes and changes phase to the liquid state. *Jan Henrik Ardenkjaer-Larsen et al.* introduced in 2003 the technique of dissolution DNP and opened a whole new field of research in hyperpolarized NMR. The technique of dissolution DNP rapidly dissolves the hyperpolarized frozen sample with a pressurized, superheated liquid, maintaining parts of the solid-state polarization and transfers it to the liquid state. Hyperpolarization decays as soon as it is converted to the liquid phase and part of this work concerns the preservation of the hyperpolarized signal as much as possible. The field of hyperpolarized ^{13}C dissolution DNP includes a wide range of molecules with ^{13}C-labeled carbons in their molecular structure, e.g., [1-^{13}C]pyruvate, [1-^{13}C]alanine, [1-^{13}C]lactate, [1,4-^{13}C]fumarate, and [^{13}C]bicarbonate. A vast diversity of different biochemical processes and biological problems can be investigated with the possibility to label and detect molecules of biomedical importance with NMR and MRI. Multiple disorders and their response to treatment and therapies like cancer, and research on different organs, such as heart, kidneys, and brain, can be monitored non-invasively and in real-time [39,53,55,82-101].

To achieve optimum polarization of the solid-state sample, different conditions must be fulfilled: first, electrons and nuclei must be frozen in an amorphous glass to achieve the best spatial packing and reduce the space between the nuclei and the corresponding electrons. Better glassing properties, including a well-dissolved solid-state sample, result in better hyperpolarization in the solid state. Furthermore, the buildup constant of the solid state is affected by the quality of the formed glass. An added radical, such as OXO63 (OXO) or TEMPOL, provides the required amount of unpaired electrons. Recently, it has been shown that ionizing radiation (UV) can also create non-persistent free radicals that can be used for hyperpolarization [102]. Additionally, a gadolinium-based contrast agent (DOTAREM, ProHance) enhances the polarization level. Dissolution is usually performed with a H_2O- or D_2O-based dissolution agent (DA), like phosphate buffered saline (PBS) or tris(hydroxymethyl)aminomethane (Tris) buffers, to adjust biological parameters, like the pH and the osmolality of the liquid, for subsequent injections. Choosing the right buffer conditions is crucial when the investigated ^{13}C-labeled compound is, for example, pH-sensitive. Optimizing both solid- and liquid-state properties of the dissolution DNP is vital and was investigated intensively in the present work.

2.1.3 Spectral spatial excitation theory

The acquisition of spatially resolved information of a hyperpolarized signal can be performed with many different techniques. Besides the conventional chemical shift imaging (CSI) [83], the signal limitations of hyperpolarized experiments necessitate to employ advanced MR acquisition techniques that preserve the hyperpolarized signal, such as parallel imaging or compressed sensing [103]. Pulses simultaneously selective in space and frequency, developed for conventional fat-water separation MRI [104], were successfully implemented in hyperpolarized ^{13}C experiments [105].

The excitation of k-space can be explained with the small-tip-angle approximation of the Bloch equation (see chapter 2.1.1.4) for transverse magnetization:

$$M_{xy}(r) = i\gamma M_0(r) \int_k W(k)S(k)e^{ir\cdot k}dk \quad (34)$$

So the magnetization excitation is a product of the initial magnetization M_0 and the inverse Fourier transform of

$$W\big(k(t)\big) = \frac{B_1(t)}{\left|\dot{k}(t)\right|} \quad (35)$$

as the weighting function in multidimensional k-space and

$$S(k) = \int_0^T \left\{\delta\left(k(t) - k\left|\dot{k}(t)\right|\right)\right\} dt \quad (36)$$

as the sampling grid in the k-space. By defining the k-space with a spatial axis z

$$k_z(t) = -R \int_t^T G_z(s)ds \ , \quad (37)$$

and a frequency axis ω

$$k_\omega(t) = t - T \quad (38)$$

the k-space can be sampled by an sinusoidal oscillating gradient. R is an arbitrary constant that converts the units of k_z to those of k_ω, which allows calculating the normalizing factor $\left|\dot{k}(t)\right|$ during trajectory design. Using an oscillating gradient trajectory

$$G_z(t) = G\ cos\ \Omega\ (t - T), 0 \le t \le T \quad (39)$$

creates a corresponding k-space trajectory, as shown in Figure 4, with

$$k_z = \frac{RG}{\Omega} \sin \Omega\ (t - T) = \frac{RG}{\Omega} \sin \Omega\ k_\omega\ , -T \le k_\omega \le 0\ . \quad (40)$$

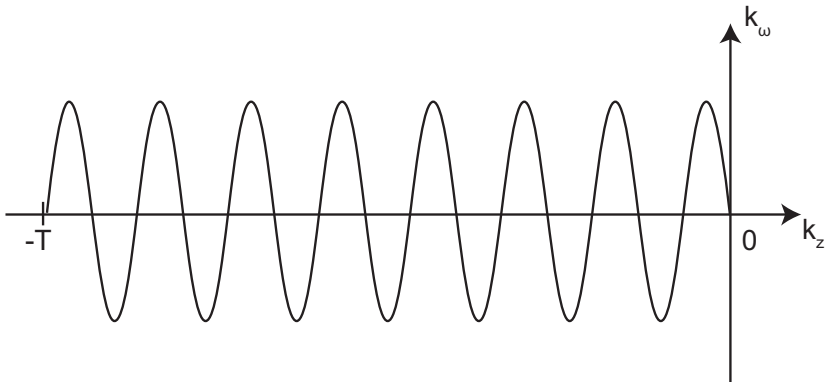

Figure 4: Oscillating gradient k-space trajectory (similar to [104]) extending from –T to 0 while moving through k-space in the z-direction.

The resulting excitation pattern excites a certain frequency at a certain spatial extension. To achieve optimum spectral selectivity, the envelope of the RF pulse should be approximately Gaussian-like (see also chapter 4.2.1.1). Both the spectral and spatial dimensions of the designed pulses are influenced by B_0 and by the strengths and slew rates of the gradients, respectively. By increasing the B_0 resonance frequency, the chemical shift differences (CSDs)

increase, which allows better spectral separation. Additionally, the minimum slice width decreases, assuming that the field strength increases with a constant gradient power.
Usually, the RF field is applied at positive and negative plateaus of the trapezoidal G_z trajectory. This half-shifted pulse design allows fast acquisition, owing to the use of positive and negative plateaus for the acquisition, both at maximum gradient strength: $G_{z_{max}} = G_{z_{pos}} = G_{z_{min}}$. A weakness of this design is the vulnerability against phase errors of the gradients, which will sum up during acquisition. A more robust alternative is the so-called fly-back design, where the RF field is only applied on the positive gradient plateaus, followed by a rewinding gradient. The integral values of the positive and negative direction of the gradient must be equal for full k-space coverage. This can be achieved by limiting the positive plateaus to half of the maximum gradient strength: $G_{z_{max}} = 2\, G_{z_{pos}} = G_{z_{min}}$. Possible phase errors cancel out during the rewinding gradient, increasing the design's robustness against this type of errors. The imaging experiments in this work were performed mostly in a fly-back design with subsequent single-shot spiral readout for signal acquisition (see Figure 5).

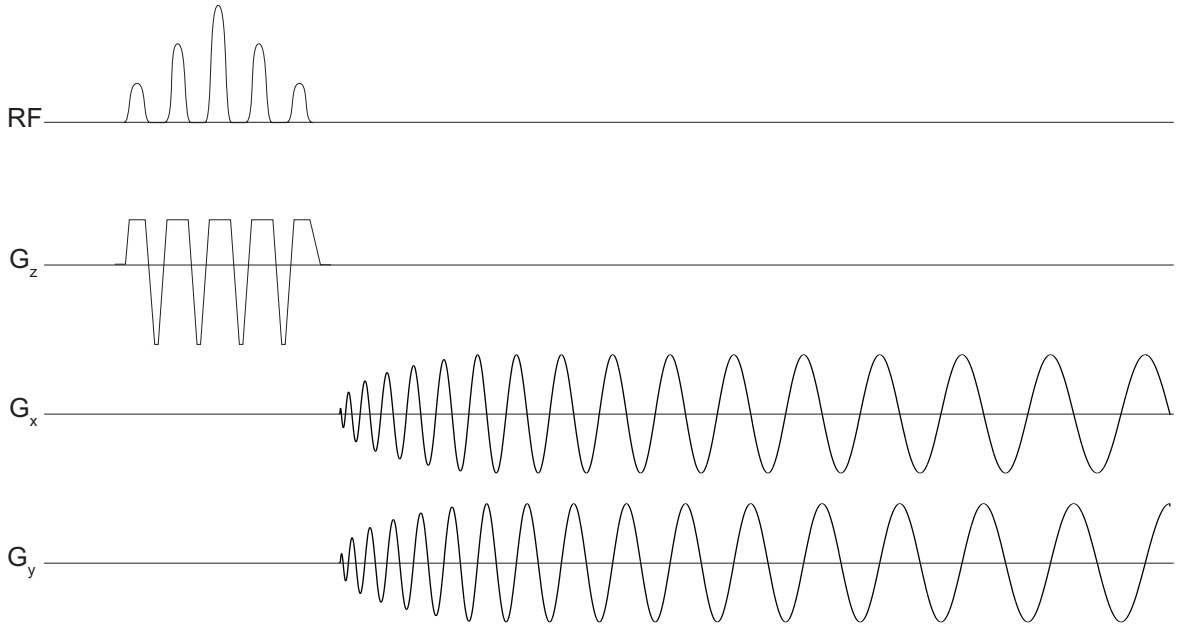

Figure 5: Typical acquisition scheme of a hyperpolarized experiment with SPSP excitation and single-shot spiral readout. The RF scheme shows the applied radio frequency, ideally having a Gaussian envelope shape and being applied on the positive plateaus of the G_z gradient, designed in fly-back mode. The excitation is followed by single-shot spiral readout, performed by interleaved G_x and G_y gradients.

2.1.4 IDEAL theory

The separation and spectral encoding of off-resonant frequencies is important for proton (fat, water) as well as for hyperpolarized ^{13}C MR. Different metabolites (e.g., pyruvate, lactate, alanine, bicarbonate) show different resonance frequencies, which can be separated and quantified. One method involves the encode of information via IDEAL separation [106]. The technique is already widely applied in clinical proton MRI [107]. Here, echoes with a certain echo time ΔTE are acquired. Figure 6 depicts the phase acquisition of signals ($S_{1,2}$) at $t_0 = 0$

and after echo time $t_2 = \Delta t$. The phase contributions of two metabolites *A* and *B* to the signal change with time.

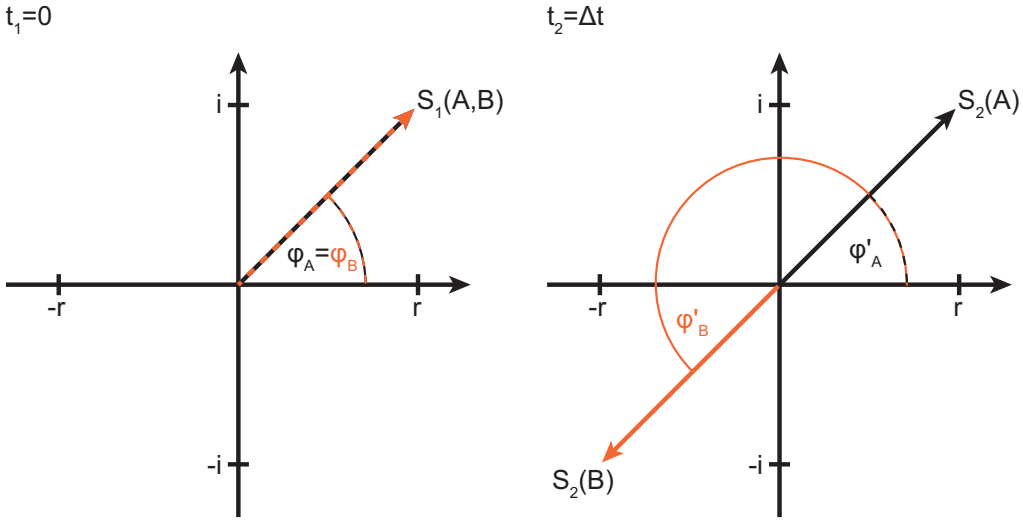

Figure 6: Scheme of signal acquisitions with different metabolite contributions. At $t = 0$ (left figure), the signal contributions are defined by the same angle $\varphi_A = \varphi_B$. At $t = \Delta t$, the signal contribution from metabolite *B* has experienced a phase shift of π.

Here, the two metabolites *A* and *B* are measured at different time points and show the signals:

$$A = a_r + ia_i = A_0(cos\varphi_a + isin\varphi_a) = A_0(cos\omega t_1 + isin\omega t_1) \quad (41)$$

$$B = b_r + ib_i = B_0(cos\varphi_b + isin\varphi_b) = A_0(cos\omega t_2 + isin\omega t_2)\,. \quad (42)$$

with respect to the real parts (a_r, b_r) and the imaginary parts (ia_i, ib_i) of A and B and the corresponding trigonometric functions at t_1 and $t_2 = t_1 + \Delta t$. Assuming a phase shift of B with $\Delta\omega\Delta t = \pi$, B becomes:

$$B = B_0(cos(\varphi_a + \pi) + isin(\varphi_a + \pi))\,. \quad (43)$$

Measuring at $t_1 = 0$ and using an echo with

$$\Delta TE = \Delta t = \frac{\pi}{\Delta\omega} = \frac{\pi}{2\pi\Delta f} = \frac{1}{2\Delta f} \quad (44)$$

leads to the following signals, to which both metabolites contribute

$$S_1(0) = a_r + ia_i + b_r + ib_i \quad (45)$$

and

$$S_2(\Delta t) = a_r + ia_i - b_r - ib_i \quad (46)$$

Subsequent addition and subtraction of the signals lead to:

$$S_1 + S_2 = 2a_r + 2ia_i \quad (47)$$

$$S_1 - S_2 = 2b_r + 2ib_i\,. \quad (48)$$

As can be seen from equations (47) and (48), the signal contributions of metabolites *A* and *B* are now separated and can be determined for the measurements.

2.2. Biochemistry

The biochemical background section starts with a determination of the pH value, which is the core parameter investigated in this work (chapter 2.2.1). Extensive work has been conducted on concentration improvements and solubility theory will explain the background behind it (chapter 2.2.2). To understand the *in vivo* behavior of bicarbonate, the background of enzyme kinetics (chapter 2.2.3) and, more specifically, reactions with and without carbonic anhydrase (chapter 2.2.4) are described.

2.2.1 pH value

In 1884, the Swedish chemist and physicist *Svante Arrhenius* developed the theory of electrolytic dissociation. When dissolved, compounds reversibly dissociate in anionic and cationic compartments. In 1909, *Søren Sørensen* introduced the notation $c_p=10^{-pH+}$ for the concentration of protons in a certain solution, where p was used as a random parameter for defining the examined solution. Later, the term *pH* was used, derived from the Latin *potentia Hydrogenii* (force of hydrogen) or *pondus Hydrogenii* (weight of Hydrogen), and connected to the hydrogen *activity*. In 1923, *Brønsted* and *Lowry* developed independently from each other an acid-base theory, which was based on the concept of proton donation by acids (deprotonation) and proton acceptance by bases (protonation).

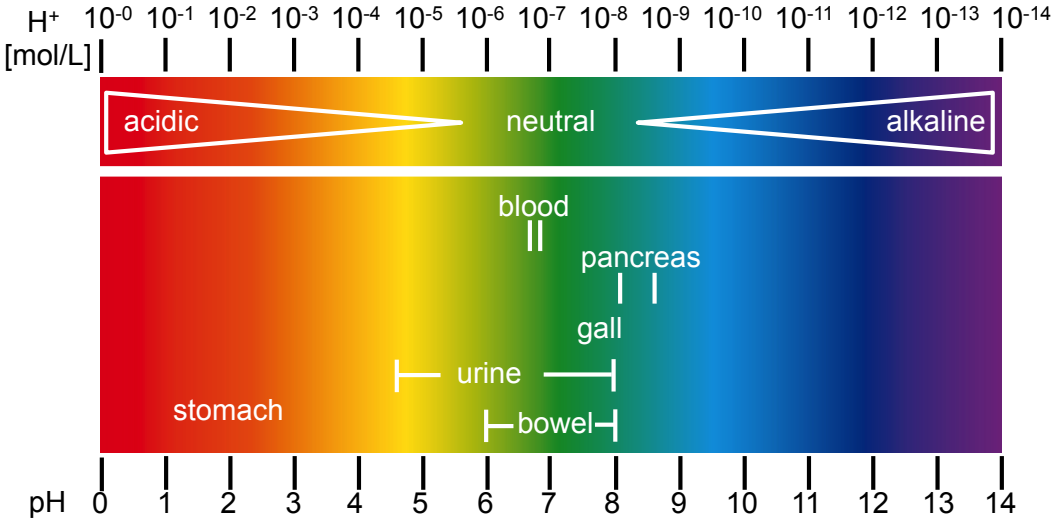

Figure 7: Schematic view of pH values (bottom) with their corresponding proton concentrations (top) and pH values of different organs are depicted.

Today, pH is defined as the negative decimal logarithm of hydrogen activity

$$pH = -log_{10}(a_H) \quad (49)$$

where $a_H = d_H \cdot [H^+]$ with d_H is the activity coefficient in diluted solutions and $[H^+]$ is the concentration of hydrogen.

In aqueous solutions, pH equals the concentrations of oxonium ions (H_3O^+) generated by autoprotolysis:

$$pH = -log_{10}\left(c_{H_3O^+}\frac{L}{mol}\right). \quad (50)$$

Conduction measurements of distilled water show a small electric current that could only exist if ions were produced by the water itself. H_2O is amphoteric and can be both proton acceptor: $H_2O + H^+ \rightarrow H_3O^+$, forming an oxonium ion, or proton donor: $H_2O \rightarrow OH^- + H^+$, forming a hydroxide ion, leading to a proteolysis equilibrium of

$$H_2O + H_2O \rightleftharpoons H_3O^+ + OH^-. \quad (51)$$

According to the law of mass action, introduced by *Guldberg* and *Waage* in 1867, this is a reversible reaction following

$$aA + bB \rightleftharpoons cC + dD, \quad (52)$$

which attains equilibrium at a certain temperature and hence the reaction quotient K remains constant:

$$K = \frac{[\mathrm{C}]^c \cdot [\mathrm{D}]^d}{[\mathrm{A}]^a \cdot [\mathrm{B}]^b} \quad (53)$$

where a, b, c, and d are stoichiometric constants and [A], [B], [C], and [D] are molar equilibrium concentrations. For water, equation (53) becomes

$$K = \frac{[H_3O^+] \cdot [OH^-]}{[H_2O]^2} \quad (54)$$

which can be rewritten as

$$K \cdot [H_2O]^2 = [H_3O^+] \cdot [OH^-]. \quad (55)$$

Shifting the equilibrium to one side of the reaction negligibly changes the water concentration of 55.5 mol/L, hence the water dissociation constant is:

$$K_W = [H_3O^+] \cdot [OH^-], \quad (56)$$

and with $[H_3O^+] = [OH^-] = 10^{-7}\frac{mol}{L}$, K_W becomes

$$K_W = 10^{-14}\frac{mol^2}{L^2}. \quad (57)$$

Regarding logarithmic notation, with the activity of water in diluted aqueous solutions equal to 1, equation (56) can be rewritten as

$$-log_{10}K_W = -log_{10}[H_3O^+] - log_{10}[OH^-] = pK_W. \quad (58)$$

Introducing pOH as the negative decimal logarithm of $[OH^-]$, it can be solved as

$$14 = pH + pOH. \quad (59)$$

Hence, pH is neutral (= 7) when the concentrations of H_3O^+ and OH^- are the same, and changes in the H_3O^+ concentration lead to changes in pH:

$$pH \begin{cases} > 7 & [H_3O^+] < [OH^-] \quad basic \\ = 7 & [H_3O^+] = [OH^-] \quad neutral \\ < 7 & [H_3O^+] > [OH^-] \quad acidic \end{cases} \quad (60)$$

K_W is dependent on temperature and pressure and the value of 14 only holds true for standard conditions of T=25°C and 0.1 MPa [108].

All above calculations can also be regarded in terms of pOH since it is directly connected with pH (see equation (59)). With this, the proton donating or accepting ability of bases can be described. This is of use for calculating, for example, alkaline compounds.

2.2.1.1 *Acidic dissociation constant K_s*

Whereas K_w is a special case for water, a general acidic constant K_S can be defined for every reaction in a protonated solvent. To define the strength of an acid or base, one can calculate the dissociation constant for each reaction:

$$HA + B \rightleftharpoons HB^+ + A^- , \quad (61)$$

where HA is an acid and B is the reaction partner. HB^+ is the protonated form of B and A^- the corresponding deprotonated base of HA. The stronger K_S is, the more the reaction shifts to the right side and HA likely to donate the proton. This can also be seen by equation (53), where a higher equilibrium constant is connected to higher values of reaction products $[\mathrm{C}]^c \cdot [\mathrm{D}]^d$. For multiple purposes, it is often useful to transform K_S into: $pK_S = -\log K_S$. For bases, the corresponding $pK_B = -\log K_B$ can be calculated and the constants are connected by:

$$pK_W = pK_S + pK_B \quad (62)$$

2.2.1.2 *pH value calculations*

For most pH value calculations, the chemical properties allow the application of different approximations for the ionic water product from models, the law of mass action, and the conservation of mass and charge [109,110]. Defining the properties of the investigated compound leads to classifying the chemical compound into one of the categories of very weak acids ($pKs > 9.5$), weak acids ($4.5 < pKs < 9.5$), strong acids ($1 < pKs < 4.5$), and very strong acids ($pKs < 1$). However, this work mostly examines the special cases of acids with multiple protonating steps and of salts of weak acids/bases.

Some compounds show the capability to dissociate more than one proton. Each proton dissociation step has a different dissociation constant at 25°C. The dissociation steps always follow a typical scheme:

$$pK_{S1} < pK_{Si-1} < pK_{Si}, \quad (63)$$

with i steps of dissociation. For H_3PO_4, three dissociation steps are possible:

$$\begin{aligned} H_3PO_4 &\rightleftharpoons H^+ + H_2PO_4^- ; \quad pK_{S1} = 2.12 \\ H_2PO_4^- &\rightleftharpoons H^+ + HPO_4^{2-} ; \quad pK_{S2} = 7.21 \\ HPO_4^{2-} &\rightleftharpoons H^+ + PO_4^{3-} ; \quad pK_{S3} = 12 \end{aligned} \quad (64)$$

The lower the pK_S values are, the higher is the capability of the molecule to donate protons. Furthermore, carbonic acid (H_2CO_3) is a special case concerning its different pK_S values:

$$\begin{aligned} H_2CO_3 &\leftrightharpoons HCO_3^- + H^+ ; \quad pK_{S1} = 3.6 \\ HCO_3^- &\leftrightharpoons CO_3^{2-} + H^+ ; \quad pK_{S2} = 10.33 \end{aligned} \quad (65)$$

However, one must be careful when quoting pK_{S1}, because carbonic acid can also dissociate directly:

$$H_2CO_3 \leftrightharpoons H_2O + CO_2(aq). \quad (66)$$

This is an equilibrium state for carbonic acid and dissolved carbon dioxide and the concentration of carbonic acid is much lower than that of carbon dioxide. Hence, the dissolved CO_2 directly influences the equilibrium of bicarbonate and carbonic acid in aqueous solutions, leading to an apparent dissociation constant pK_{S3}:

$$H_2CO_3 \leftrightharpoons HCO_3^- + H^+ ; \quad pK_{S3} = 6.3. \tag{67}$$

Aqueous solutions of strong salts and bases show in general neutral pH, e.g., NaCl. When dissociated, H_2O is a stronger base than Cl^- and hence, the pH stays unaffected. However, salts of weak acids and bases can behave differently and change pH, depending on the strength of the cations and anions of the corresponding conjugated bases and acids, which define their capability to further react with H_2O.

The properties of the different groups of compounds are mostly defined by their state of protonation in equilibrium and the complexity of the occurring reactions. The given examples concerned acid calculations, but using K_B instead of K_S will allow the application to base calculations. A schematic overview of pH in biology is given in Figure 7.

2.2.1.3 *Henderson-Hasselbalch equation*

In this work pH mapping is performed by measuring the ratio of bicarbonate and CO_2 signals and hence their ratio of concentrations as shown in equation (1). This is a derivation from the Henderson-Hasselbalch equation as explained in the following:

Neglecting the proton acceptor from equation (61), the equilibrium of ionization for weak acids can be simplified to:

$$HA \rightleftharpoons H^+ + A^- , \tag{68}$$

According to equation (53) dissociation constant K_s for this ionization is:

$$K_s = \frac{[H^+][A^-]}{[HA]} \tag{69}$$

Which can be transformed to

$$\frac{1}{[H^+]} = \frac{1}{K_s}\frac{[A^-]}{[HA]} \tag{70}$$

and logarithmized to

$$pH = pK_s + \log\left(\frac{[A^-]}{[HA]}\right) . \tag{71}$$

For the case of the carbonic acid dissociation (see equations (66) and (67)), equation (69) can be written as

$$K_s = \frac{[H^+][HCO_3^-]}{[H_2CO_3]} = \frac{[H^+][HCO_3^-]}{[H_2O][CO_2]} \tag{72}$$

which subsequently can be translated and simplified to equation (1).

2.2.2 Solubility

The solubility of bicarbonate constitutes a major bottleneck for the bicarbonate-related work. The usability of ^{13}C-sodium bicarbonate was primarily tested; however, owing to the small counter ion, it has very limited solubility. Therefore, it is not the best solution for quantification and method analysis and subsequent *in vivo* works, where a good SNR is needed. The preparation work with bicarbonate mainly involves highly concentrated ionic solutions ($c_{max}(Na_{BiC}) \approx 1.2\frac{mol}{L}; c_{max}(Cs_{BiC}) \approx 6\frac{mol}{L}$), which is why ionic influences cannot be neglected when describing solution theory.

The following calculations determine the theoretical maximum solubility s of the bicarbonate ion (HCO_3^-) with different counter ions ($Li^+, Na^+, Rb^+, Cs^+, K^+, NH_3^+, Ca^{2+}$). For understanding the dissolving process, the dissolution of a nearly insoluble salt ($CatAn$) consisting of an anion (An^-) and a corresponding cation (Cat^+), is described [111].
The maximum solubility of an ionic compound is defined as the molality of the saturated solution in which a dynamic equilibrium exists between the compound in the undissolved and the dissolved state. The equilibrium of the solution is:

$$CatAn(s) \rightleftharpoons Cat^+(aq) + An^-(aq). \quad (73)$$

In a saturated solution, the equilibrium constant K is related with the activity constants a for each ion as

$$K = a(Cat^+) + a(An^-). \quad (74)$$

Due to the very low solubility, the activities can be replaced with the molalities $m(Ion)$:

$$K = \frac{m(Cat^+)}{m^\ominus}\frac{m(An^-)}{m^\ominus}, \quad (75)$$

where $m^\ominus = 1\,\frac{mol}{kg}$ is used to give a dimensionless result. Since one anion and one cation are produced, during the dissolution process, it is $m(Cat^+) = m(An^-)$. With the solubility s as a constant value, equation (75) can be rewritten as

$$s = \sqrt{K}m^\ominus. \quad (76)$$

The equilibrium constant K can be derived from:

$$R\,T \ln K = -\Delta_R G^\ominus, \quad (77)$$

with relation to the free standard reaction enthalpy (a.k.a. Gibbs energy), $\Delta_R G^\ominus$, the temperature $T = 298.5K$, and the gas constant R. $\Delta_R G^\ominus$ can be calculated by:

$$\Delta_R G^\ominus = \Delta_B G^\ominus(Cat^+, aq) + \Delta_B G^\ominus(An^-, aq) - \Delta_B G^\ominus(CatAn, s) \quad (78)$$

where $\Delta_B G^\ominus$ is the energy required for the formation of the dissolved ions, and the solubility s can be written as:

$$s = \sqrt{e^{-\frac{\Delta_R G^\ominus}{R\,T}}}\,m^\ominus \left[\frac{mol}{kg}\right]. \quad (79)$$

Calculating the maximum solubility values for bicarbonate and the corresponding counter ions results in:

counter ion	compound	$\Delta_R G^\ominus$	s
Na^+	$NaHCO_3$	1.319	0.766
NH_4^+	NH_4HCO_3	0.179	1.036
K^+	$KHCO_3$	-6.539	3.739

Table 1: Examples of free Gibbs energy (values from [112]) and calculated maximum solubility.

As can be seen from equation (79) the maximum solubility is directly connected to $\Delta_R G^\ominus$. Coherence between $\Delta_R G^\ominus$ and maximum solubility is shown in Table 1. Increasing the temperature also leads to an increase of the solubility. Cesium bicarbonate exhibited much better solubility properties owing to the bigger size of the counter ion and the lower grid enthalpy required to dissolve the salt in a liquid.

Defining the properties of proton enthalpies $(\Delta_B G^{\ominus}(H^+, aq), \Delta_B H^{\ominus}(H^+, aq)) = 0$ for any temperature allows calculating the enthalpies for any cations and anions of the corresponding salt. The solvation of a given salt can be described by the following scheme (like [111]):

0. General reaction $$\frac{1}{2}\mathrm{Cat_2(g)} + \frac{1}{2}\mathrm{An_2(g)} \rightarrow \mathrm{Cat^+(aq)} + \mathrm{An^-(aq)} \quad (80)$$

1. Formation of the ion $$\frac{1}{2}\mathrm{X_2(g)} \rightarrow \mathrm{X(g)} \quad (81)$$

2. Electron attachment $$\mathrm{X(g)} + \mathrm{e^-(g)} \rightarrow \mathrm{X^-(g)} \quad (82)$$

3. Hydratation $$\mathrm{X^-(g)} \rightarrow \mathrm{X^-(aq)} \quad (83)$$

Hydratation can be described by the free solvation energy $\Delta_{Solv}G^{\ominus}$, which equals the free hydration enthalpy $\Delta_{Hyd}G^{\ominus}$ when water is used as a dissolution agent. Transferring an ion from vacuum to dissolution can be described by the Born equation:

$$\Delta_{Solv}G^{\ominus} = -\frac{z^2 e^2 N_A}{8\pi\epsilon_0 r}\left(1 - \frac{1}{\varepsilon_{rel}}\right), \quad (84)$$

where ε_{rel} is the relative dielectric constant of the solution, r is the radius, and z is the charge of the ion. Looking at the ionic radii of the counter ion candidates for bicarbonate (see Table 5) one can state that the solubility increases with increasing ionic radius as $\Delta_{Solv}G^{\ominus}$ decreases from Li^+ to Cs^+. Expanding these ideas to ionic lattices, the Born-Landé equation allows calculating the lattice energies that are needed to break the lattice and separate its compounds in vacuum:

$$\Delta_{lat}U = -\frac{M\, z^+ z^- e^2\, N_A}{4\,\pi\,\varepsilon_0\, r_0}\left(1 - \frac{1}{n}\right), \quad (85)$$

where M is the Madlung constant, dependent on the geometry of the crystal, z^+ and z^- the charges of the cation and anion, respectively, r_0 is the distance of the shortest cation-anion pair, and n is the Born exponent for different ion types. Lattice energies of selected bicarbonate compounds are listed in Table 2.

Ion	Hydration enthalpy of Ion $\left[\frac{kJ}{mol}\right]$	Bicarbonates	Lattice energy $\left[\frac{kJ}{mol}\right]$
Na	-503	$NaHCO_3$	818
K	-314	$KHCO_3$	736
Rb	-289	$RbHCO_3$	714
Cs	-256	$CsHCO_3$	709
NH_4	-293	NH_4HCO_3	741
Ca^{2+}	-1577	$Ca(HCO_3)_2$	2403

Table 2: Values of hydration enthalpy for selected ions and lattice energies for the corresponding bicarbonates. Values from [112].

Depending on the values of lattice energy and hydration enthalpy, exo- or endothermic reactions can be predicted. The lattice enthalpy $\Delta_{lat}H$ and the entropy are connected as:

$$\Delta_{lat}U = \Delta_{lat}H - p\Delta V_m \quad (86)$$

with an outer pressure p and change of volume per mol ΔV_m. The entropy an ion in a solution $S^{\ominus}(ion, aq)$ is always given relatively to the entropy of hydrogen ions in water:

$S^{\ominus}(H^+, aq) = 0$. Its value is defined by the order of the formed hydrate shells around the ion: smaller ions with a higher charge lead to a higher order of hydrate shells compared to larger ions with single charge.

2.2.3 Enzyme kinetics

The principle of hyperpolarized ^{13}C bicarbonate pH imaging is fundamentally based on the fact that equilibrium between bicarbonate and CO_2 is enzymatically enhanced. A catalytically active enzyme is called holoenzyme and consists of an inactive apoenzype and a co-factor. If the factor is strictly bound to the apoenzyme, it is called prosthetic group. Like substrates, some co-factors can be released, but they differ in the fact that they originate from vitamins and many enzymes can use the same co-factors. It is important that enzymes do not shift the thermodynamic equilibrium to one side. They can only decrease the time, which is required for the establishment of equilibrium.

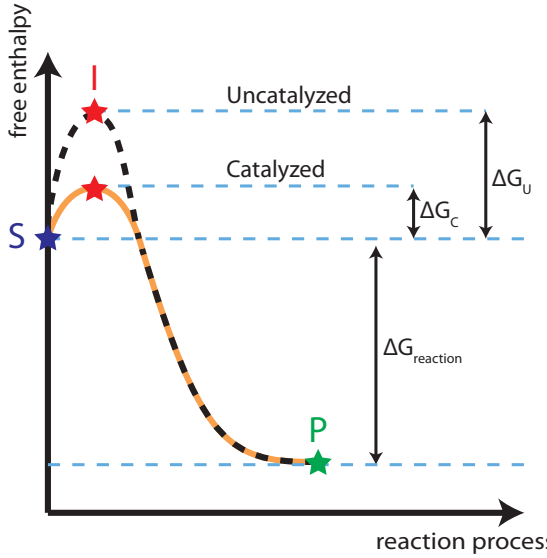

Figure 8: Schematic overview of the conversion of a substrate (S) to a product (P). The uncatalyzed reaction shows a higher requirement of free reaction enthalpy to form the intermediate (I): $\Delta G_U > \Delta G_C$. The overall reaction enthalpy $\Delta G_{reaction}$ remains unaffected by the catalysis. Figure similar to that presented in [113].

From equation (77) it can be seen that the equilibrium of a reaction can be described by the free standard reaction enthalpy $\Delta_R G^{\ominus}$. In Figure 8, one can see that a certain energy enthalpy level of an intermediate step (I) must be reached before a reaction happens. The enthalpy difference between the substrate (S) and the product (P), which is called activation energy, is lower for a catalyzed reaction (ΔG_C) compared with that in an uncatalyzed one (ΔG_U). The influence of this energy lowering has direct influence on the reaction speed. Assuming a reaction from a substrate S to a product P with the intermediate state I, where the substrate and the intermediate state are in equilibrium:

$$S \overset{K}{\leftrightarrow} I \overset{v}{\rightarrow} P\,, \tag{87}$$

where K is the equilibrium constant, the reaction velocity v is directly proportional to the concentration of the intermediate state due to the fact that P can only be produced by I:

$$v_{product} \propto [I] \quad (88)$$

Since $[I]$ is again dependent on the activation energy difference $(= \Delta G_{U,C})$, the overall reaction velocity can be described as:

$$v_{reaction} = v_{product}[I] = \frac{kT}{h}[S]e^{-\frac{\Delta G_{U,C}}{RT}} \quad (89)$$

Reducing the activation energy directly leads to an increase in reaction speed.

2.2.3.1 *Reactions orders*

Enzyme kinetics is classified according to the participating reactants. Most *in vivo* reactions are described by reactions from 0th to 2nd order.

Reactions of 0th order are independent from the concentrations of the substrate and the product:

$$S \rightarrow P \quad (90)$$

The reaction velocity v is constant and described by k:

$$v = k, \left[\frac{M}{s}\right] \quad (91)$$

Reactions of the 1st order are dependent on the change of substrate concentration $[S]$:

$$S \rightarrow P \quad (92)$$

$$v = k \cdot [S], \left[\frac{1}{s}\right] \quad (93)$$

Reactions of the 2nd order are described by the change of the concentrations of two substrates (S_1, S_2) with the reaction scheme of equation (90):

$$v = k \cdot [S_1] \cdot [S_2], \left[\frac{1}{Ms}\right] \quad (94)$$

If one of the substrates are concentration-independent ($[S_{1,2}] = const.$), the reaction follows the 1st order description.

Enzymatic reactions are described by the model introduced in 1913 by *Michaelis and Menten,* where an enzyme (E) and substrate (S) form an intermediate complex (ES) before releasing a product (P):

$$E + S \underset{k_{-1}}{\overset{k_1}{\rightleftarrows}} ES \underset{k_{-2}}{\overset{k_2}{\rightleftarrows}} E + P. \quad (95)$$

For simplification, this reaction can be described for an early time point with a low concentration of the product $[P]$, leading to:

$$k_{-2} \cdot [E] \cdot [P] \approx 0 \quad (96)$$

With a second assumption of a steady state, postulated by *Briggs and Haldane* in 1923, where the concentration of the intermediate state $[ES]$ stays constant for the case that the buildup and decay of the complex is constant, one can define the catalysis velocity of the reaction by:

$$V_0 = V_{max}\frac{[S]}{[S] + K_M}, \quad (97)$$

where V_{max} is the maximum catalyse velocity, calculated when all binding sites of the enzyme are occupied, and K_M is the Michaelis constant:

$$K_M = \frac{k_{-1} + k_2}{k_1} . \quad (98)$$

2.2.4 Reactions with and without carbonic anhydrases

The transformation between HCO_3^- and CO_2 is important for pH buffering reactions but also for other important biochemical reactions, like the exhalation of CO_2. Without the help of the enzymatic carbonic anhydrase system, the reaction would be too slow. The forward and reverse reactions of hydration of CO_2 are depicted in Figure 9.

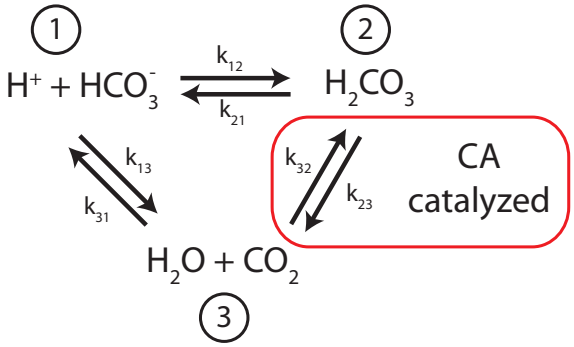

Figure 9: Bicarbonate reactions with corresponding reaction constants k. The reactions with constants k_{32} and k_{23} are catalyzed by the carbonic anhydrases (CA).

At normal *in vivo* conditions (T = 37° C, physiological pH), the velocity constants of the reaction from CO_2 and carbonic acid can be calculated by the ratio of the concentrations of CO_2 and H_2CO_3, which is 340: 1, and the equilibrium constant $K_{32} = 5.4 \cdot 10^5$. The second order reaction from CO_2 to carbonic acid has a reaction constant $k_{32} = 0.0027 \frac{1}{M\,s}$ [114]. In water ($c_{H_2O} = 55.5\,M$), this corresponds to an effective reaction constant $k_{32_{eff}} = 0.15 \frac{1}{s}$, which is quite fast. The reverse reaction shows an even faster value of $k_{23_{eff}} = 50 \frac{1}{s}$. However, these reactions are catalyzed due to their importance in many biological and biochemical processes, examples include the bicarbonate pH buffering system, urea synthesis and synthesis of liquids (e.g. eye liquid) in the body. Furthermore, bicarbonate and CO_2 often act as co-factors for transporting processes and enzymatic activities. These reactions are catalyzed up to $k_{cat} = 10^6 \frac{1}{s}$, which makes the carbonic anhydrases one of the fastest enzymes known. Similar to most enzymes, the catalytic activity of carbonic anhydrases is pH-dependent [115]. Carbonic anhydrases show an increase of catalytic activity $k_{cat}(pH = 6) \leq 1 \cdot 10^5$ to $k_{cat}(pH = 8) \geq 9 \cdot 10^5$. One should keep this in mind while regarding possible influences on signal parameters (see chapter 5.2). The ionization reactions between the carbonic acid and the bicarbonate (k_{12}, k_{21}) are known to be very fast [116] and a permanent equilibrium can be assumed between the two species. For the direct reaction, values [117] of $k_{13} = 5.5 \cdot 10^4 \frac{1}{M\,s}$ and $k_{31} = 0.043 \frac{1}{M\,s}$ have been reported. These values show that the dissociation of bicarbonate into water and carbon dioxide is relatively fast. In contrast, the

low-rate constant of the direct reaction (k_{31}) to bicarbonate is not the main reaction pathway. Hence, the catalyzed reaction works via the catalyzed formation of carbonic acid.

The group of carbonic anhydrases is per definition divided into five families ($\alpha, \beta, \gamma, \delta, \varepsilon$), of which only the α-carbonic anhydrases are found in mammals. This group is again divided into subgroups ranging from CA-I to CA-XV [118], which differ in the occurrence (e.g., cytosol-, mitochondria-, and cell-membrane-associated) and catalytic activity properties (see Table 3). They are not only involved in pH regulation but also play a role in tumorigenic processes, cell adhesion, and cell proliferation [119].

Isoenzyme	Appearance	k_{cat} [s^{-1}]	K_m [mM]	k_{cat}/K_m [$M^{-1}\ s^{-1}$]
CA I	Cytosol	$2.0 \cdot 10^5$	4.0	$5.0 \cdot 10^7$
CA II	Cytosol	$1.4 \cdot 10^6$	9.3	$1.5 \cdot 10^8$
CA III	Cytosol	$1.3 \cdot 10^4$	52.0	$2.5 \cdot 10^5$
CA IV	GPI-anchored	$1.1 \cdot 10^6$	21.5	$5.1 \cdot 10^7$
CA VA	Mitochondria	$2.9 \cdot 10^5$	10.0	$2.9 \cdot 10^7$
CA VB	Mitochondria	$9.5 \cdot 10^5$	9.7	$9.8 \cdot 10^7$
CA VI	Secreted	$3.4 \cdot 10^5$	6.9	$4.9 \cdot 10^7$
CA VII	Cytosol	$9.5 \cdot 10^5$	11.4	$8.3 \cdot 10^7$
CA IX	Transmembrane	$1.1 \cdot 10^6$	7.5	$1.5 \cdot 10^8$
CA XII	Transmembrane	$4.2 \cdot 10^5$	12.0	$3.5 \cdot 10^7$
CA XIII	Cytosol	$1.5 \cdot 10^5$	13.8	$1.1 \cdot 10^7$
CA XIV	Transmembrane	$3.1 \cdot 10^5$	7.9	$3.9 \cdot 10^7$
CA XV	GPI-anchored	$4.7 \cdot 10^5$	14.2	$3.3 \cdot 10^7$

Table 3: Carbonic anhydrase isoforms with their corresponding k_{cat} and K_m values and the calculated molar rate constant k_{cat}/K_m. The appearance of the isoforms is also listed.

The catalysis of carbonic anhydrases is a four-step mechanism (see Figure 10). The main factor affecting catalyzation is a pK_S value decrease to $pK_S = 7$ of the Zn^{2+} bound water compared to bulk water, which has $pK_S = 15.9$. This allows a release of a proton from the water and the subsequent reactions. Interestingly, the catalysis itself is inherently limited by the proton diffusion of water: water has a very high diffusion coefficient of $10^{11}\,\frac{1}{M\,s}$, which is reflected by k_{-1} in Figure 10. When $pK_S = 7$, the equilibrium constant is given by: $K = \frac{k_1}{k_{-1}} = 10^{-7}$. Thus, k_1 is limited to values $\leq 10^4\,\frac{1}{s}$. However, as mentioned above, the catalysis activity of carbonic anhydrases shows values of up to $10^6\,\frac{1}{s} = k_1$. This problem can be solved by using a buffer agent with a higher concentration than that of proton and hydroxide ions in water at $pH = 7$ with $c_{max} = 10^{-7}M$. The onward reaction in the buffer environment is then $k_1 = k_1^* \cdot c_b$, which is now limited by the buffer diffusion constant ($k_1^* \leq 10^9\,\frac{1}{M\,s}$) and the concentration of the buffer c_b. This leads to a minimum buffer concentration:

$$c_b(min) = \frac{k_1}{k_1^*} = \frac{10^6 \frac{1}{s}}{10^9 \frac{1}{M\,s}} = 10^{-3} M\,. \qquad (99)$$

To sum up, the catalytic activity of carbonic anhydrases is only possible for buffer solutions with concentrations $\geq 10\ mM$.

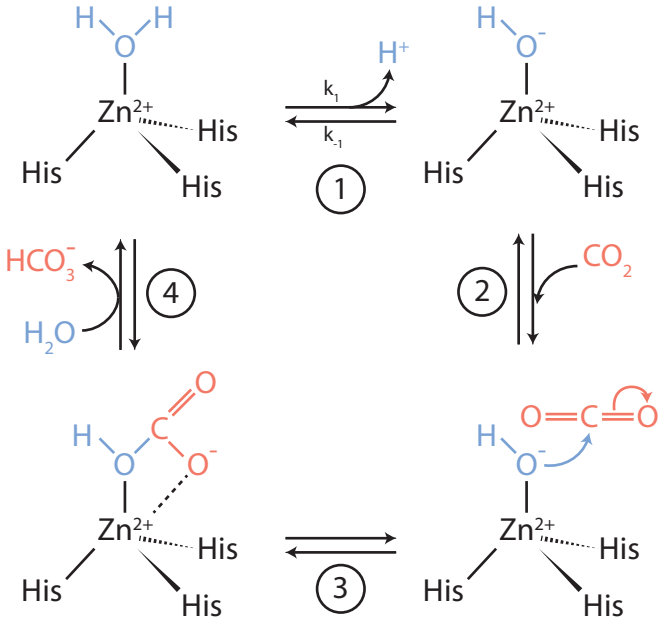

Figure 10: Four-step catalysis of carbonic anhydrase with a zinc ion acting as the active center of the enzyme and three histidin residues and a bound water molecule as the initial conditions. Step 1: The bound zinc ion decreases the water's pK_S, thus allowing a release of a proton. The reaction constants of the forward reaction (k_1) and the backward reaction (k_{-1}) are shown. Step 2: Carbon dioxide binds to the active center of the enzyme and is positioned so that it can react with the hydroxide ion. Step 3: The hydroxide ion attacks the carbon dioxide and forms bicarbonate. Step 4: The bicarbonate is released and replaced by water to achieve the initial conditions. Figure similar to that presented in [114].

3. Methods

For successful pH mapping, standardized methods were optimized and adjusted to achieve maximum SNR for subsequent application and analysis. First, the bicarbonate synthesis was established and optimizations of the bicarbonate sample preparation were performed (chapter 3.1). Subsequently, modifications to the dissolution procedure (chapter 3.2) led to an overall optimized experimental protocol for subsequent *in vitro* and *in vivo* application. The data analysis procedures were custom-tailored for the desired purpose (chapter 3.3).

3.1. Optimizing sample

3.1.1 Na vs. Cs

To find an optimum counter ion for the bicarbonate synthesis, different parameters must be taken into account, such as toxicity, solubility, availability/cost, and handling. To achieve an electrically neutral compound, it is necessary to neutralize the singly negatively charged bicarbonate (HCO_3^-) with an equally positively charged counter ion. Group 1 of the periodic system excluding hydrogen, namely, the group of Alkali metals, exhibit this property. These have their outermost electron in the s-orbital, which they easily donate to form singly positively charged cations. The group consists of lithium, sodium, potassium, rubidium, cesium and francium. Francium shows a fast natural radioactive decay and can therefore be excluded from further investigation. Other positively charged ions that could be used for the synthesis are nitrogen and calcium. Calcium is a special case, as its ion is doubly positively charged and two bicarbonates are needed to achieve electric neutrality. Another method of electrical neutralization could be the use of singly positively charged complex molecules. Owing to the higher complexity in the synthesis and the unknown stability at a certain pH and temperature, this approach was not further followed.

3.1.1.1 *Solubilities and toxicities*

The toxicities of the corresponding carbonates and bicarbonates are listed in the following table (numbers in brackets are the temperatures where dissolution takes place):

name	formula	solubility in g per 100 g H_2O	toxicity - LD50
Lithium-Carb.	Li_2CO_3	1.54 (0°C) - 0.72 (100°C)	525 mg/kg (oral - rat)
Lithium-Bicarb.	$LiHCO_3$	5.74 (20°C)	NA
Sodium-Carb.	Na_2CO_3	7 (0°C) - 49 (40°C)	4090 mg/kg (oral - rat)
Sodium-Bicarb.	$NaHCO_3$	7 (0°C) - 16 (60°C)	4220 mg/kg (oral- rat)
Potassium-Carb.	K_2CO_3	105 (0°C) - 156 (100°C)	1870 mg/kg (oral - rat)
Potassium-Bicarb.	$KHCO_3$	22.5 (0°C) - 65.6 (60°C)	2064 mg/kg (oral- rat)
Rubidium-Carb.	Rb_2CO_3	45000 (20°C)	2625 mg/kg (oral - rat)
Rubidium-Bicarb.	$RbHCO_3$	97.6 (20°C)	NA
Cesium-Carb.	Cs_2CO_3	260.5 (15°C)	2170 mg/kg (oral - mouse)
Cesium-Bicarb.	$CsHCO_3$	209 (15°C)	NA
Calcium-Carb.	$CaCO_3$	0.0013 (25°C)	6450 mg/kg (oral - rat)
Calcium-Bicarb.	$Ca(HCO_3)_2$	16.1 (0°C) - 18.4 (100°C)	NA
Ammonium-Carb	$(NH_4)_2CO_3$	55.8 (0°C) - 100 (20°C)	1975 mg/kg (rat - oral)
Ammonium-Bicarb.	NH_4HCO_3	11.9 (0°C) - 109 (80°C)	1237 mg/kg (oral - rat)

Table 4: Solubility [120] and toxicity values [121] used for counter-ion estimation.

At certain temperature and pH, the conversion of bicarbonate to carbonate and back can be observed, which is why both types are listed in Table 4. Additionally, no toxicity reference data are available for lithium-, rubidium-, cesium-, and calcium bicarbonates. The comparison to the toxicity of the carbonate data gives a general indication about the toxicity of the corresponding alkali metal in the bicarbonate form. In other words, if the alkali carbonate is highly toxic, it is likely that the corresponding bicarbonate will behave in a similar way and should therefore be excluded.

The solubility analysis leads to the conclusion that the order of the alkali metal corresponds to the highest possible solubility. Only rubidium compounds do not follow this rule. This increased solubility can be explained by the increasing radius of the ions, which has an impact on the grid energy. Following the theoretical explanation (see chapter 2.2.2, equation (85)), the grid energy is directly connected to the charge and radius of the ions.

name	formula	ionic radius of alkali ion [pm]	grid enthalpy [kJ/mol]
lithium fluoride	LiF	74	1030
sodium fluoride	NaF	102	910
potassium fluoride	KF	138	808
rubidium fluoride	RbF	149	774
cesium fluoride	CsF	170	744

Table 5: Different alkali metals in fluorinated form. The grid enthalpy decreases with increasing ionic radius. Values from [112].

name	formula	cations	anions	grid enthalpy [kJ/mol]
sodium chloride	NaCl	Na^+	Cl^-	769
sodium sulfide	Na_2S	Na^+	S^{2-}	2192
magnesium chloride	$MgCl_2$	Mg^{2+}	Cl^-	2326
magnesium sulfide	MgS	Mg^{2+}	S^{2-}	3406

Table 6: Examples of salts with different charges. Increasing the charge leads to an increased grid enthalpy. Values from [112] and [122].

From Table 5 and Table 6 it can be derived that the ideal candidate for a counter ion for the bicarbonate should have a small charge and a large ionic radius. Combining all the criteria with a higher emphasis on the solubility, cesium ions exhibit all the required characteristics and the highest solubility, owing to the single positive charge, largest ionic radius, and medium toxicity. In comparison with sodium as counter ion, it is twice as toxic; on the other hand, its 13-fold higher solubility makes it a perfect candidate for quantification analysis at a highly SNR-limited experimental setup. In addition, very few ^{13}C-labeled compounds are commercially available, hence the synthesis is a significant criterion for choosing the cation. Cesium bicarbonate can be synthetized relatively easily, as shown in chapter 3.1.2. Moreover, other ^{13}C bicarbonate work has already been performed [53] with this counter ion and no negative impact on the hyperpolarized signals were reported. However, when using cesium as the counter ion, one should also consider filtration or replacing the ion with a less toxic equivalent when moving from preclinical to clinical application (see chapter 3.2.3).

3.1.2 ^{13}C-labeled Cs-bicarbonate synthesis

Previous work on pH mapping was performed either with sodium [92] or cesium [53] as counter ions. Regarding the SNR limits of a hyperpolarized experiment, it is desirable to achieve maximum concentration of the ^{13}C-labeled compound. The experimental solubility of Cs-bicarbonate showed 5 times higher values (6 mol/L) compared to Na-bicarbonate (1.2 mol/L) and hence, Cs-bicarbonate was used for pulse design, quantification experiments *in vitro*, and application *in vivo*. In contrast to ^{13}C-Na-bicarbonate (Sigma Aldrich, CAS: 87081-58-1), ^{13}C-Cs-bicarbonate is not commercially available and must be synthetized by neutralizing cesium hydroxide with ^{13}C-labeled carbon dioxide [123]. Therefore, two setups were designed: one for the synthesis and one for the lyophilisation of ^{13}C-labeled cesium bicarbonate. Lyophilisation is necessary to create samples with high bicarbonate concentrations. It is also advantageous for storage, since CO_2 release is prevented when the bicarbonate is kept in crystalline form.

1.3 g of cesium hydroxide monohydrate (Sigma Aldrich, CAS: 35103-79-8) was mixed with 20 ml of H_2O to a concentration of 0.389 mol/L. The solution was transferred to a three-necked round-bottom flask (see in Figure 11) via valve V3. A magnetic stirrer was added and set to maximum rotational speed to achieve turbulent mixing conditions in the cup and a maximized surface for gas exchange in the liquid phase.

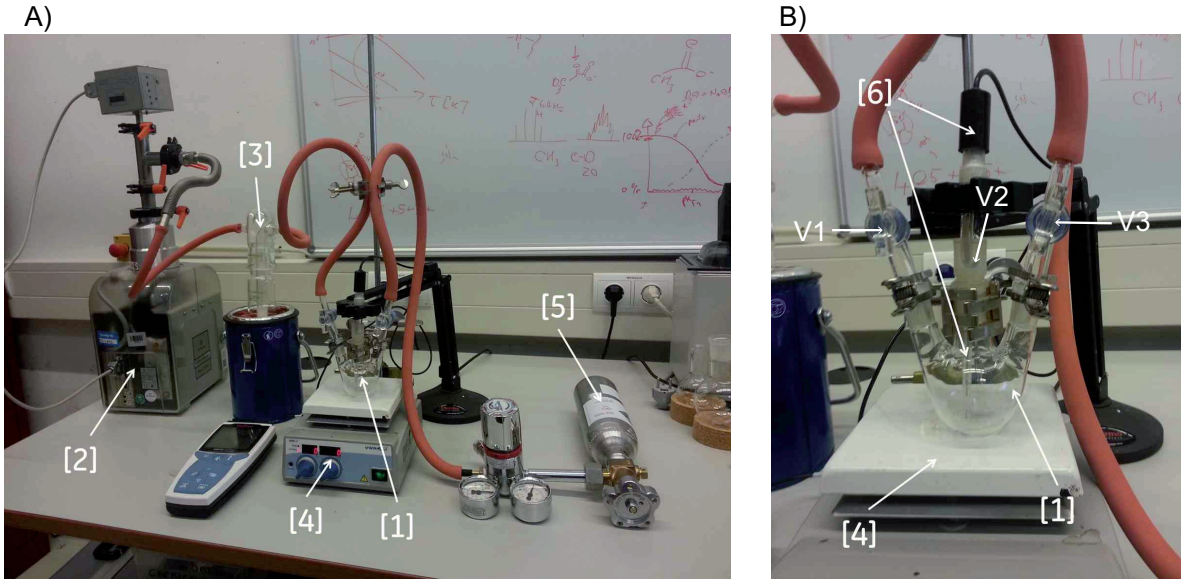

Figure 11: A) An overview of the setup used for the synthesis of ^{13}C-labeled Cs-bicarbonate. The main components include a three-necked round-bottom flask [1], connected via a flexible tube to a ^{13}C-labeled CO_2 bottle [5]. On the left side, a high-power vacuum pump [2] is connected via a flexible tube with a nitrogen-driven cold trap [3], interconnected between the flask and the pump to protect the vacuum pump from moisture damage. The flask is fixed upon a heatable magnetic stirrer [4]. B) A close-up view of the round flask, showing the three necks [V1-V3] with the regulating valves [V1] and [V3] at the left and right neck, correspondingly, for the regulation of the CO_2 gas and the vacuum. The central neck shows the connected pH meter [6].

The air was removed by a membrane vacuum pump. Subsequently, a CO_2-gas atmosphere was established with 99% ^{13}C-enriched CO_2 gas (Sigma Aldrich and Eurisotope, CAS: 1111-72-4) and the following neutralization reaction took place:

$$2\,CsOH + {}^{13}CO_2 \rightarrow Cs_2{}^{13}CO_3 + H_2O \quad (100)$$

Under further $^{13}CO_2$ administration, $Cs_2{}^{13}CO_3$ reacted with $^{13}CO_2$ and H_2O to produce two ^{13}C-cesium-bicarbonate molecules ($CsH{}^{13}CO_3$):

$$Cs_2{}^{13}CO_3 + {}^{13}CO_2 + H_2O \rightarrow 2CsH{}^{13}CO_3 \quad (101)$$

The progress of the synthesis can be tracked by measuring the pH. The initial pH of the cesium hydroxide solution was alkaline, with values of ~14. With further $^{13}CO_2$ gassing and the corresponding cesium bicarbonate synthesis, pH became more neutral. The reaction was finished when cesium hydroxide had been consumed and pH had a value of ~7. After the synthesis was completed, the solution was transferred to a 100 ml beaker and shock frozen in liquid nitrogen. The frozen sample was then transferred to the lyophilisation setup (Figure 12).

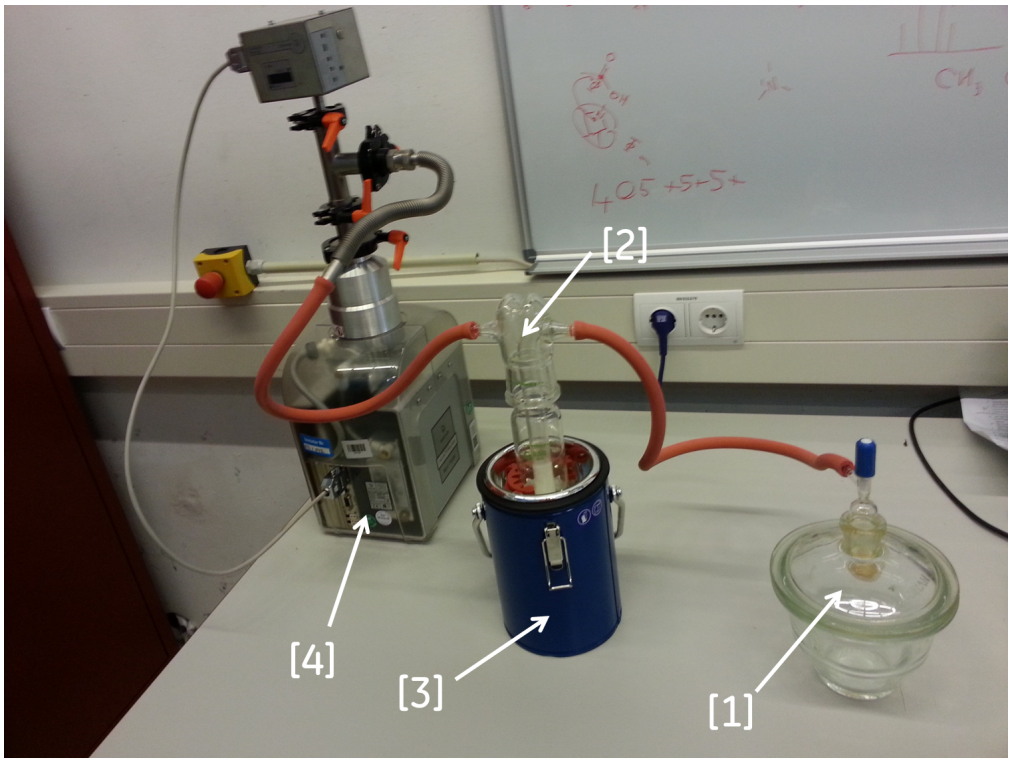

Figure 12: Lyophilisation setup for bicarbonate drying. A desiccator [1] is connected with a high-power vacuum pump [4] via flexible pipes. Between them, a cold trap is installed [2], which freezes the lyophilized liquid. For multiple sample drying, a vacuum splitter (not shown) can be installed (between [1] and [2]), dividing the vacuum into multiple desiccators and allowing the drying of up to 3 samples simultaneously.

The setup contained a high-performance vacuum pump (Varian Inc., California, USA), which was connected to a nitrogen cold trap. This was further connected to a valve-regulated vacuum splitter. Up to three desiccators were attached to the splitter to dry multiple samples simultaneously. One beaker was placed into each desiccator, which was set under vacuum of up to $2 \cdot 10^{-5}$ bar. During lyophilisation, the H_2O was removed completely from the sample, leaving a dry Cs-bicarbonate powder. To prevent the vacuum pump from damage, the nitrogen cold trap condensed the removed water and froze it before it reached the vacuum pump. After 48 h of drying, ~1.3 g ^{13}C-labeled cesium bicarbonate powder was collected. For storage, the powder was sealed gastight and deep-frozen.

The weight of $CsOH$ was 1.3 g and with $M_{CsOH} = 149.912 \frac{g}{mol}$, the amount of used $CsOH$ was $n_{CsOH} = 8.673\ mmol$. Calculating the theoretical outcome for 1 mol cesium hydroxide and a complete reaction leads to: $1\ mol\ CsOH \rightarrow 1\ mol\ CsHCO_3$. In other words, for every hydroxide molecule used, one bicarbonate molecule was gained. Hence, with $M_{CsHCO_3} = 193.922 \frac{g}{mol}$, the theoretically achievable weight of synthetized bicarbonate for a full reaction is $m_{CsHCO3} = 1.682\ g$. The difference between theoretical and practical outcome ranges between 100 mg and 300 mg. Partial residues of bicarbonate powder in the flask that cannot be collected after the drying process can mostly explain the disagreement between the theoretical weight and the measured weight. Additionally, the reaction might not have been be fully completed, which was indicated by a slightly alkaline pH of ~8 after dissolving the

gained bicarbonate powder in H_2O. Since the bicarbonate solution had a neutral pH at the end of the CO_2 application, the pH drop could be explained by CO_2 release during lyophilisation and subsequent cesium hydroxide formation.

3.1.3 Gd and OXO

Samples prepared for hyperpolarizing purposes usually contain T_1 relaxing agents, like the OXO63 radical or gadolinium compounds. These impact the relaxation rates of the electrons involved in the hyperpolarization process, allowing the more efficient transfer of polarization from the electrons to the nuclei. For solid-state hyperpolarization, it is desirable to work in a power-saturated regime. This can be confirmed by sweeping the power of the microwave source at resonance frequency for different power levels. When no changes are observable in the hyperpolarized signal, the power-saturated regime is achieved. By reducing the relaxation rates of the electrons, the electrons are able to relax back faster to their initial state, from which they can again transfer polarization to the nuclei. However, increased radical and gadolinium concentrations also increase the T_1 relaxation of the corresponding nuclei after dissolution. This leads to a reduced T_1 decay, which in the end can lead to an overall signal loss at the time point of measurement. Careful investigations during sample preparations are needed to find an optimum solution for this inherent tradeoff between efficient solid-state buildup and increased liquid state decay.

3.1.3.1 *OXO radical*

The OXO63 radical concentrations were optimized for hyperpolarized ^{13}C-Cs-bicarbonate samples. The samples were prepared in 80%/20% glycerol/D_2O. Different batches with OXO concentrations ranging from 14 mmol/L to 69 mmol/L were prepared and analyzed in terms of solid-state buildup, liquid-state decay, and the influence on polarization level and T_1. 50 µl of the prepared samples were hyperpolarized and subsequently dissolved. Since the OXO radical itself has a dark green color, samples of different concentrations can be differentiated by visual inspection (see Figure 13). The goal of the study is to achieve maximum signal within the appropriate solid-state buildup time for *in vivo* experiments of $\leq$ 90 min.

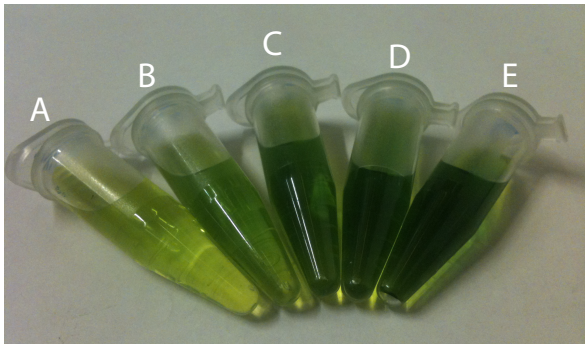

Figure 13: Dissolved samples of ^{13}C-Cs-bicarbonate with different OXO concentrations. A: 14 mmol/L; B: 28 mmol/L; C: 42 mmol/L; D: 55 mmol/L; E: 69 mmol/L.

The solid-state signal was measured by low flip-angle excitation and free induction decay (FID) readout. The influence of increasing the OXO concentrations to the solid-state level

confirms its T_1 relaxing properties (see Figure 14). For concentrations ≥ 42 mmol/L, the maximum polarization level was reached after 30 minutes of polarization. However, the maximum signal amplitude was half of that of the samples with lower radical concentrations. The low concentration of 14 mmol/L shows that 95% of the maximum polarization level was not achieved after 2 h of polarization.

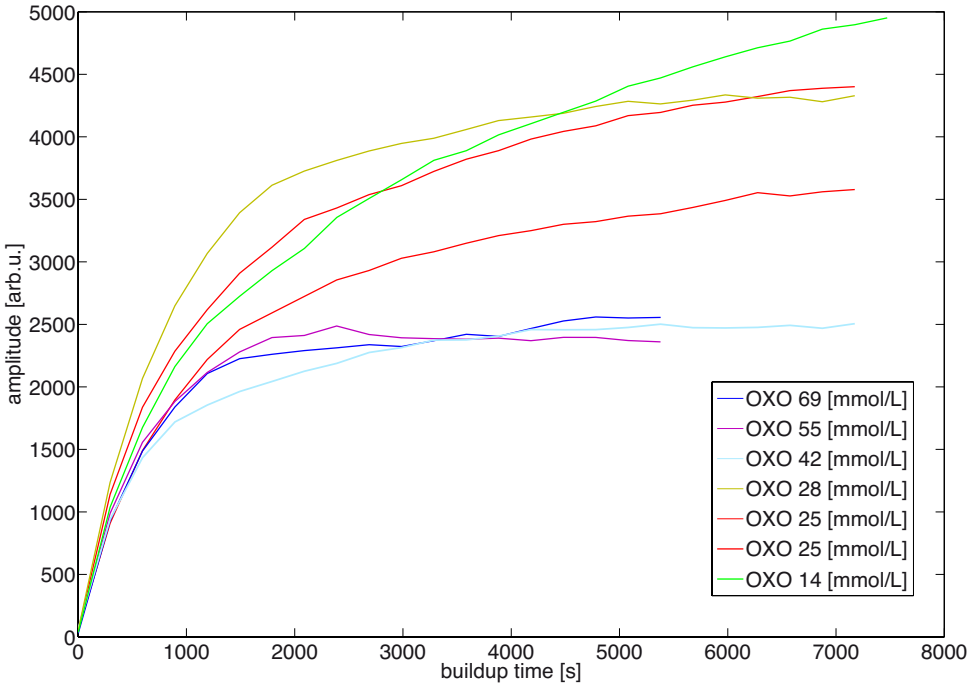

Figure 14: Hyperpolarized signal buildup for different OXO concentrations. Increasing the OXO concentrations affects the buildup time. The signal approaches a maximum in the polarization level. The maximum polarization is larger for lower radical concentrations. However, it takes longer time to achieve the maximum. The solid-state buildup for OXO concentrations of 55 mmol/L and 69 mmol/L was aborted after 90 minutes because the maximum level of signal increase was achieved.

The decreased buildup time can be expressed by the buildup constants of the exponential fits to the corresponding OXO radical concentrations and are shown in Figure 16. The buildup constants approach a maximum of 550 s, which is estimated as the limit of the solid-state buildup. Adjusting the radical concentrations to higher values would not decrease the buildup time.

The solid-state buildup signal (s_{solid}) can be calculated by the following equation:

$$s_{solid}(t) = s_{max} \cdot \left(1 - e^{-\frac{t}{s_{const}}}\right) \quad (102)$$

With s_{max}=1 for full polarization and s_{const} for the corresponding solid-state buildup constant. The results of the simulation for different buildup constants are displayed in Figure 15.

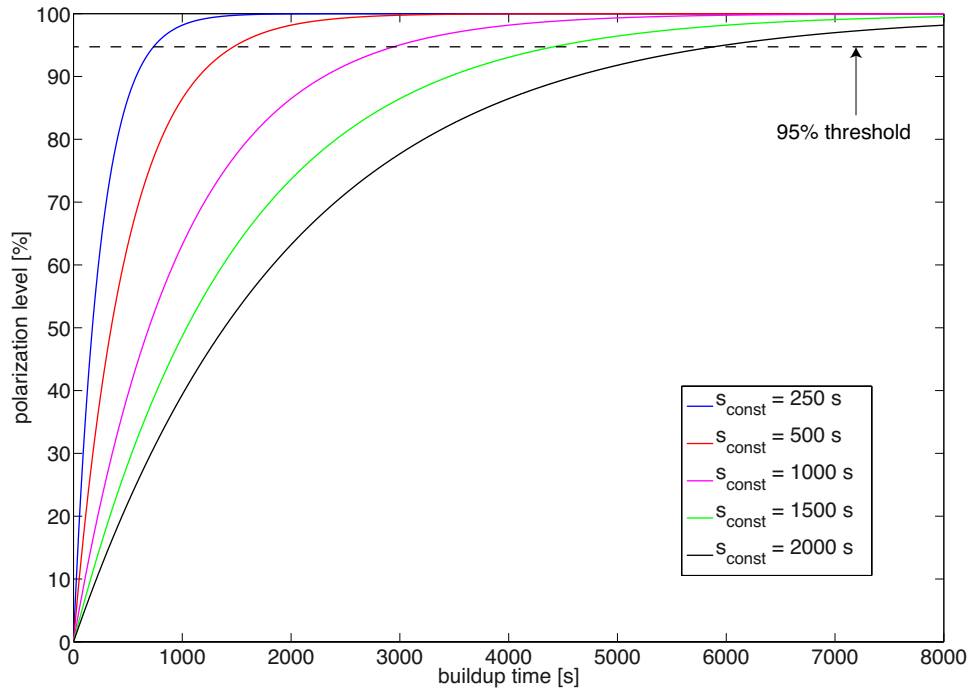

Figure 15: Simulated solid-state buildup with varying buildup constants. The horizontal axis depicts the time of hyperpolarization. The vertical axis shows the achieved polarization level. The dotted line depicts the 95% polarization level threshold, after which dissolutions were performed. For all simulated polarizations, a maximum polarization of 1 (≈ 100% polarization level) can be achieved. However, in real samples, these maximum achievable values differ. This value can be influenced by, e.g., sample volume and concentrations of OXO63 radical and Gd.

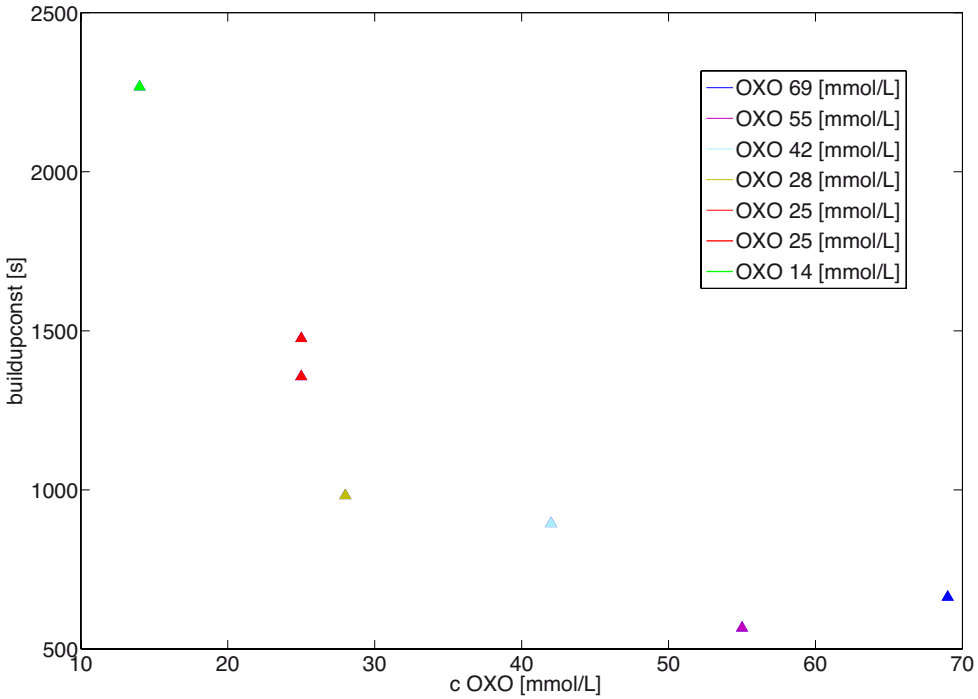

Figure 16: Different buildup constants (y-axis) of the hyperpolarized solid-state signal as a function of the concentration of the OXO radical (x-axis). It can be seen that the buildup constants decrease with increasing OXO concentrations and they approach a maximum of 550 s.

The samples were dissolved with a dissolution agent containing D_2O and EDTA (0.1 g/L). Measurements of the liquid-state signal were performed at the 1 T Bruker Minispec

spectrometer. The subsequent data analysis revealed the polarization level of the hyperpolarized compound in the liquid state (see Figure 17).

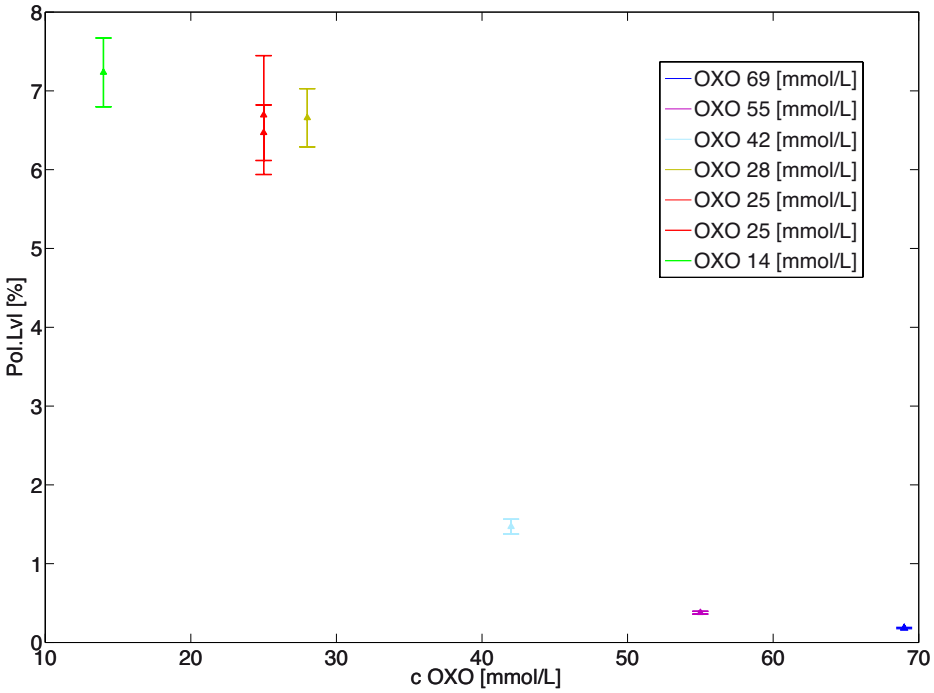

Figure 17: Polarization levels of hyperpolarized ^{13}C -Cs-bicarbonate (y-axis) for different OXO radical concentrations (x-axis). Increasing the OXO-radical concentration significantly decreases the polarization level. By increasing the radical concentrations from 14 mmol/L to 28 mmol/L, only small changes in the polarization level can be observed, from 7.2% to 6.7%. Further increase to 42 mmol/L leads to a substantial drop in polarization level to 1.5% and further decrease with increasing concentration.

The considerable drop in signal intensity limits T_1 determination in the Minispec to concentrations $\leq 28\ mmol/L$; the corresponding values are given in Table 7.

OXO63 [mmol/L]	14	25	25	28	42
Liquid state T_1 [s]	136.5 ± 5.0	120.6 ± 2.5	118.1 ± 3.5	120.4 ± 3.5	118.5 ± 6.7

Table 7: T_1 decay of hyperpolarized ^{13}C -Cs-bicarbonate dissolved in D_2O for different OXO-radical concentrations. The error was calculated using 95% confidence boundaries for the mono-exponential fit. The T_1 estimation with different OXO concentrations shows a decrease of T_1 with increasing OXO concentration. The T_1 estimation was performed disregarding larger OXO concentrations ($\geq 42\ mmol/L$), because the error increases significantly for large concentrations owing to low SNR.

The T_1 values slightly decrease for radical concentrations $\leq 28\ mmol/L$. The optimal OXO63 radical concentration was calculated to be between $20\ mmol/L$ and $25\ mmol/L$. Hyperpolarization was $\geq 95\%$ for the high solid-state polarization signals and the overall polarization level was only slightly decreased. T_1 remained high enough to maintain sufficient signal during transport from the polarizer to the MR scanner. All hyperpolarized experiments for *in vitro* or *in vivo* measurements were conducted in the above-mentioned range of radical concentrations.

3.1.3.2 *Gadolinium*

After the optimal radical concentration was found, subsequent investigations were performed on different gadolinium concentrations, ranging from 0 $mmol/L$ to 3.5 $mmol/L$. Similar to the OXO radical investigations, the effects of gadolinium on solid-state buildup and liquid-state decay were determined. It is important to mention that all experiments were performed using gadoteric acid, where gadolinium is chelated by 1,4,7,10-tetraazacyclododecane-1,4,7,10-tetraacetic acid (DOTA). Hence, all listed gadolinium concentrations refer to the concentrations of the non-toxic contrast agent (DOTAREM, ProHance).

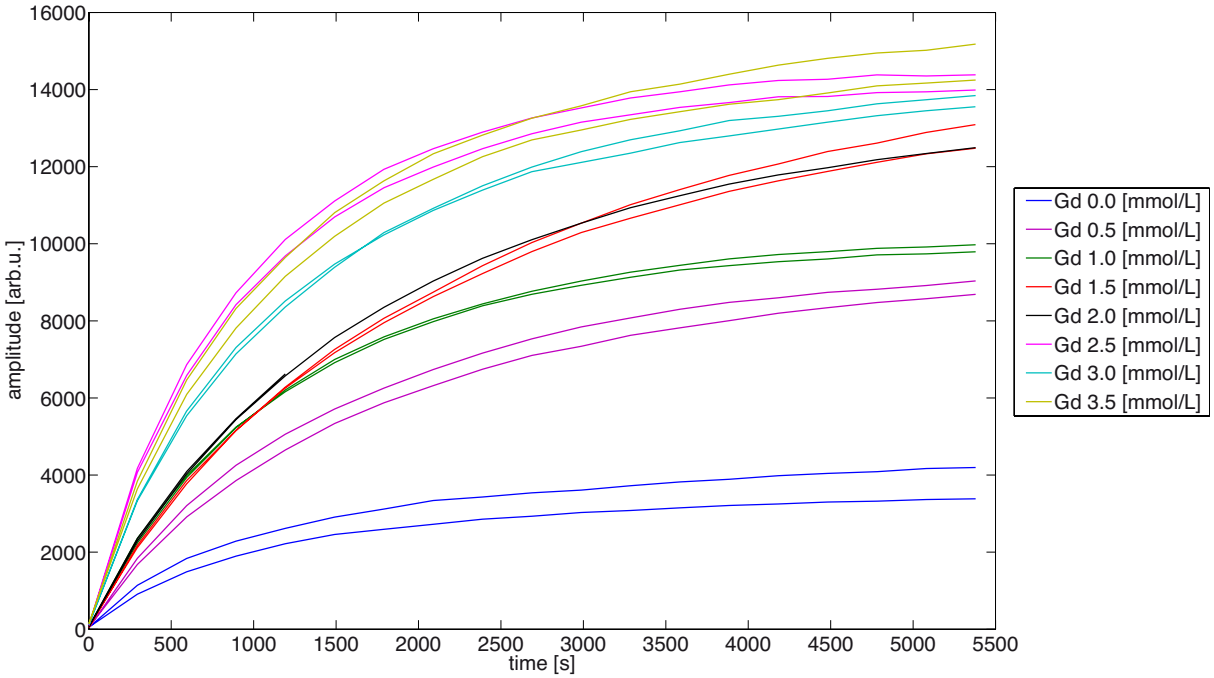

Figure 18: Hyperpolarized signal buildup for different Gd concentrations. The gadolinium concentrations vary from 0 to 3.5 mmol/L. Increasing the Gd concentrations affects the buildup time. The signal approaches a maximum at the polarization level. For larger Gd concentrations, the maximum polarization is larger; however, it takes longer to reach the maximum. The maximum hyperpolarized signal is significantly increased (≥ factor 4) with the use of gadolinium. Good reproducibility of two measurements with the same Gd concentration can be observed. After $t = 90$ minutes, the buildup was stopped and subsequent dissolution was performed.

All Gd concentration experiments were performed with double-dissolution experiments to confirm their reproducibility. Figure 18 shows a direct influence of Gd on both the solid-state buildup time and the maximum hyperpolarized signal achieved. It has a significant impact on the hyperpolarized signal, as it improves the maximum signal intensity by a factor of ≥4. The signal increases even at low Gd concentrations and the enhancement approaches a maximum for Gd concentrations ≥ 1.5 mmol/L. In contrast to the increased OXO radical concentration, Gd shows no clear trend when investigating the concentration dependency of the solid-state buildup constant (see Figure 19) and liquid-state polarization levels (see Figure 20).

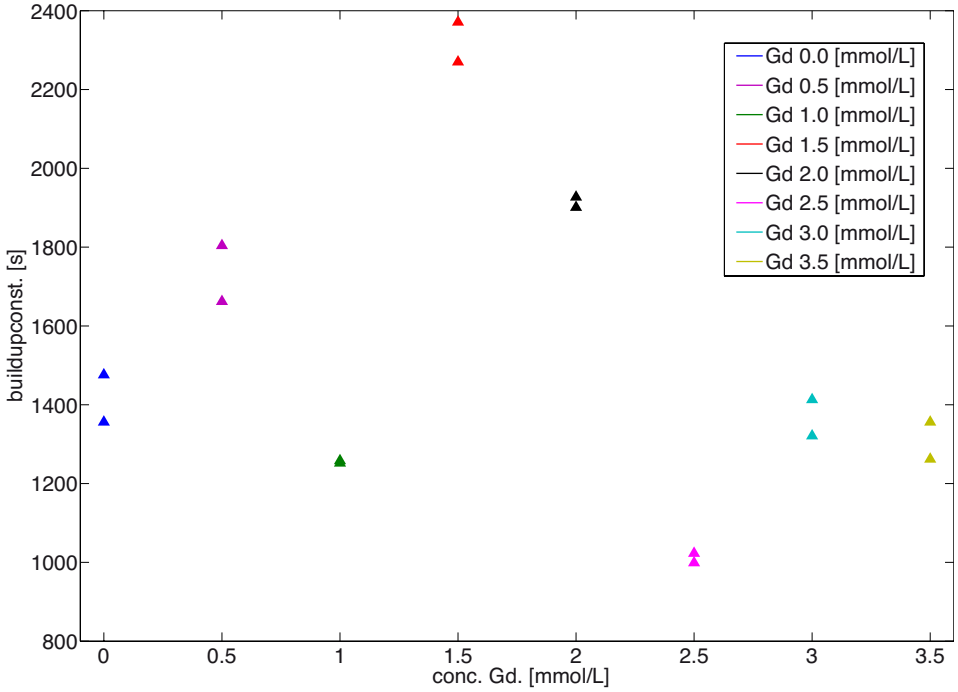

Figure 19: Influence of different Gd concentrations (x-axis) on the solid-state buildup constant (y-axis). Compared to the sample with no Gd added, the buildup constant changes but shows no clear trend with varying Gd concentration. However, the reproducibility of every investigated Gd concentration can be confirmed.

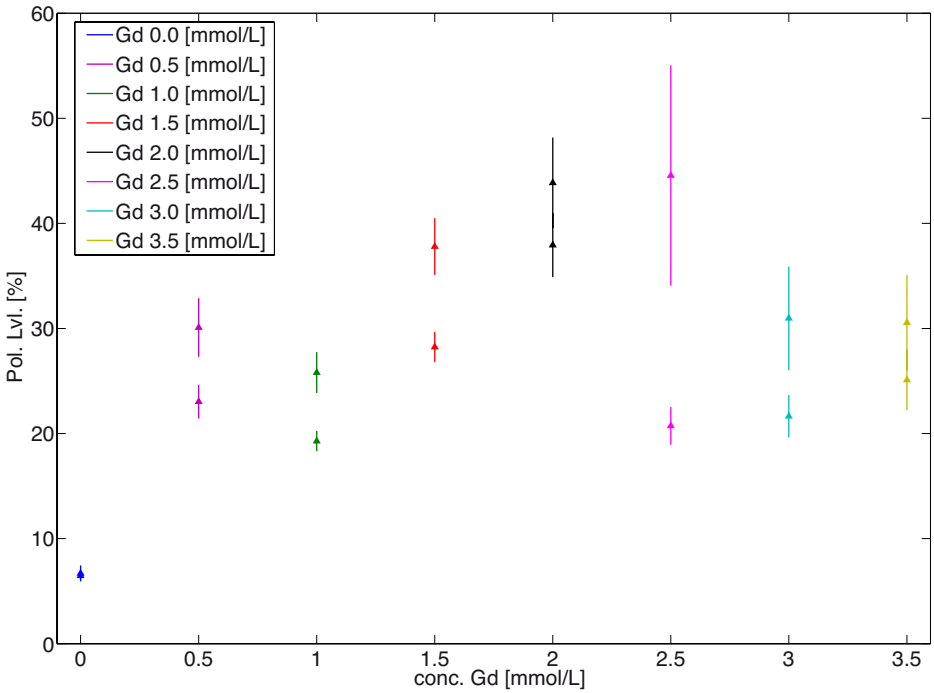

Figure 20: Polarization levels (y-axis) of hyperpolarized ^{13}C -Cs-bicarbonate for different Gd concentrations (x-axis). Comparing the polarization level of 6.4% without Gd with the polarization levels where Gd was added, a significant increase can be observed (factor ≥ 3). Some polarization level estimations show large errors, especially compared to the calculated polarization level without any Gd, which are mainly due to the thermal measurements, where a decrease in T_1 increases the error in the polarization level estimation. No trend can be seen with increasing Gd concentrations. The measured polarization levels are distributed around 25% - 30% and are already achieved for the smallest investigated concentration (c = 0.5 mmol/L).

However, plotting the buildup constants versus the achieved polarization levels leads to an increased polarization level with increasing buildup constant (see Figure 21).

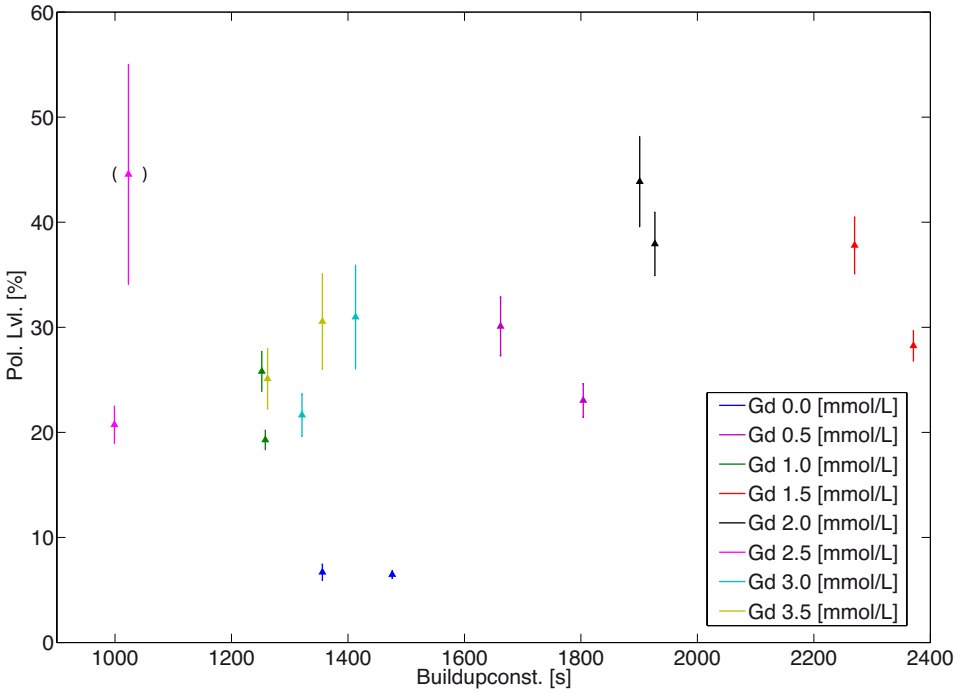

Figure 21: Liquid-state polarization levels (y-axis) for different Gd concentrations, plotted against their corresponding buildup constants (x-axis). Neglecting the large-error measurement in brackets and the measurements without any Gd, an increase in polarization level with increasing buildup constant can be confirmed.

In conclusion, a higher final polarization level can be achieved by a longer polarization time for the case when the maximum level is not reached. As can be seen from Figure 18, all solid-state polarization buildups were performed until $t = 90$ minutes and subsequently, dissolution was performed.

As mentioned above, Gd has a direct influence on the T_1 relaxation time. On the one hand, this allows a more efficient solid-state polarization, on the other hand, it increases the T_1 signal decay in the liquid state. This is demonstrated in Figure 22. Increasing the Gd concentration from 0 to 3.5 mmol/L significantly decreases T_1 from 120 s - 130 s to 60 s - 70 s, measured in D_2O and 1 T.

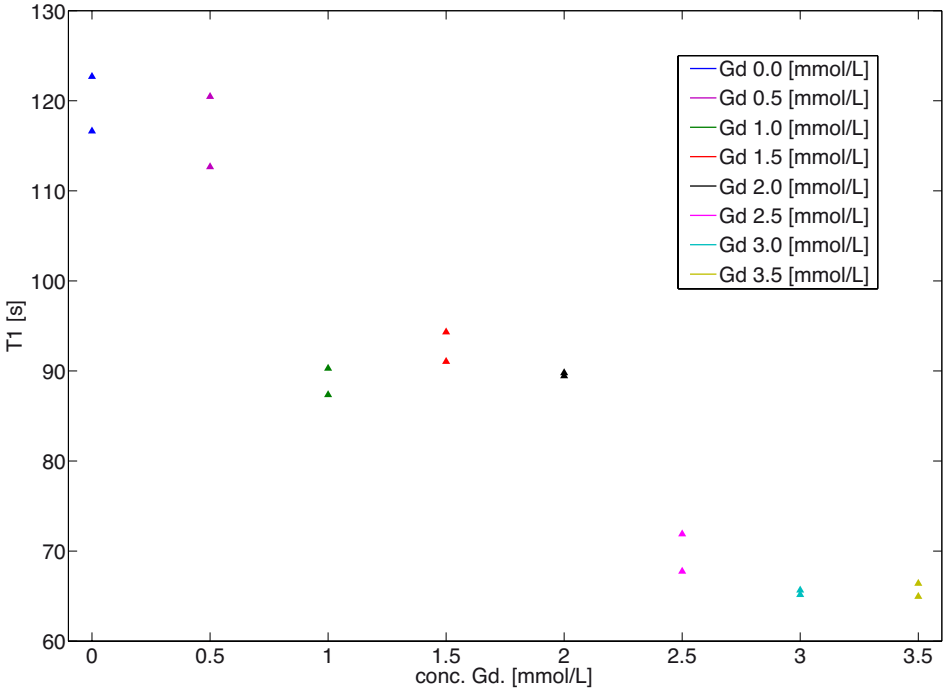

Figure 22: T_1 relaxation constants (y-axis) in the liquid state for different Gd concentrations (x-axis). T_1 decreases with increasing Gd concentration, measured at 1 T in D_2O.

Adding Gd considerably increases the polarization level, even at low concentrations. From these results, it can be seen that solid-state polarization buildup is sufficiently fast for all investigated values. With regard to the T_1-decreasing effect of Gd, the optimum value was found at the lowest investigated Gd concentration of 0.5 mmol/L.

Hence, the final optimum composition was determined as 25 mmol/L OXO radical and 0.5 mmol/L Gd. This ratio provides sufficiently fast solid-state buildup ($\approx$ 90 min), high polarization level ($\sim$19% - 21%), and the appropriate T_1 ($\sim$120 s) for signal conservation during transport from the polarizer to the scanner. The transport time ranges from 12 s to 240 s, dependent on the experimental setup.

It must be noted that this chemical formulation shows best performance for sample volumes up to 250 µl. As discussed in chapter 3.2.2 larger sample volumes lead to an increased concentration of OXO and Gd in the dissolved solution, which could lead to a significant drop in T_1 and the polarization level, which must be considered when performing larger sample volume experiments.

3.2. Optimizing dissolution

3.2.1 Signal loss due to buffer pH and temperature

Optimizing the dissolution agent is the second step to optimize SNR. To increase T_1, a D_2O-based dissolution agent is advantageous. For the subsequent *in vivo* experiments, a pH buffer is needed to adjust pH and osmolality to physiological levels. Because the bicarbonate itself is a pH buffer and the pure Cs-bicarbonate dissolution has a pH of around 8.2 to 8.4, the final pH needs to be adjusted with the dissolution agent buffer. The main issue of this process is the preservation of the bicarbonate signal. The lower the pH becomes, the more CO_2 is produced (see Henderson-Hasselbalch equation (1)), which can easily evaporate during the dissolution process as depicted in Figure 23. The dissolution process at the HyperSense polarizer was explicitly designed as a turbulent process that allows rapid dissolving. This, of course, leads to an increased CO_2 loss. Furthermore, one must take into account that the dissolution liquid is heated up to 168°C. Depending on which pH buffer is used, pKa, and thus pH, changes with temperature. The change in the used phosphate buffer [124] is described as:

$$pH = pH_{start} - 0.0028 \cdot \Delta temp \qquad (103)$$

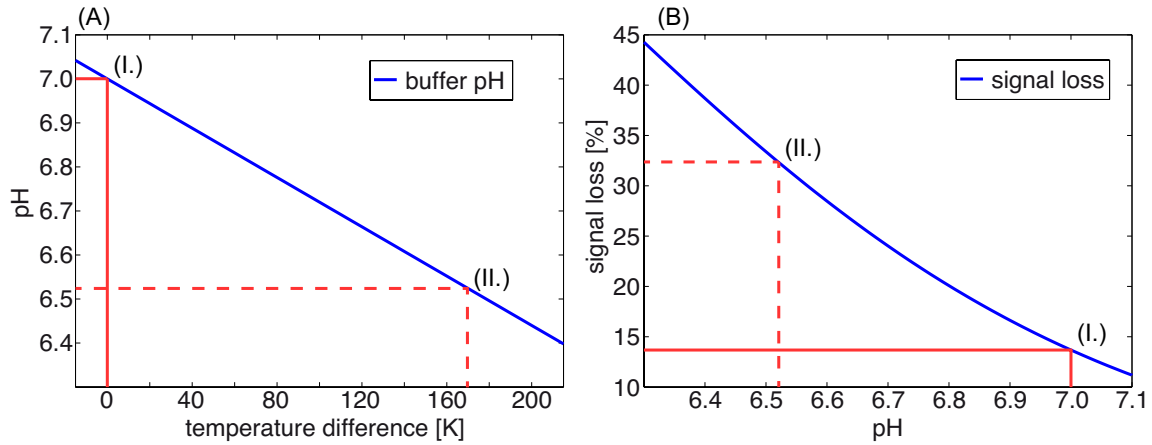

Figure 23: (A) The pH change of the phosphate buffer used as dissolution agent, which is assumed to have pH=7 at room temperature (solid line). Increasing the temperature during the dissolution process leads to a decrease in pH (dashed line). (B) The signal loss at room temperature (solid line) and at dissolution temperature (dashed line), assuming that all CO_2 generated because of the pH decrease is removed. Signal loss increases from 13.7% at room temperature to 32.4% at dissolution temperature.

where $pH_{start} = 7$, as a pH-neutral buffer is assumed. The signal loss is calculated by expressing the Henderson-Hasselbalch equation as:

$$sig_{loss} = \frac{100}{sig_{CO2} + 10^{pH-pKs}} \qquad (104)$$

with $10^{pH-pKs} = sig_{BiC}$ being the signal of the bicarbonate, $sig_{CO2} = 1$ the signal of the CO_2, sig_loss the percentage of CO_2 contributing to the overall signal, and $pKs = 6.2$, as it is assumed to be *in vivo* [53,54]. When pH decreases, the contribution of the CO_2 to the

overall signal increases. Hence, the possible loss due to evaporation has a higher probability. This loss is assumed to be a full removal of the CO_2 after equilibrium is established. This assumption is simplified owing to the fact that the buildup at equilibrium is a permanent and dynamic process, dependent on the enzymatic activity of the environment. Additionally, the evaporation dynamics changes during the dissolution process. Nonetheless, the above assumptions show that there is a significant impact of the temperature on the dissolution agent, which was taken into account when preparing it.

3.2.2 Polarizer modifications

To increase the amount of dissolved bicarbonate in the polarizer, modifications of the dissolution process were performed. The changes affect the standard Hypersense DNP polarizer, located at the GE Global Research Center in Munich. A second modified polarizer was used, located at the Technical University of Denmark, Lyngby, Copenhagen in the laboratories of Prof. Jan Henrik Ardenkjær-Larsen to evaluate performance changes based on changed settings, which are not tunable on the standard model.

The standard DNP Hypersense polarizer operates with a pressure-regulated heat bomb, where the dissolution agent is heated up to 168°C. The temperature is measured indirectly by a pressure sensor, which translates the pressure measured during the dissolution process into temperature. At the beginning of the dissolution process, the pressure sensor showed a pressure of 10 bar, which is equivalent to a temperature of 168°C for heated aqueous solutions. Since the default parameters of standard models cannot be changed without losing the warranty, changes of pressure and heating cannot increase the maximum volume of the dissolved sample, and the amount of dissolution agent in the polarizer is limited to 10 ml. However, lower volumes are usually used, since not all of the hyperpolarized liquid can be utilized in *in vivo* experiments. The minimum volumes used for rat experiments are:

$$V_{min} = V_{inj} + V_{spec} + V_{pH} + V_{loss} \quad (105)$$

with injection volumes (V_{inj}) of 1-2 ml, depending on the rat weight (200-400 g), volume for the Minispec measurement (V_{spec}) of 1 ml, volume for pH and later osmolality determination (V_{pH}) of 1 ml, and a volume that is lost during the experiments due to the dead volumes of the polarizer, syringes, and tubes used for injection (V_{loss}) of around 0.5 ml - 0.7 ml. The use of more dissolution agent (up to 10 ml) would be possible, but it would also prolong the dissolution process and increase the amount of unused hyperpolarized substance. Since these values vary with experimental setup and procedure, the dissolution of the bicarbonate was optimized for a maximum volume of dissolution agent of 5 ml. The aim of the optimization process is to achieve a complete dissolution with no residual bicarbonate sample remaining in the sample cup (see Figure 25). The dissolution process of the frozen sample is difficult because most of the hyperpolarized signal is lost, dissolving in the wrong way. Dissolving the sample just by removing the frozen, hyperpolarized sample from the polarizer and dissolve it manually results in a complete signal loss. This technical issue was first solved by *Ardenkjaer-Larsen* in 2003 [11]. The remaining bicarbonate in the sample cup not only reduces the amount of dissolved bicarbonate, but it also shows a significant impact on the

polarization level in the liquid state. Hence, the goal of the optimization process was to achieve complete dissolution of the bicarbonate sample with 5 ml of dissolution agent.

3.2.2.1 *Evaluation at modified Hypersense DNP polarizer*

As mentioned, standard Hypersense DNP polarizers pose limitations to the variation of their parameters. Hence, a modified version of a polarizer was used. Spectral analysis of the dissolved compound was performed using a 9.4 T Varian spectrometer. This setup was used to investigate the possibility of increasing the dissolved bicarbonate concentration and investigate all relevant parameters (T_1, polarization level). The modified version of the polarizer allows increasing the temperature and pressure of the dissolution agent. The line widths of the 400 MHz scanner were measured with 2 Hz of the CO_2 resonance peak and 6 Hz of the bicarbonate resonance peak. The polarization level was measured with 19% and the T_1 decay was 34 seconds at 9.4 T for a 50 µl sample dissolved with 5 ml H_2O + EDTA (0.1 g/L). Subsequently, the increase of the dissolved bicarbonate concentration was tested by increasing the temperature from 168°C to 200°C. By changing the parameters, the dissolved amount of bicarbonate could be increased to 500 µl and dissolved successfully with 5 ml of dissolution agent. This caused an increase of the maximum dissolved bicarbonate concentration to 300 mM. Despite the fact that the solid-state polarization was the same for small volumes (3162 arb. u. with 50 µl) and big volumes (31897 arb. u. with 500 µl), the liquid-state polarization level dropped from 19% to 11%. An explanation for this behavior is that such large amounts of bicarbonate are dissolved in a non-optimal way. Improvement of the dissolution process can be achieved by pre-freezing the sample to droplets before hyperpolarization (see Figure 25). Another observation was made for the decay of the T_1 relaxation, which decreased from 34 s to 6.8 s. Because a T_1 of 6.8 s would negate the benefit of a higher bicarbonate concentration, further experiments were performed to investigate the source of the T_1 drop.

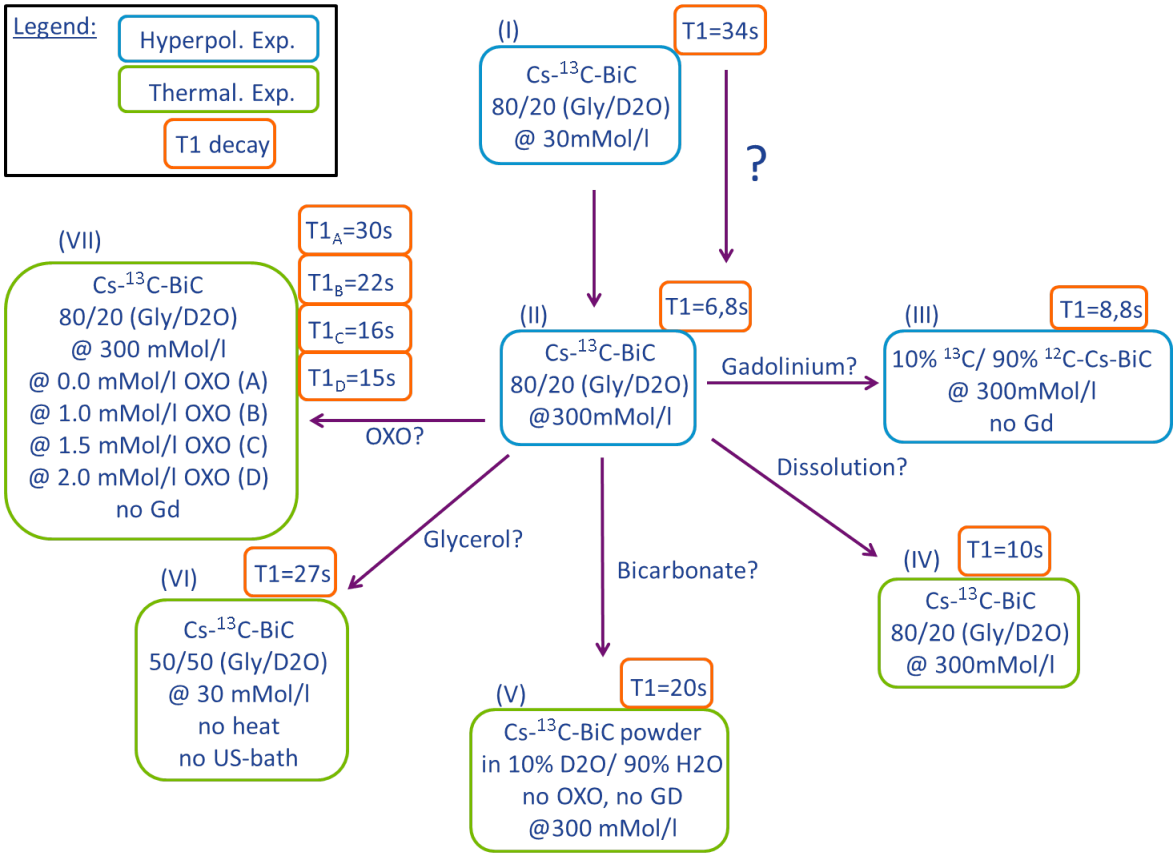

Figure 24: Bicarbonate (BiC) concentration increase experiments investigating the T_1 decay and the polarization level.

Figure 24 depicts the experimental workflow of the T_1 investigation. The larger boxes show key parameters for each experiment. The measured T_1 is shown for each experiment, indicating whether T_1 was measured with a hyperpolarized experiment (blue frame) or with a thermal measurement (green frame). All experiments were performed at a 400 MHz Varian spectrometer. In hyperpolarized experiments, T_1 was measured with a low flip-angle excitation approach. The thermal T_1 measurements were performed with an inversion recovery pulse sequence using adiabatic pulses. The pulse used was a hyperbolic secant pulse with a length of 400 µs.

The first observation was the change in T_1 from low concentration and high T_1 (I) to high concentration and low T_1 (II). Subsequent experiments conducted for each parameter that could influence T_1 are displayed clockwise in Figure 24.

(I): Starting at the top, the original recipe (20 mmol/L OXO, 0.5 mmol/L Gd) is presented, where 50 µl bicarbonate was dissolved in 5 ml DA (water + 0,1 g/L EDTA), showing a T_1 of 34 s. (II): Using the same bicarbonate batch, dissolving 500 µl decreases the T_1 to 6.8 s. (III): The increase of the dissolved sample causes a higher gadolinium concentration and a higher OXO radical concentration. Both are substances that are essential for the polarization buildup process. In order to exclude Gd as the source of the T_1 decrease, a 10% ^{13}C/ 90% ^{12}C-Cs-bicarbonate sample was prepared at a concentration of 300 mM without Gd and was subsequently hyperpolarized and measured. The T_1 value of 8.8 s shows that also the Gd could not be the main source of the strong T_1 decrease. (IV): Subsequently, the dissolving

process was investigated as the source of T_1 shortening. A sample was prepared with the same chemical composition as a regular dissolved one, but during the dissolution process, no high temperature and pressure were applied. A thermal measurement showed T_1 of 10 s; therefore, the dissolving process could be excluded as the source of the T_1 decrease. (V): To eliminate the used self-synthetized ^{13}C-Cs-bicarbonate as the source of the small T_1, a thermal measurement was performed using 13 M Cs-BiC, dissolved in D_2O only, without Gd and OXO. The measured T_1 value was 20 s. (VI): To exclude the influence of the preparation procedure on the chemical properties of the bicarbonate and the glycerol, during which a heat gun and an ultrasound bath at 60°C were used to prepare the sample, a sample with lower glycerol concentration was produced without any heat processing or ultrasound bath, which led to a T_1 of 27 s. (VII): The relaxivity was also increased by the trityl radical OXO63, whose concentration was 0.17 mM in the 50 µl sample and 1.7 mM in the 500 µl sample. OXO63 should increase the relaxivity of the ^{13}C atom by 0.01 mM^{-1} s^{-1}. This should decrease the T_1 from ~30 s to ~20 s and cannot explain the significant decrease in T_1. To evaluate the influence of the radical in high field, thermal T_1 measurements were performed at different OXO concentrations ranging from 0 to 2 mM. T_1 dropped from 30 s to 15 s, which is still more than 2 times higher than the observed T_1 of 6.8 s and can therefore not be the only cause of the T_1 drop. The reproduction of consistent values for this series of measurements performed at high field failed and therefore, the measured T_1 should be treated with caution.
Considering that the relaxivity increases more at low field strengths, field cycling experiments were performed to evaluate the low-field influence of OXO to the T_1. No consistent reproducible T_1 data could be acquired and further investigations need to be performed on that issue.
Finally, the reason of the unexpected large T_1 decrease could not be completely determined. One assumption could be the interplay of the different parameters. Additionally, chemical shift anisotropy due to the increased viscosity of the higher concentrated sample could be an alternative explanation.

3.2.2.2 *Evaluation at standard Hypersense DNP polarizer*

The evaluations at the modified polarizer show that it is possible to increase the concentration up to 500 µl with increased pressure and temperature. However, some of the tested techniques, such as pre-freezing of the sample to beads (see Figure 25), can also be applied to the standard version of the polarizer. A larger surface and space between the beads leads to more efficient dissolution.

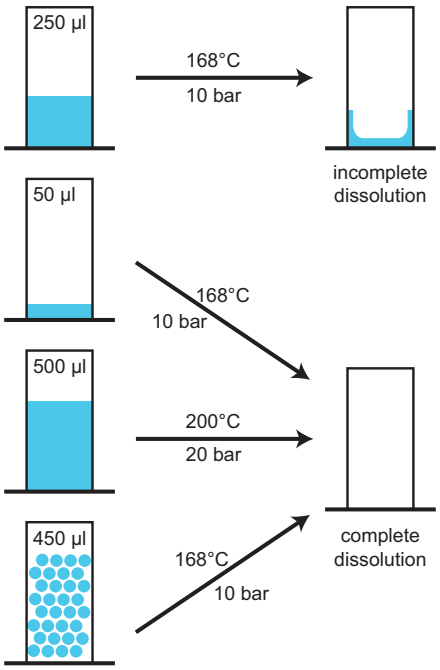

Figure 25: Experimental scheme of different sample volumes of bicarbonate and subsequent dissolution in 5 ml dissolution agent. The parameters of the dissolution are displayed by the arrows pointing to the results, which indicate whether the dissolution was successful or not.

The pre-freezing bead technique was successfully tested with different volumes of 7 µl and 12 µl per bead. Both sizes showed the same values for polarization levels after complete dissolution, therefore, the bigger bead volume size was used. Performance tests showed an increase of up to 450 µl of the bicarbonate sample dissolved at standard conditions of 10 bar pressure and 168°C temperature of the dissolution agent. This limitation is posed by the limited sample cup size. The large sample cups allow a maximum sample volume of 1 ml. The use of small beads increases the volume of the bicarbonate sample in the cup and the limit of 1 ml is reached with only 450 µl of sample. However, the polarization level showed again a decrease from 19% to 5-6%. Hence, an optimum solution for this tradeoff (higher concentration versus higher polarization level) was found by using 250 µl dissolved sample with 5 ml dissolution agent, which achieved a polarization level of 11% at a dissolved bicarbonate concentration of ~250 mmol/L.

The standard HyperSense DNP polarizer operated at $\sim 3.35\ T$ and $\sim 1.4\ K$. The microwave irradiation frequency varied depending on the molecule, and for ^{13}C-bicarbonate, it was $94.111\ GHz$. Achieving the correct irradiation frequency is important, since it influences the maximum polarization level and polarization buildup time. Usually, the power of microwave irradiation is selected to be in a power-saturated region and for ^{13}C-bicarbonate, it was $\sim 100\ mW$.

3.2.3 Filtration

One source that has a significant impact on T_1 decay is the paramagnetic influence of the OXO63 radical. This radical is necessary for hyperpolarization and was applied in concentrations of 20-25 mmol/L. To avoid its reduction effect on T_1, it would be preferable to

remove the radical as soon as possible after dissolution. Previous attempts were made to remove the radical from the dissolved liquid using ascorbic acid [125]. Additionally, the cesium ion has an impact on the signal parameters (e.g., T_1 relaxation) as well as biological effects [126,127]. Thus, its removal is necessary to overcome cesium influences to organ functionality with regard to later clinical studies. Because Cs is needed as a counter ion for the synthesis, which allows the preparation of a highly concentrated bicarbonate solution, it should be removed before the injection and exchanged with less toxic counter ions to form sodium bicarbonate with a low LD50 of 4220 mg/kg (oral - rat [128]).
For this purpose, filtration experiments were performed using the modified Hypersense DNP polarizer with subsequent evaluation at a 9.4 T Bruker spectrometer. The hyperpolarized bicarbonate dissolution liquid was dissolved and cleared by anion- and cation-exchange columns. The polarization levels and T_1 were analyzed to evaluate the impact of filtration to the standard procedure.

3.2.3.1 *Cesium*

The cesium concentration was detected with a tunable probe at the ^{133}Cs resonance frequency. To remove the cesium, a cation-exchange column (DOWEX 50WX8, Dow Chemical Company, Midland, US) with a mesh size of 200-400 was used in hydrogen form. The resins used were based on a microporous copolymer of styrene and divinyl benzene with 8% cross linkage between the divinyl benzene in the copolymer. In this form, the affinity of the column to cations is as follows:

$$H^+(1.0) > Na^+(1.5) > NH_4^+(1.95) > K^+(2.5) > Rb^+(2.6) > Cs^+(2.7).$$

The numbers in brackets show the relative selectivity. Hence, in the hydrogen form, the affinity of the mesh is 2.7 times higher for cesium than for hydrogen. The cesium concentration decreased from 0.5 mmol/L to below the detection limit of the scanner and is therefore assumed to be successfully cleared (see Figure 26).

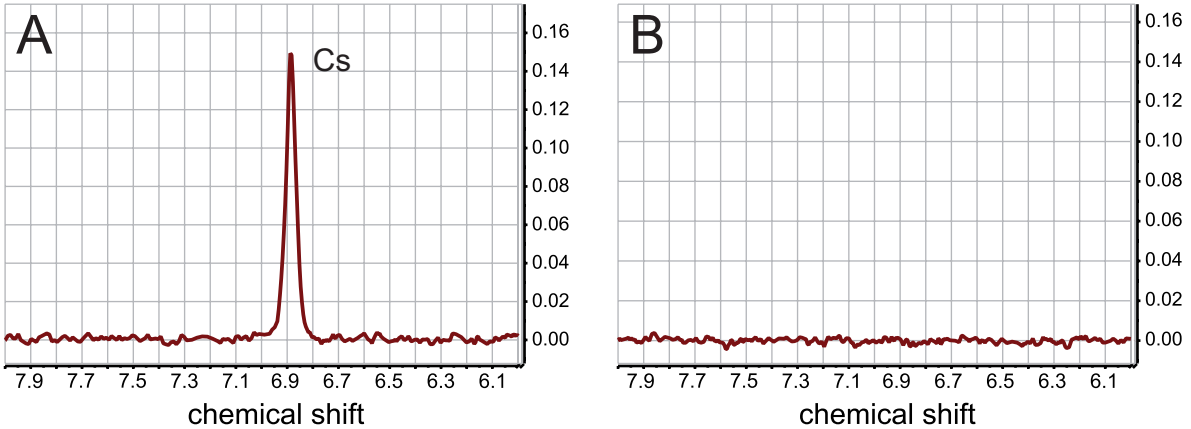

Figure 26: Spectrum of the dissolved bicarbonate sample, acquired with a tunable probe adjusted to the ^{133}Cesium resonance. Figure (A) clearly depicts the cesium resonance signal, which disappears after the successful ion exchange of the cesium (B).

The polarization level (22%) and T_1 (37s) were not affected negatively by the cesium-sodium exchange.

3.2.3.2 *OXO*

For OXO radical clearance, an anion-exchange column (DOWEX 1X8, Dow Chemical Company, Midland, US) with a mesh size of 200-400 was used. To decrease the affinity to the also negatively charged Cs-bicarbonate, the resin was treated overnight with 1 M Na_2SO_4 to convert it to the chloride form and increase the affinity for the negatively charged OXO. After dissolution, the liquid was passed through the resin manually, T_1 and the polarization level were measured, and the concentration of the bicarbonate was estimated.

OXO itself has a dark green color and even low concentrations of the radical in a solution exhibit an intense green color. Hence, the color of the liquid indicates the radical concentrations of the corresponding solutions. After filtration with the exchange column, the liquid changed from green to completely colorless. Furthermore, T_1 increased from 34 s to 40 s and the polarization level was measured as 22.4%, so it can be concluded that all the radicals were successfully removed. Filtration shows no negative effect on the polarization level and T_1. Despite the Na_2SO_4 treatment, the bicarbonate concentration dropped from 15 mmol/L to 0.06 mM after filtration; consequently, the affinity of the resin is still too high for the bicarbonate and the resin is therefore not applicable for OXO filtration with subsequent acquisition of the bicarbonate.

For all experiments, the minimum amount of resin needed was calculated for each corresponding ion (Cs^+ and OXO^-).

3.2.3.3 *Calculating the capacity with Cs^+ ions*

Since every bicarbonate ion is bound to an Cs^+ ion, the Cs^+ concentration equals the bicarbonate concentration in the prepared batch:

$$n_{diss}(Cs^+) = c_0(Cs^+) \cdot V_{batch} = 6\ \frac{mol}{L} \cdot 300\ \mu l = 1.8 \cdot 10^{-3}\ mol$$

where $c_0(Cs^+)$ is the cesium concentration of the prepared bicarbonate and V_{batch} is the maximum volume of dissolved bicarbonate sample in the DNP Hypersense polarizer. With the molecular weight of the corresponding ion being $(Cs^+) = 132.91\ \frac{g}{mol}$, the mass of the ions in a dissolution can be calculated:

$$m_{diss}(Cs^+) = MW(Cs^+) \cdot n_{diss}(Cs^+) = 239 \cdot 10^{-3}\ g\ .$$

In order to include the charge of the ion to the capacity calculation, this physical property must be taken into account using equivalent values (eq) with:

$$eq(Cs^+) = \frac{m_{diss}(Cs^+) \cdot z(Cs^+)}{MW(Cs^+)} = 1.8 \cdot 10^{-3}\ eq\ ,$$

The Cs ion is singly positively charged ($z(Cs^+) = 1, eq(Cs^+) = n_{diss}(Cs^+)$), hence the minimum resin volume for a complete exchange can now be calculated by

$$V_{Resin}(Cs^+) = \frac{eq(Cs^+)}{c_{resin}} = \frac{1.8 \cdot 10^{-3}\ eq}{1.7\ \cdot 10^{-3}\ \frac{eq}{ml}} = 1.059\ ml,$$

with relation to the corresponding wet capacity c_{resin} of the cation-exchange resin (DOWEX W50X8, 200-400 mesh, hydrogen form).

For OXO filtration, similar calculations can be performed using the standard concentration of the OXO63 radical $c_0(OXO^-) = 25\ \frac{mmol}{L}$:

$$eq(OXO^-) = 0.75 \cdot 10^{-3}\ eq$$

$$V_{Resin}(OXO^-) = \frac{eq(OXO^-)}{c_{resin}} = \frac{0.75 \cdot 10^{-3}\ eq}{1.2\ \cdot 10^{-3}\ \frac{eq}{ml}} = 0.625\ ml$$

with respect to the corresponding wet capacity c_{resin} of the anion-exchange resin (DOWEX 1X8, 200-400 mesh, chloride form). The hyperpolarized dissolution liquid was filtered using a column connected to a syringe, which was utilized for collecting the sample and transporting it to the scanning setup, since no automated injection system was used in the experiments. Because of the filtering, the liquid uptake needed 1-2 s longer to complete the collection, so no large amounts of time were lost during filtering.

For the case where an automated injection system is used, it is advisable to directly connect both types of resins successively in line in the dissolution pathway of the polarizer. The pressure of the helium driving gas is ~4 bar and can be used to pass the liquid through the columns, which will further save time. However, attention must be paid because the filtering columns create back-pressure to the system, whose effects must be evaluated.

The resulting filtrations showed encouraging results concerning the exchange of the cesium ion. In principle, radical filtration was successful but further work needs to be performed on finding an optimal resin (e.g., C18) for OXO63 radical filtration.

3.3. Region of interest determination by SNR

For spatial pH analysis, it is important to determine the region of interest (ROI). Many MR imaging techniques rely on ROI estimation, performed by anatomical images. The desired structure is separated either by simply drawing the ROI contour manually in the proton map or automatically, by using algorithms that distinguish the target regions. In this work, an SNR based approach was used for *in vitro* and *in vivo* acquisition.

All ^{13}C acquisition techniques are generally limited by SNR. Based on this, pH mapping is only reliable in regions where the signals of bicarbonate and CO_2 have sufficient intensity. To estimate the SNR of a given acquisition, it is necessary to discriminate the signal from the noise in an image.

The applied setup was a volume coil with a bore diameter of 8 cm. The measured objects were usually distributed around the center of the coil in all spatial directions. The investigated object was placed in the center, leading to the maximum signal from the hyperpolarized bicarbonate. The noise level calculation was performed by using a script that reads the first two lines of pixels in the 64 · 64 matrix in each direction (see Figure 27). The noise estimation is then based on a sum of 152 pixels, which provides a sufficient number of measurement points for averaging. Owing to the experimental setup, no real hyperpolarized substance could be acquired at this location. Hence, all acquired signals were noise.

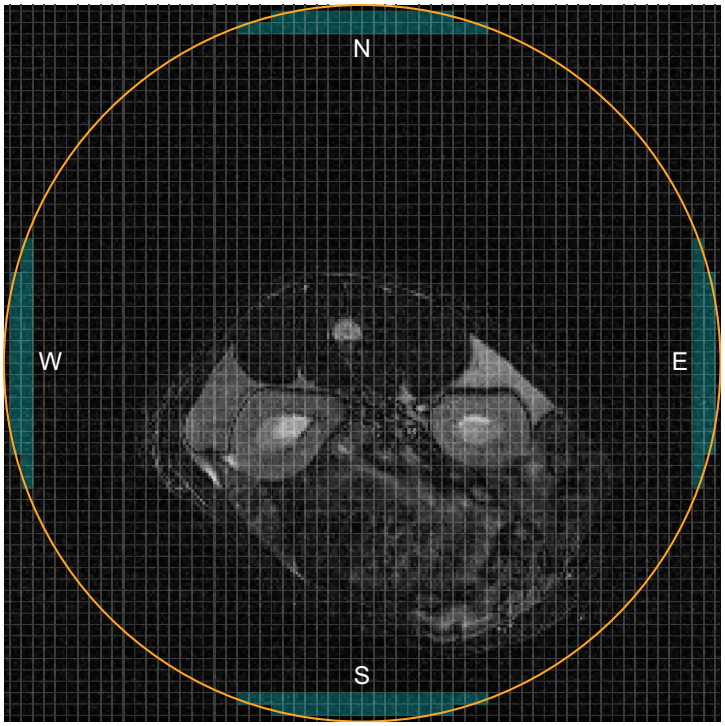

Figure 27: Axial rat kidney slice of 3 mm thickness proton map (gray color scale) acquired with fast recovery fast spin echo (FRFSE), field of view (FOV)= 8 cm · 8 cm, ^{13}C acquisition matrix overlaid on the proton map with a resolution of 64 · 64. The orange circle depicts a cross section in the z-axis through the volume coil. The pixels used for noise calculation are depicted in light blue and named by the origin of their appearance: north (N), east (E), south (S), west (W).

The regions are described according to their origin, as north (N), south (S), east (E), and west (W). The average noise in each region were calculated and led to a general noise level of the acquired image.
However, blurring can occur when reconstructing using a shifted resonance frequency (see Figure 28). This false signal information can drift into the abovementioned regions of noise estimation, falsifying the noise estimation results. Thus, achieving the correct reconstruction frequency is important for the correct reconstruction of the hyperpolarized signal. This leads to a possible inherent error for the case that the excitation band of the SPSP pulse is off-resonant.

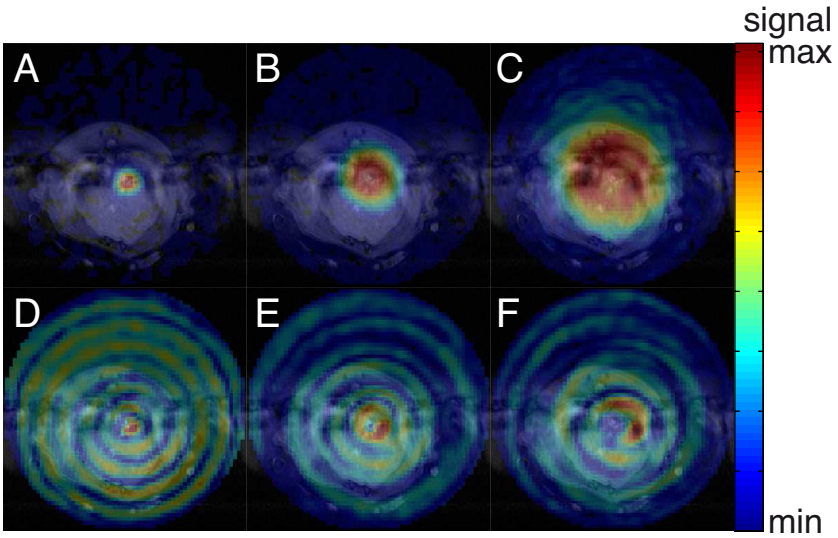

Figure 28: Gradient echo proton map of an axial liver slice from a healthy Lewis rat (gray color scale). Slice thickness = 10 mm, FOV=8 cm · 8 cm, flip angle (FA)=10°. ^{13}C-bicarbonate image overlaid (jet color scale), measured directly after injection. Reconstruction of the hyperpolarized signal for different chemical shift frequencies (A=0 Hz, B=50 Hz, C=100 Hz, D=250 Hz, E=500 Hz, F=1138 Hz). The excitation at the bicarbonate resonance frequency leads to the correct reconstruction of the map at 0 Hz. At this time point, the largest bicarbonate signal can be seen in the *vena cava*. Departure from this optimal reconstruction frequency leads to a decrease of the SNR and blurring of the hyperpolarized signal. Figure F shows the case of the chemical shift at 1138 Hz and 3 T (≈35 ppm), reflecting the case for the bicarbonate and CO_2 chemical shift.

Blurring leads to a higher mean noise level and thus a decreased calculated SNR. To overcome this issue, the mean values of each cardinal direction were compared and separated by a threshold value, which ensured that regions with a spiked mean value, including artifact signals, were excluded from noise level calculation.
The main contributor to the decreasing SNR at low flip-angle excitation is the short *in vivo* T_1, which is ≈ 10 s for bicarbonate at 3 T, which limits the signal acquisition to a short time window (see Figure 29). Defining the SNR in the image allows separating the hyperpolarized signal from the noise with signal intensity thresholds.

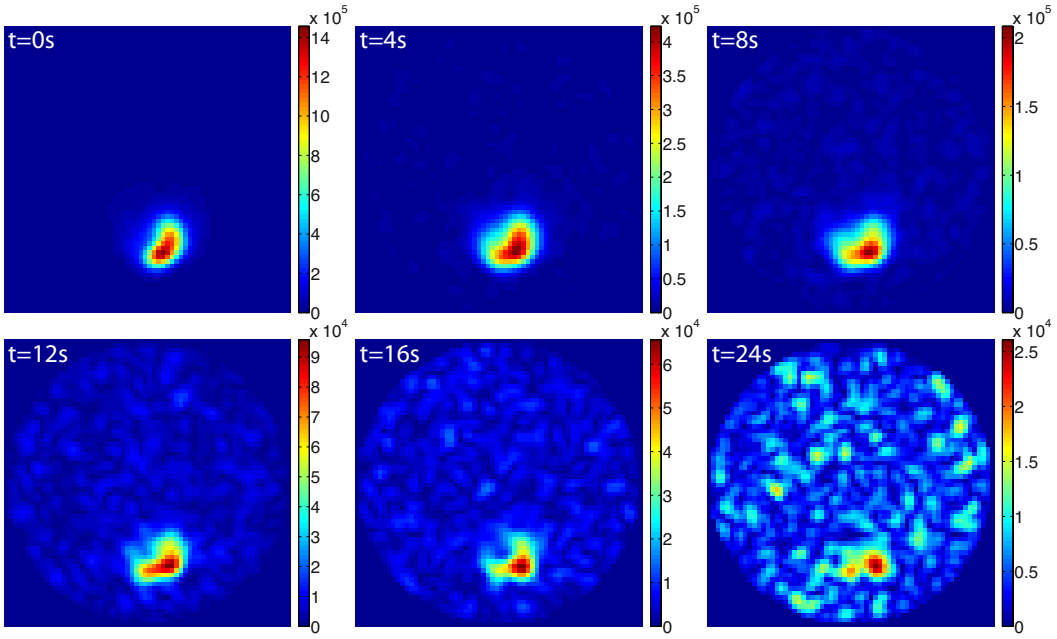

Figure 29: Hyperpolarized signal decay of bicarbonate from an axial rat heart slice, measured with on resonant excitation with the SPSP pulse at the bicarbonate resonance frequency. Image acquired directly after the end of injection and with repetition time (TR)=2 s. Slice thickness= 10 mm, FOV=8 cm, Resolution=64 · 64, FA=10°. Signal is decaying with T_1=10 s *in vivo*, leading to a limited time window for hyperpolarized signal acquisition.

4. Results and discussion

After optimizing the preparation and dissolution procedure, the bicarbonate was investigated spectrally and applied *in vitro* for signal analysis (chapter 4.1). This included error propagation analysis for the pH acquisition at different SNRs. Subsequently, the imaging modalities were SNR-optimized and analyzed in terms of pH-imaging sensitivity for different pH values (chapter 4.2). The optimized methods were then applied to map healthy rats for hyperpolarized *in vivo* signal performance and obtain signal maps of different organs (chapter 4.3). Finally, pH maps were acquired of rats with metabolic alkalosis and induced sterile inflammation (chapter 4.4).

4.1. pH quantification spectral *in vitro*:

The spectral investigation and *in vitro* application of the bicarbonate for signal analysis allowed the evaluation of the signal performance for bicarbonate and CO_2 under different pH conditions for different counter ions (chapter 4.1.1) and with a cancer cell spheroid solution (chapter 4.1.2). The errors originating from the CO_2 release (chapter 4.1.3) and the different SNRs (chapter 4.1.4) were quantified, leading to a broad sensitivity analysis concerning the method's major challenges, which had not been previously performed for bicarbonate pH mapping.

4.1.1 Results on buffers with Na-bicarbonate

To estimate the viability of pH detection with hyperpolarized bicarbonate, spectral analysis of hyperpolarized ^{13}C-Na-bicarbonate was performed. The spectral results also served as a comparison with the subsequent used ^{13}C-Cs-bicarbonate to reveal possible variations between the two substances. Na-bicarbonate showed a limited maximum concentration of 1.2 mol/L and the quantification experiments were limited to *in vitro* experiments with PBS buffers. The spectral analysis was performed to determine the resulting behavior of the used chemical preparation procedure of the hyperpolarized bicarbonate, including the influence of the glassing and dissolution agents and the dissolution process. SNR- and time-stability-analysis were performed, to examine the influence of high field (3 T) at various flip angles. The results provided a first view on the feasibility of ^{13}C pH measurements and revealed possible drawbacks. To characterize the factors influencing the pH measurement, analysis was performed with pure buffer solution, without the addition of carbonic anhydrases.

4.1.1.1 *Spectral and temporal signal evaluation*

The spectral analysis of the hyperpolarized spectrum revealed a clear bicarbonate and CO_2 signal with no visible side products (see Figure 30). This leads to the conclusion that during the preparation process, hyperpolarization, and dissolution of the bicarbonate sample, no unwanted side products or reactions were obtained. Only one side peak was observed,

showing a CSD of 1 ppm to the bicarbonate. The impurity clearly shows hyperpolarized behavior with the same T_1 as the bicarbonate. This side peak has been reported before in hyperpolarized bicarbonate experiments. However, after the exclusion of all reaction species of bicarbonate and CO_2, like H_2CO_3 and CO_3^{2-}, the impurity could not be identified, so it was subsequently integrated in the bicarbonate signal. The bicarbonate and CO_2 signals showed no changing CSDs for different pH. The comparison of Na-bicarbonate and Cs-bicarbonate revealed no differences in spectral and temporal behavior.

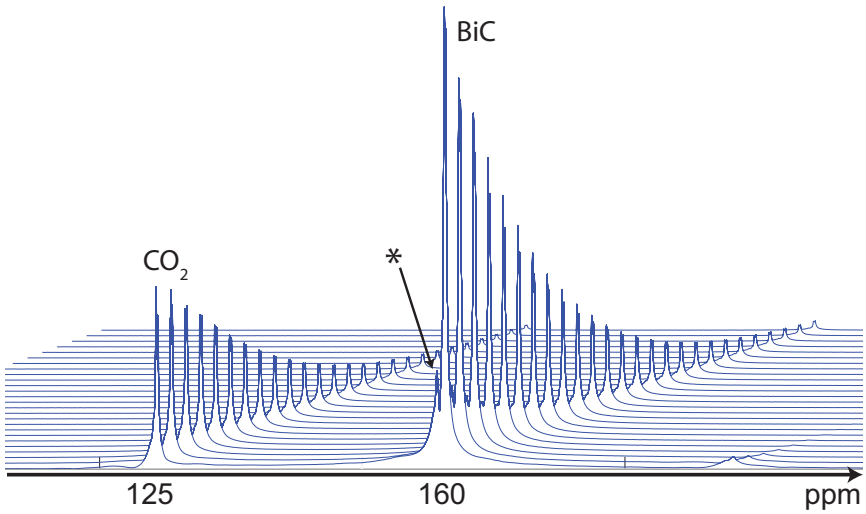

Figure 30: Example of the temporal decay of the hyperpolarized spectrum of bicarbonate (160 ppm), CO_2 (125 ppm) and the impurity (marked with * at 159 ppm); hard pulse excitation with a 10° flip-angle excitation, TR= 1 s. The z-axis shows longitudinal measurement acquisitions with Δt= 5 s Acquisition was performed in a D_2O-based PBS buffer with a set pH of 6.

The measurements of the signal intensities and of the bicarbonate and CO_2 resulted in typical decay curves for hyperpolarized substances (see Figure 30). The pH measurements were limited by the SNR, which was again limited by the T_1 decay of each hyperpolarized compound. For D_2O-based PBS buffers, measuring the integral of the bicarbonate and CO_2 lead to a pH-dependent ratio. The time dependency of this ratio is depicted in Figure 31. Signal development evaluation was performed without the addition of carbonic anhydrases to create a “worst-case scenario” with a maximum CO_2 buildup time. *In vivo*, CO_2 is generated nearly instantaneously [53], thus the time window can be expanded to earlier time points.

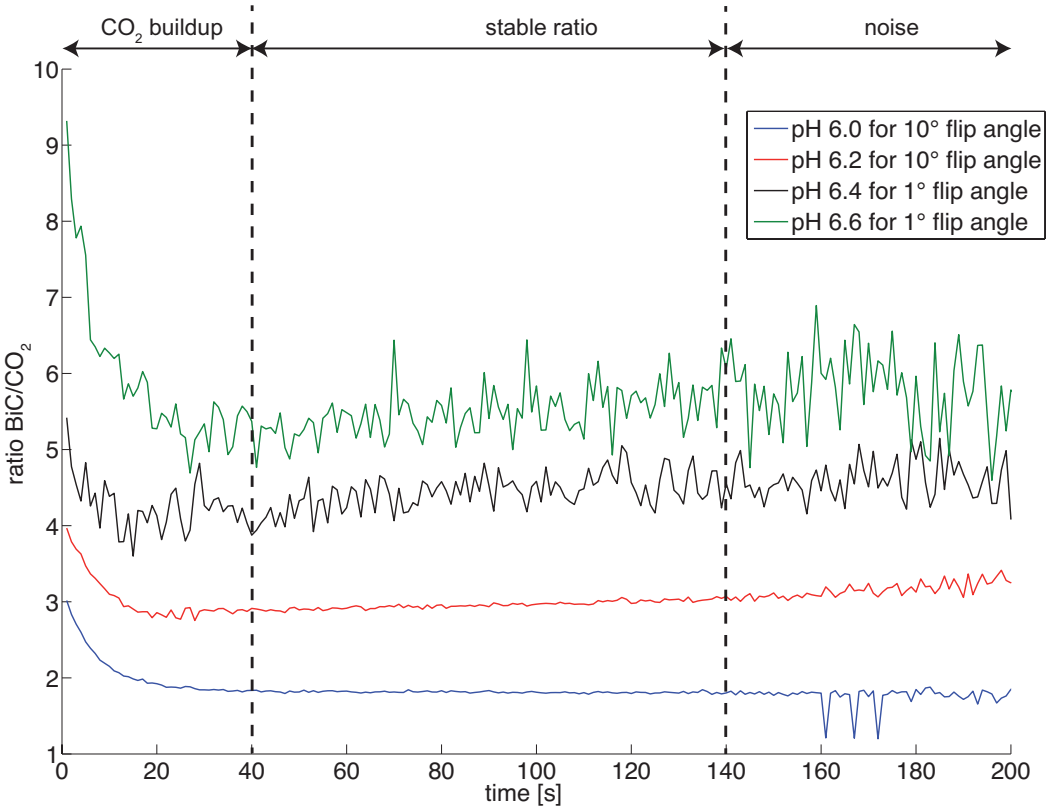

Figure 31: Temporal signal development of bicarbonate to CO_2 ratio. The horizontal axis shows the elapsed time and the vertical axis shows the ratio of the signal integrals of bicarbonate to CO_2. The signals were acquired with hard pulse excitation in 1 ml D_2O-based PBS buffers directly after the addition of the hyperpolarized bicarbonate. The buffers were set to different pH values and measured for two different excitation flip angles of 10° and 1°. The slight drift of the signal, observed for pH 6.2, 6.4, and 6.6 could be explained by CO_2 release and subsequent pH increase during the experiment. Figure from [129].

Due to the lack of carbonic anhydrase activity, ratio equilibrium was not established instantaneously, but according to the chemical reaction constant. The buildup time is pH dependent: lower pH values and higher corresponding CO_2 concentrations required longer times for the establishment of equilibrium. In the biologically relevant pH region of 6-8, equilibrium is established at 40 s at the latest. According to [53] rate constant from bicarbonate to CO_2 without enzymes is ~0.1 s^{-1}. Assuming an accelerated rate constant under presence of carbonic anhydrases, e.g. CA IX with ~10^6 s^{-1}, (see chapter 2.2.4) the buildup time for a stable equilibrium would be reduced to 40 µs and is thus not detectable with hyperpolarized NMR. A stable ratio is maintained until the signal decay leads to a decrease of the SNR. After 140 s, the noise drops below the SNR threshold, resulting in a time frame of 100 s of stable pH measurements between the CO_2 buildup and the signal decay threshold. The results for different flip angles confirm the feasibility of the method even at very low excitation and high noise, which is shown by the simulations for pH 6.4 and 6.6 with 1° flip-angle excitation. The noise level increase is mainly based on the reduced excitation but also on the reduced CO_2 levels at lower pH values.

4.1.1.2 *Spectral analysis*

The accuracy estimation of the spectral pH measurements with hyperpolarized Na-bicarbonate was performed with a H_2O-based PBS buffer set to pH values of 6.0 to 6.4 with small pH steps ΔpH of 0.2 (see Figure 32). This pH resolution must be at least achieved to establish further pH measurements in *in vivo* systems.

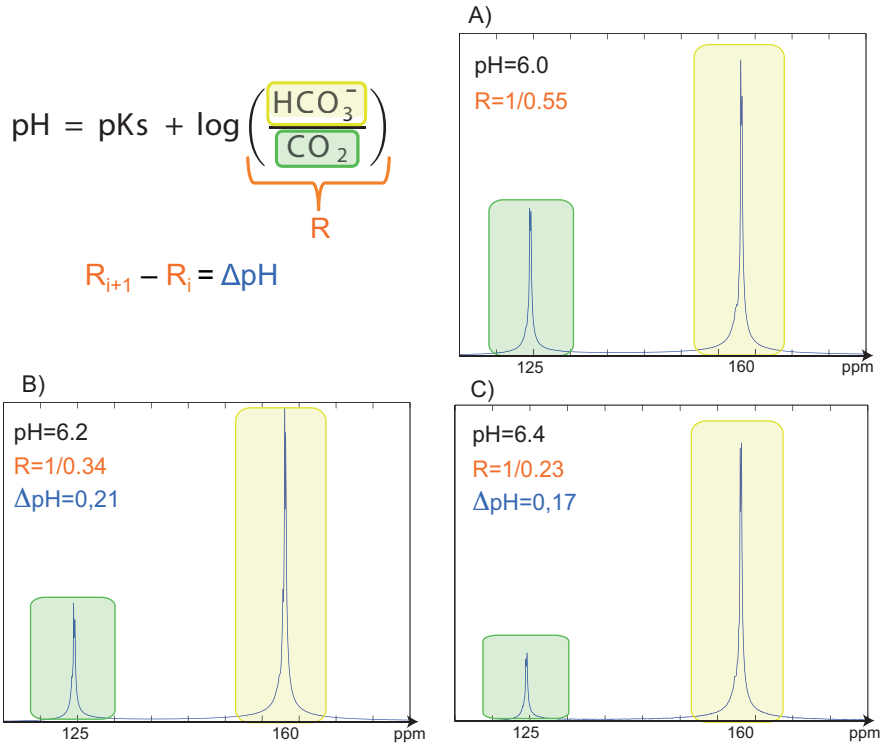

Figure 32: Spectra of bicarbonate (yellow-marked) and CO_2 (green-marked). A 60 µl hyperpolarized bicarbonate sample, dissolved in 5 ml H_2O-based PBS buffer was measured in 1 ml 0.2 M Sørensen phosphate buffer. The buffers were set to different pH values with a common glass electrode. The spectra were acquired with a 10° hard pulse and subsequent FID readout 25 s after mixing, in order to measure in the time region of stable bicarbonate to CO_2 ratio. The ratio of bicarbonate to CO_2 is given by the orange numbers and leads to the calculation of the pH difference in the next buffer.

To avoid errors from the assumed pKs value in the calculation of the absolute pH value, differences were calculated, which are independent from pKs. The results demonstrate that pH value differences can be estimated with very good accuracy in a spectral manner. The measured pH values were biased by errors, changing with SNR. This error calculation can be reviewed in chapter 4.1.4.

4.1.2 MCF-7 cell suspension analysis

The signal decay of hyperpolarized substances undergoes influences from multiple sources. The T_1 relaxation is inherently influenced by the field strength and also environmental parameters, such as the viscosity of the sample, and the buffer concentration of the dissolution agent shows an impact on the hyperpolarized signal decay. It is important to determine and characterize these influences, e.g., for the transfer to another MRI system when higher gradient strengths than those achievable by a clinical scanner are needed.

The estimation of intra- and extracellular bicarbonate and CO_2 signal contribution constitutes an important knowledge gap in current pH mapping ^{13}C-bicarbonate research, where the measured signal is assumed to occur mainly extracellularly [53,130]. However, in *in vivo* conditions, multiple cellular bicarbonate transporters exist, allowing an exchange of intra- and extracellular bicarbonate (see Figure 33).

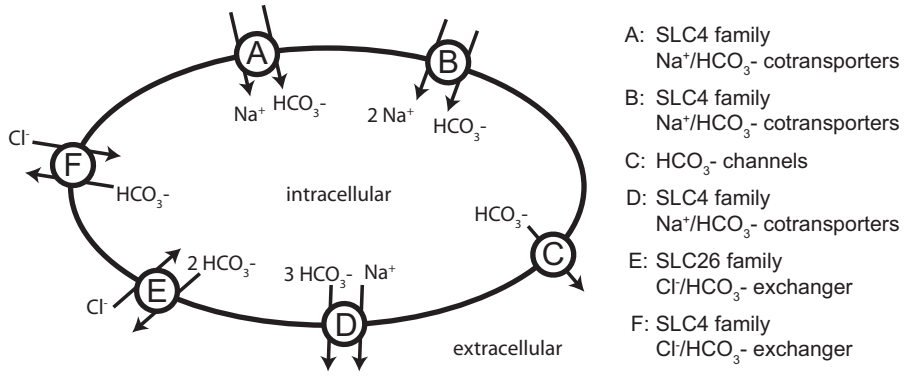

Figure 33: Schematic overview of cellular bicarbonate transporters.

A compartment determination would help to show the impact of intracellular signals to pH maps. Intracellular signals can be separated by their respective apparent diffusion coefficients (ADCs), which differ for intra- and extracellular space [131,132]. Before the technique of gradient-based compartmental ADC analysis can be applied to ^{13}C-bicarbonate, it is necessary to ensure that the SNR and T_1 are sufficient for a cell environment and different field strengths and that the influential parameters have been quantified. Considering the tumor spheroid experiments, it was necessary to demonstrate that the investigated spheroids survived and healthy cells remained; this was tested with lactate dehydrogenase (LDH) analysis. A dissolved ^{13}C-bicarbonate sample was then added to an *in vitro* solution of MCF-7 spheroid cells to investigate influences of the different environments (highly concentrated MCF-7 cell spheroid solution, culture medium, and pure dissolution buffer) to SNR and T_1 for field strengths of 1 T, 3 T, and 14 T. Additionally, different pH levels were tested and controlled by electrode pH measurements.

All T_1 measurements were performed with 10° flip-angle excitation and subsequent FID readout. The pH values were controlled by a common glass electrode.

	exp 1	exp 2	exp 3	exp 4	exp 5	exp 6	exp 7
pH DA	7.11	7.11	7.11	7.32	6.26	5.17	5.13
c DA [mmol/L]	40	40	40	40	40	40	120

	T_1 [s]													
	T_1	± err	T_1	± err	T_1	± err	T_1	± err	T_1	± err	T_1	± err	T_1	± err
1 T BiC decay	83.27	1.01	93.41	1.40	91.85	0.93	93.98	1.54	85.68	1.63	79.69	0.93	76.05	1.37
3 T BiC decay	54.08	0.23	53.97	0.09	56.92	0.16	60.24	0.22	61.92	0.12	56.31	0.09	42.53	0.09
CO_2 decay	55.16	0.81	55.16	0.81	53.88	1.33	53.34	0.64	58.24	0.44	54.56	0.41	41.79	0.19
CO_2 buildup	9.39	0.76	10.46	1.07	12.31	1.83	9.88	0.63	8.65	0.92	9.29	0.76		
14 T BiC decay	43.16	0.63	42.01	0.65	43.65	0.63	37.25	0.21	37.62	0.22	38.15	0.28	38.01	0.58
CO_2 decay	41.24	5.78	57.30	6.09	57.17	7.99	40.63	4.59	49.65	3.35	52.61	4.26	25.01	2.95

Table 8: T_1 values and errors for ^{13}C-bicarbonate and $^{13}CO_2$ in culture medium (orange), cell solution (green), and pure dissolution (blue) for 1 T, 3 T, and 14 T. pH DA reflects the pH of the dissolution agent (buffer), c DA reflects the concentration of the buffer. The yellow boxes show the pH and the concentration of the phosphate buffer used to dissolve the hyperpolarized ^{13}C-bicarbonate. The T_1 of ^{13}C-bicarbonate and $^{13}CO_2$ decreases with increasing field strength. Furthermore, decreasing the pH and increasing the buffer concentration leads to a decrease in T_1. All decays show a mono-exponential behavior, except for the 3 T CO_2 signal, where the experimental setup allowed more rapid tracking of the CO_2 buildup. Bi-exponential fitting allowed the extraction of a CO_2 buildup constant, which was similar for all experiments performed.

When measuring at 1 T, the T_1 of ^{13}C-bicarbonate, dissolved in D_2O-based phosphate buffer dissolution, shows a clear dependency on pH. Decreasing the pH leads to a decrease in T_1. Additionally, increased buffer concentrations decrease T_1. At 3 T, the T_1 of ^{13}C-bicarbonate and $^{13}CO_2$ were measured with and without added MCF-7 cell spheroids. $^{13}CO_2$ showed similar T_1 compared with ^{13}C-bicarbonate for the measurements with added MCF-7 cell spheroids. The T_1 of ^{13}C-bicarbonate only increased in the culture medium; it decreased when cells were added to the solution. This T_1 decrease is not detectable for $^{13}CO_2$, where T_1 does not change significantly following cell-spheroid addition. This behavior may be due to the increased viscosity from the 50 million cells. Due to the bicarbonate's larger size, changes in viscosity increase its correlation time τ_c and chemical shift anisotropy (CSA) more than in CO_2. Movement of the bicarbonate changes the area of the planar projection of the bicarbonate. These changes hold true for rotations in all three spatial dimensions. Because of its linear shape, CO_2 has one axis of rotation, where no changes occur during the movement. Hence, for this degree of motion, CO_2 is not affected by environmental viscosity changes and

T_1 is therefore less susceptible to changes of environmental viscosity. At the higher field strength of 14 T, bicarbonate T_1 is again reduced under the addition of MCF-7 cell spheroids. In addition to the LDH measurements, cell viability is reflected in the pH decrease of the cell suspension, compared to the culture medium for the 14 T scanner measurements (Table 9). A pH decrease of the medium is an indication of cell metabolism and cell viability. During this time, the highly concentrated cell solution acidifies its environment, owing to normal cell respiration.

	exp 4	exp 5	exp 6	exp 7
	electrode pH			
Pure Dissolution	8.2	7.18	6.96	6.49
Culture Medium	8.24	7.72	7.63	7.07
Cell Suspension	7.86	7.23	7.26	6.85

Table 9: pH control measurements with glass electrode after MR acquisition. The pH values were measured for the pure dissolution experiments, the experiments with the culture medium and cell suspension. The pH of dissolution is influenced by the pH of the dissolution agent (PBS buffer) and the dissolved bicarbonate. The culture medium with and without cells is weakly buffered to a pH of 7.4 to provide best cell growing conditions. Comparing the culture medium pH with the pH of the cell suspension, acidification was observed 5 minutes after MR acquisition.

The minimal pH and maximal buffer-concentration measurements (far right column, Table 8) show a significant drop in T_1 for both the bicarbonate and CO_2.
In summary, from the physical point of view, these results show a clear influence of field strength on the bicarbonate T_1 as well as the sample's viscosity. From the chemical point of view, increasing pH and buffer capacity leads to a decreased T_1.

4.1.3 CO_2 loss issue

Long-term measurements of dissolved bicarbonate and CO_2 show an inherent problem in the stability of the measured signal due to loss of CO_2 from the solution during the measurement as depicted in Figure 34. Whereas the bicarbonate concentration is consistently high at physiological pH values, CO_2 undergoes a dynamic change of concentration due to buildup from bicarbonate (see chapter 4.1.1) and loss of the dissolved CO_2 into the gaseous phase. For the case of single-shot pH imaging with hyperpolarized bicarbonate *in vivo*, loss due to CO_2 can be neglected, as long as one does not intend to perform a longitudinal measurement. Because the hyperpolarized signal decays relatively fast (T_1 *in vivo* = 10 s), the loss of CO_2 only has a minor influence on the resulting pH. However, it must be considered as a source of error and for the following cases:
a) Long-term thermal measurement with multiple repetitions and measurement times.
b) Long-term hyperpolarized measurements in buffers with long T_1 (e.g., D_2O with a T_1 of 120 s at 1 T).

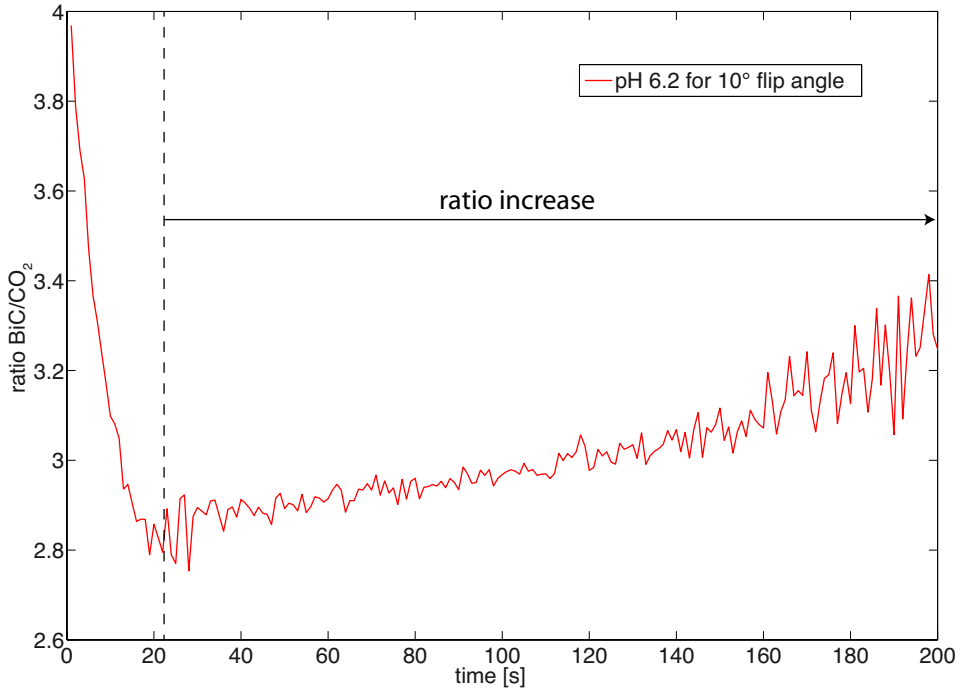

Figure 34: Longitudinal measurement of the signal ratio of hyperpolarized bicarbonate to CO_2. Hyperpolarized bicarbonate was added to 1 ml PBS (c=0.1 M) phantoms set to a pH of 6.2. The signals were acquired with hard pulse excitation for a flip angle of 10°. The acquisition started directly after mixing. The horizontal axis depicts the measurement time and the vertical axis depicts the ratio of bicarbonate to CO_2. The CO_2 buildup is finished after 21 s, since no carbonic anhydrases were added. The bicarbonate to CO_2 ratio changes when CO_2 starts to leave the sample volume, changing the ratio and subsequently measured pH.

Standard T_1 and polarization level measurements were performed using a low-field (1 T) Bruker Minispec mq40 NMR analyzer (Bruker Optik, Ettlingen, Germany) with a four-fold 20° flip-angle excitation for hyperpolarized signal estimation, directly after dissolution. Subsequently, T_1 was estimated by 20-fold 10° flip-angle excitation with a repetition time (TR) of 1 s and the thermal signal was measured by Carr–Purcell–Meiboom–Gill (CPMG) pulse trains (12 times), from which the polarization level was derived. These thermal measurements lasted up to 90 minutes, depending on the number of repetitions, and were therefore sensitive to CO_2-loss errors.

Once CO_2 starts moving into the gaseous phase above the liquid, the partial pressure of the CO_2 rises, until equilibrium is established between the dissolved CO_2 and the CO_2 above the sample surface. T_1 measurements were performed using standard 10 mm NMR tubes with a liquid sample volume of 1 ml. Gastight sealing of the NMR tubes does not solve the problem of losing signal owing to CO_2 release, as demonstrated by the following calculations, made under the assumption that equilibrium between dissolved CO_2 and CO_2 in the gas phase is established instantaneously.

The calculation of the amount of CO_2 dissolved in 1 ml dissolution (c_{CO2}) was made as follows. The volume of the sample batch is $V_s = 100\ \mu l$, containing 80%/20% mass of glycerol/D_2O. The molar mass of Cs-bicarbonate is $M_{Cs\_BiC} = 193.922\ g/mol$ and the dissolved amount of bicarbonate: $m_{BiC} = 100\ mg$. The volume of the dissolution agent is $V_{DA} = 5\ ml$ and the volume measured in Minispec: $V_{MS} = 1\ ml$. Using these values gives the

amount of bicarbonate in the MiniSpec: $m_{BiC\_MS} = 77.35\ \mu mol$. Since the CO_2 is produced from the bicarbonate and is pH-dependent, a neutral pH of 7 is assumed, leading to a ratio of $\frac{BiC}{CO2} = \frac{7.41}{1} = \frac{68.2\ \mu mol}{9.2\ \mu mol}$, resulting in a CO_2 concentration of $c_{CO2} = 9.2\ mmol/L$ in the batch.

Calculating the partial pressure of CO_2 (p_{CO2}), using the Henry constant of CO_2 at 25 °C:

$$k_H = 29.76\ \frac{atm\ L}{mol} = \frac{p_{CO2}}{c_{CO2}} \quad (106)$$

$$\Rightarrow p_{CO2\_liquid} = k_H \cdot c_{CO2} = 0.274\ atm\,. \quad (107)$$

Using the partial pressure of CO_2 in air: $p_{CO2\_air} = 0.00039\ atm$ leads to a partial pressure difference of $\Delta p = p_{CO2\_liquid} - p_{co2\_air} = 0.27361\ atm$ between the liquid phase and the volume above the liquid.

For thermal polarization level measurements at 1 T the MiniSpec spectrometer, the used NMR tubes had the following parameters (see Figure 35): $d = 8.5\ mm, h = h_D + h_S = 18\ cm$ with h_D being the height of the dead volume and h_S the height of the sample volume. Using $V_{MS} = 1\ ml$, the total volume, reclaimable in a closed NMR tube, is: $V_{total} = 9.21\ cm^3$. In equilibrium, the partial pressure of the gas phase and the liquid phase are equal:

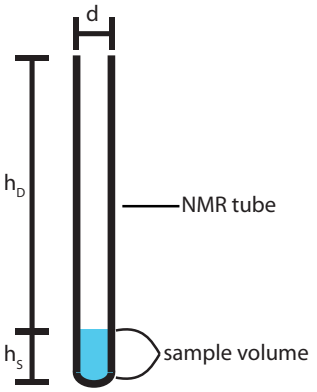

Figure 35: Standard NMR tube for T_1 measurements with diameter d, height of the sample volume h_S, and height of the dead volume h_D.

$$p_{CO2\_liquid} = k_H \cdot c_{CO2} = \frac{n_{CO2} \cdot R \cdot T}{V_{total}}\,. \quad (108)$$

Using $c_{CO2} = \frac{n_{0CO2} - n_{CO2}}{V_{sample}}, R = 8.314\ \frac{J}{mol\,K}, T = 298.15\,K$, the amount of evaporated CO_2 becomes:

$$n_{evap} = \frac{n_{0_{CO2}}}{\left[\frac{R \cdot T \cdot V_{sample}}{k_H \cdot V_{total}} + 1\right]} = 8.44\ \mu mol\,. \quad (109)$$

This results in an evaporation of 92% of the total amount of CO_2, starting from $n_{0_{CO2}}$. For these calculations, pH is assumed to stay constant, which only holds true for well-buffered systems, as CO_2 evaporates and is rebuilt from the bicarbonate pool. Although one can argue that the pool size of the bicarbonate is more than 7 times bigger compared with the CO_2 pool size and would be able to antagonize the loss up to a certain amount, it would be preferable to avoid the aforementioned issue for signal conservation. The loss can either be antagonized by using a higher-concentration sample or by reducing the dead volume above the liquid sample volume. Since hyperpolarized experiments are time-sensitive, standard methods of sealing NMR tubes, like melting the tube, fail. Hyperpolarization studies are normally one-shot experiments, which need to be repeated several times to obtain sufficient statistical significance. This would make one-way experiments even more cost-intensive for some NMR tubes that cost 50€ upwards per piece. A solution for this issue was developed and is shown in Figure 36. The dead volume of the NMR tube is reduced by inserting a plug of an MR-

compatible material (e.g., glass) with a volume V_p. Subsequently, a gastight cap seals the tube. The reduced dead volume $V_{rd} = V_d - V_p$ leads to a reduced loss of CO_2 due to faster partial pressure equilibrium. Since the mounting procedure only takes seconds, it is compatible with hyperpolarized experiments. The plug can be later removed with the corresponding post, which allows cleaning and reusing the NMR tube.

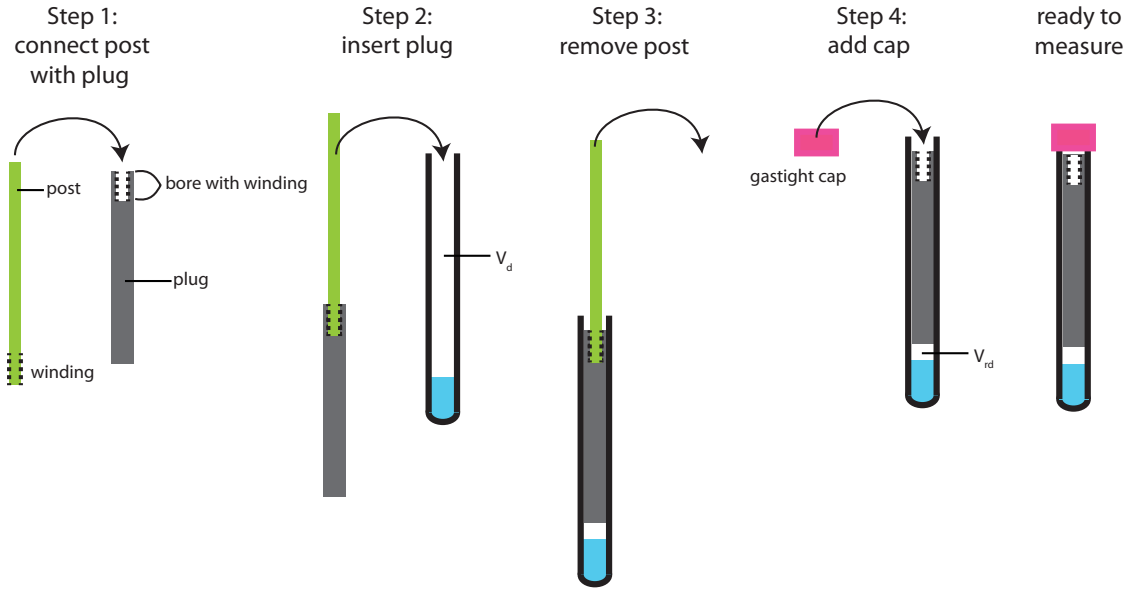

Figure 36: Procedure of preventing CO_2 loss during hyperpolarized MR experiments and for subsequent thermal measurements of the pH. V_d is the dead volume and V_{rd} the reduced dead volume, in which CO_2 can be released.

The problem of losing CO_2 at thermal phantoms also impacts pulse design, as it could make the preparation of thermal phantoms containing bicarbonate and CO_2 problematic. Hence, pulse design was performed using literature values, with an assumed resonance frequency difference between bicarbonate and CO_2 of ~35 ppm.

4.1.4 pH error estimation

Uncertainty analysis is an important tool to estimate the limits and opportunities of a given measurement technique. Here, errors from different sources are taken into account and their influence to the estimated value is quantified. This helps to counteract possible problems in measurement accuracy in advance. After a range of the appropriate measurement accuracy is determined, the investigated targets can be shortlisted and fitted to the measuring technique.
Similarly to all hyperpolarized measurements, the bicarbonate pH measurements are also mainly limited by the SNR. To estimate the influence of the SNR on the measured pH, quantification was performed based on error propagation. pH can be simulated by the signal ratios of the bicarbonate and CO_2, assuming that the integral of the two signals equals 1 (see Figure 37).
pH, as described from the Henderson-Hasselbalch equation, is assumed to be affected from two error sources: error u_{BiC} of the bicarbonate signal and error u_{CO2} of the CO_2 signal. These

affect the calculated pH as described by the equation of error propagation for two independent error sources [133]:

$$u_y = \sqrt{\left(\frac{\partial y}{\partial x1} \cdot u_{x1}\right)^2 + \left(\frac{\partial y}{\partial x2} \cdot u_{x2}\right)^2} \quad (110)$$

which can be rewritten (see Appendix 6.1) as

$$u_{pH} = \sqrt{\left(\frac{1}{ln10 \cdot sig\_BiC} \cdot u_{BiC}\right)^2 + \left(\frac{-1}{ln10 \cdot sig\_CO2} \cdot u_{CO2}\right)^2} \quad (111)$$

where *sig_BiC* is the bicarbonate signal and *sig_CO2* is the CO_2 signal. u_{BiC} and u_{CO2} are the errors, that depend on the SNR of each peak. For CO_2, a large flip-angle excitation leads to larger SNR, which results in a smaller uncertainty u_{CO2}. Hence, the error is smallest for the largest signals, which is the case when the bicarbonate signal and the CO_2 signal are the same (=0.5, when the integral of signal intensities is 1) and the ratio is 1. Changing the ratio to an increased SNR will lead to a decreased error for the one compound. On the other hand, for the other compound, decreasing the signal will lead to a decreased SNR and an increased error. If SNR is enhanced for one compound (e.g. CO_2 in Figure 37, red lines) by increased flip angle excitation decreases error values for alkaline pH. Hence, the signal ratio can be plotted vs. pH, as shown in Figure 37. Using an example *in-vivo* dataset (as shown in Figure 38), the range of acceptable pH is dependent of the SNR of the signals, as depicted in Figure 37. pH of acceptable accuracy (pH error < 0.2) can be simulated with same excitation flip-angle (30°) for BiC and CO_2 for pH 4.79-7.62 and can be extended with a larger excitation flip-angle for CO_2 (90°) to pH 4.79-7.92. pH value with lowest error shifts from pH=6.2 to pH=6.5 (see Figure 39), which reflects the change in signal intensity for CO_2. At this pH, BiC and CO_2 have again the same intensity (=0.5, when the integral of signal intensities is 1).

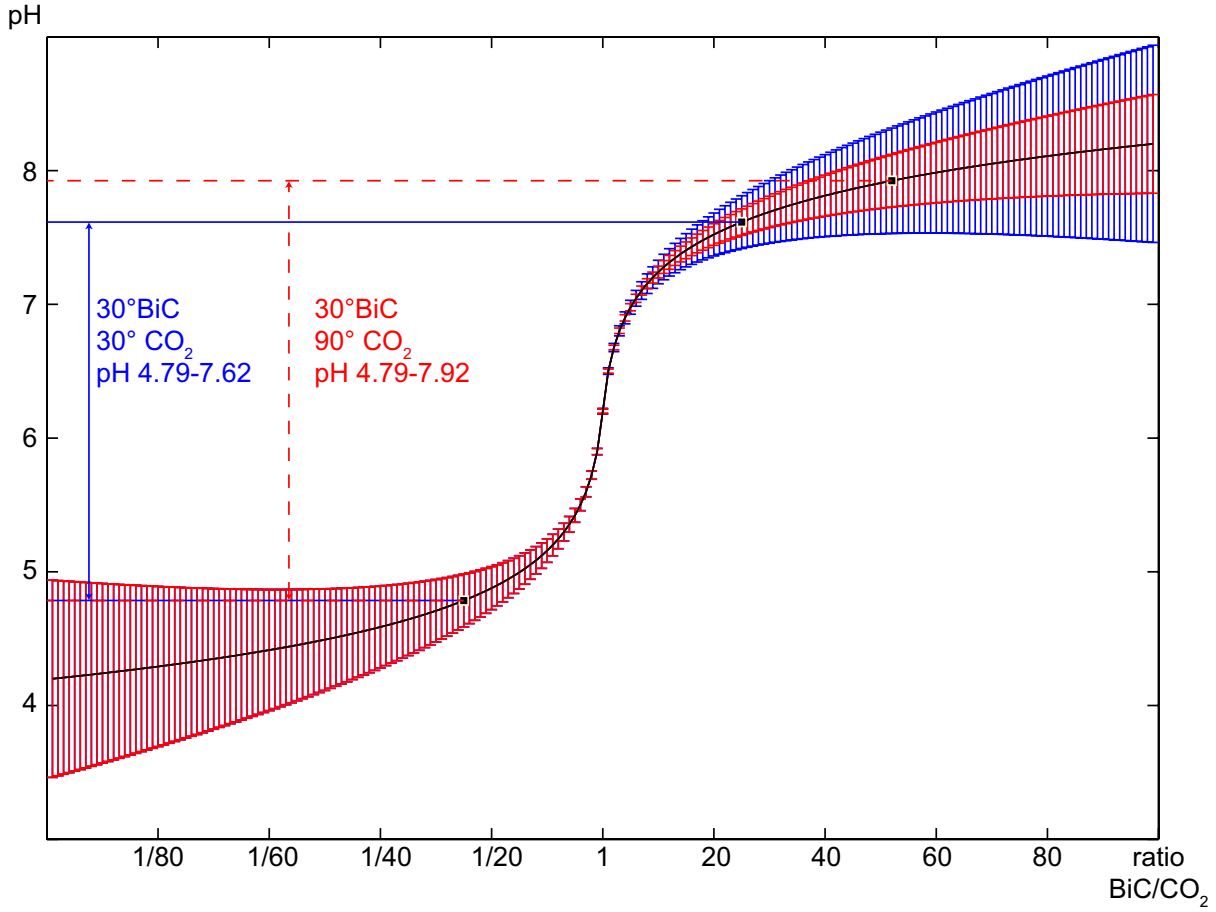

Figure 37: Error estimation of the pH value from a SPSP excited spectrum. The x-axis shows the bicarbonate to CO_2 ratio. The y-axis shows the calculated pH with an assumed pKs of 6.2. The solid black line depicts the pH, simulated by the ratio of the bicarbonate and CO_2 signals. The blue lines show the acceptable pH range when the excitation flip-angles of BiC and CO_2 are assumed to be the same (here 30°, as typically employed for *in vitro* experiments). The region of acceptable pH is within 4.79 to 7.62 and the error propagates symmetrically for lower and higher pH. The region of acceptable pH estimation was set to pH ± 0.2 and is dependent on the flip angles and the assumed pKs. For *in vivo* experiments, the flip angle of CO_2 was set to 90° to excite the maximum number of CO_2 spins in order to overcome low *in vivo* signal intensity. This technique extends the region of acceptable pH to 7.92 (red line). The smallest error and best pH estimation occur at pH = pKs = 6.2 for the same excitation and pH = 6.5 for 90° CO_2 excitation.

The increase in CO_2 excitation flip angle has a higher impact at higher pH owing to the low CO_2 intensities. There is little impact of the excitation flip angle at pH < pKs (the red and blue lines in Figure 37 are overlaid), as the impact of noise in the CO_2 signal is small at low pH. This low noise is observed because the main error source is the small bicarbonate signal. The asymmetry would also appear mirror-inverted if the bicarbonate flip angle was larger than that for CO_2. However, due to the high bicarbonate signal intensities in *in vivo* experiments, this asymmetry is of no further interest.

The relevant range of pH in *in vivo* measurements covers 5.5-8 in biological targets; therefore, the error estimates show that pH can be calculated to a good approximation within the region of acceptable pH. Owing to its extension via flip-angle optimization, the region covers pH values from 4.79 to 7.92. This demonstrates the robustness of the method regarding biological

pH and distinguishes the method from other pH-detecting methods, such as CEST, that may exhibit varying sensitivity for *in vivo* pH ranges [51].

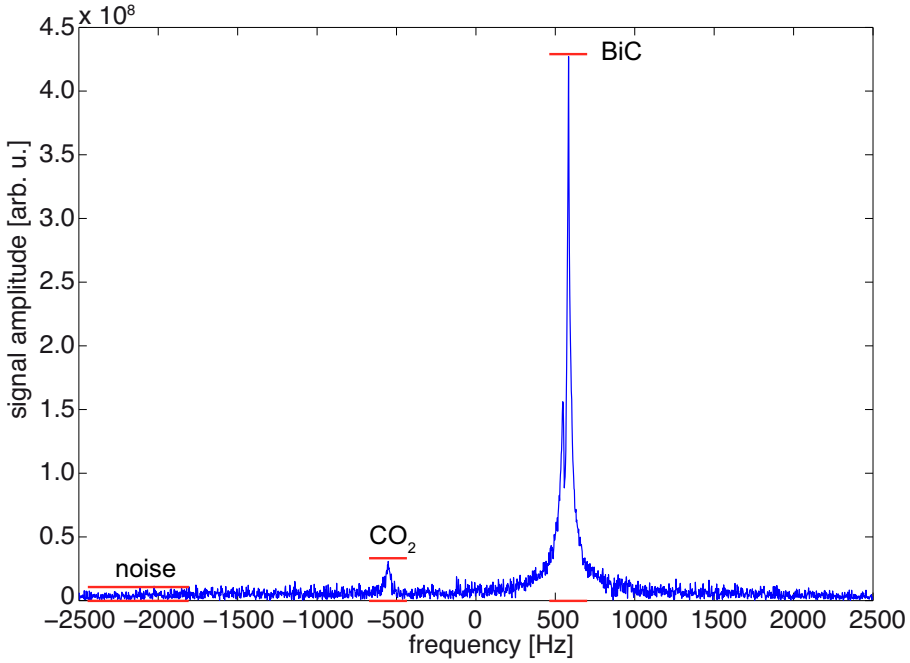

Figure 38: Representative spectrum of a 90° rat kidney slice of 10 mm thickness with a bicarbonate signal with a CSD of 1042 Hz (≈ 35 ppm), and the associated noise. The signal was acquired with a soft pulse and subsequent FID readout. The pulse is spectrally centered between the bicarbonate and the CO_2 resonance frequency. The calculated pH from the bicarbonate and CO_2 signal intensities is 7.34 and corresponds to blood pH.

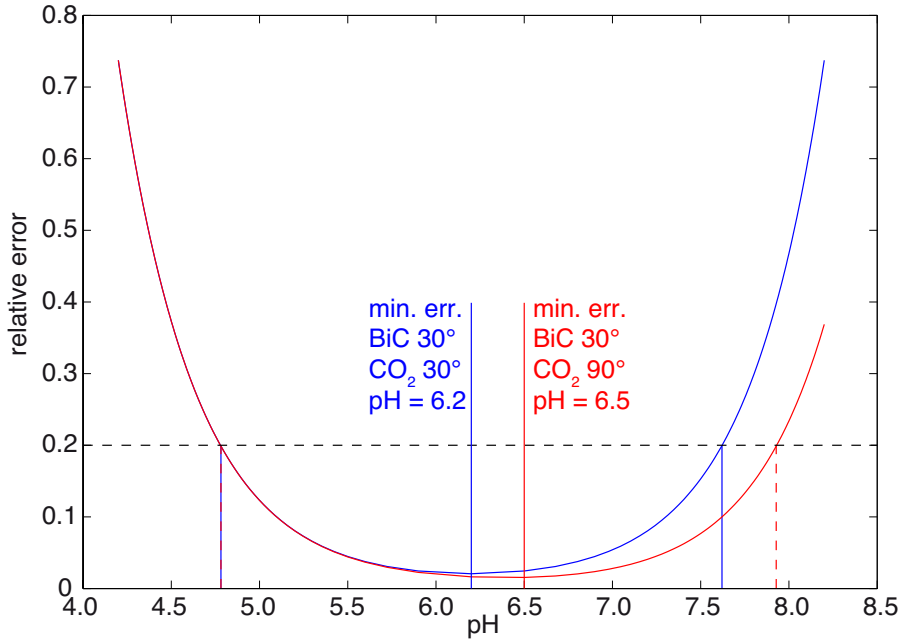

Figure 39: Simulated pH (x-axis) versus pH error (y-axis). Increasing the excitation flip-angle for CO_2 leads to a decreasing error and a wider range of accurate pH measurement. The point of lowest error (min. err.) shifts from pH=pKa=6.2 to pH=6.5.

4.2. pH quantification *in vivo* (methods):

The application of the spectral pH determination to the imaging domain requires enhanced acquisition techniques, like SPSP excitation for fast and signal-preserving imaging, which was designed (chapter 4.2.1) and characterized (chapter 4.2.2) in this work. Since residual excitation is a major problem for considerably differing signal intensities and for SPSP excitation, IDEAL separation was designed and added to the SPSP excitation protocol (chapter 4.2.3). Subsequently, the imaging methodology's sensitivity and errors were quantified (chapter 4.2.4) to obtain a self-contained analysis of the applied imaging method.

4.2.1 IDEAL spiral chemical-shift imaging for quantitative pH mapping

One option for achieving a separation of different metabolites by their respective chemical shifts in hyperpolarized measurements is to apply IDEAL spiral chemical shift imaging (CSI), which was shown to reliably enable the imaging *in vivo* using ^{13}C-pyruvate. To this end, a small flip-angle excitation is followed by single-shot spiral readout [56]. Frequency separation is achieved by shifting the echo time between the excitations, according to the principle of fat-water separation, introduced by Dixon in 1984 [106]. Flip angles are changed for each excitation to achieve a normalized signal intensity for each measurement, which is depleted during the successive excitations. The limitation of common IDEAL spiral CSI is using a constant excitation flip angle for all frequencies, which is unfavorable for two reasons. First, the bicarbonate is an injected metabolite and therefore has very high signal intensity due to its higher intravenous concentration compared with the low levels of CO_2, which must be produced from the bicarbonate. Second, the CO_2 signal is generally an order of magnitude lower at common *in vivo* pH levels (e.g., for a blood pH of 7.35, the ratio of the signal of the bicarbonate to that of CO_2 is 15 to 1). Therefore, it is preferable to use small flip-angle excitation for the bicarbonate magnetization and larger flip angles for CO_2. CO_2 must be excited with larger flip angles to overcome SNR issues. Combining SPSP excitation [57] with IDEAL separation [56] allows the excitation of different frequency bands separately with different flip angles. The SPSP pulses were centered at the resonance frequency of bicarbonate and CO_2, consecutively. The spectral excitation of the pulses depicted a periodic maximum across the frequency domain (see also Figure 42, B and D). This led to the unwanted off-resonance excitation of the other metabolite. During the pulse design process, attempts were made to minimize the off-resonance excitation, but it could not be completely eliminated [130]. To quantify the influence of the off-resonance excitation on the resulting pH maps, the residual signal was separated from the on-resonant signal with IDEAL encoding steps and investigated in terms of quantifying the error of the pH estimation. The bicarbonate and CO_2 resonance frequencies and the IDEAL encoding time shifts for frequency separation were determined. ΔTE was calculated for a CSD of 1140 Hz at 3 T for the two compounds with 0.3 ms for different flip angles (see 4.2.3).

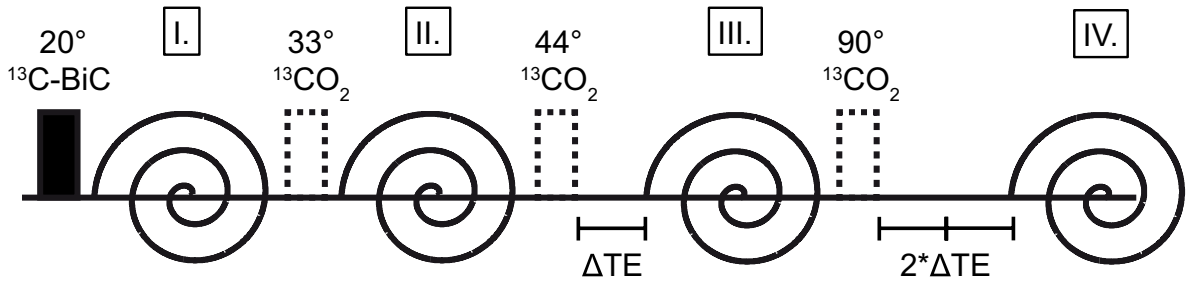

Figure 40: IDEAL SPSP acquisition scheme. ^{13}C-bicarbonate resonance frequency excitation (solid black) at a 20° flip angle with a subsequent spiral k-space acquisition (I.). $^{13}CO_2$ resonance frequency excitation with interleaved echo time ΔTE = 0.3 ms (dotted) for increasing flip angles and subsequent spiral k-space acquisition (II.-IV.).

The bicarbonate was excited first with a lower flip angle (20°) to conserve magnetization and an image was acquired with a spiral readout trajectory. Subsequently, CO_2 was excited with an SPSP pulse, whose excitation band was shifted to the resonance frequency of the CO_2. CO_2 was excited three times to ensure frequency separation with IDEAL encoding, each time with a different excitation flip angle (33°, 44°, 90°) to ensure comparable signal intensity for each excitation. Between each excitation, images were acquired using spiral readout trajectories.

4.2.1.1 *SPSP pulse design*

All SPSP pulses were designed according to [57]. Two different pulses were prepared with a fly-back design for *in vitro* and *in vivo* application (see Figure 42) at 40 mT/m gradient strength. The boundary conditions of the bicarbonate and CO_2 excitation were the CSD of the bicarbonate and the CO_2 of 35 ppm (~1140 Hz for 3 T field strength). Furthermore, the acquisition scheme is following an on-resonant excitation and subsequent shift of the on-resonant excitation band. Hence, it is necessary to develop a pulse that shows maximum excitation at 0 Hz frequency and minimum excitation at 35 ppm.

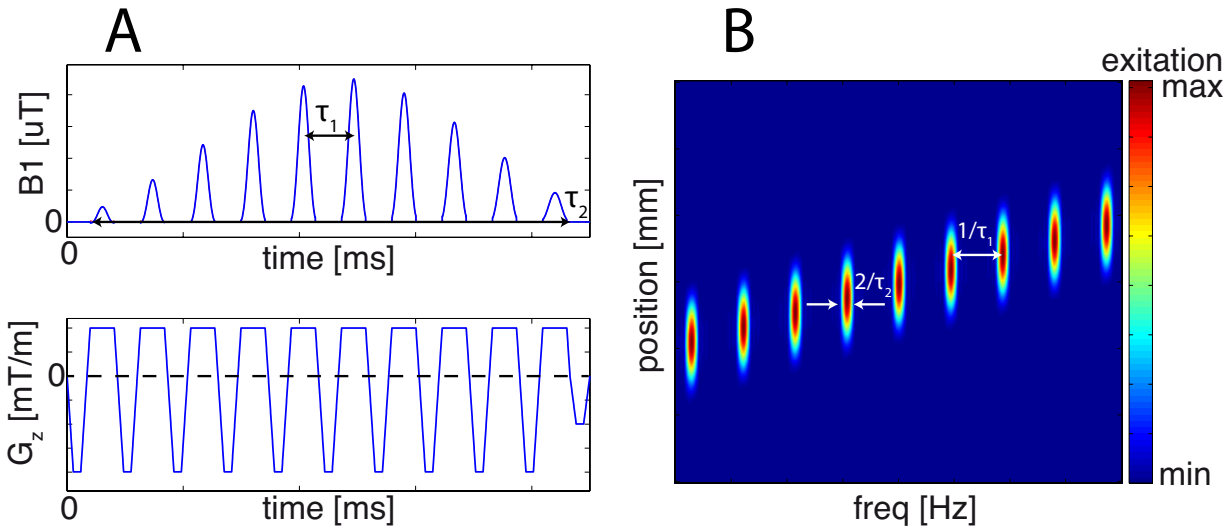

Figure 41: Relationship between the applied B1 (top, left) and the gradient waveforms (bottom, left) and the resulting spectral spatial excitation simulation (right figure) for bicarbonate and CO_2 excitation. τ1 denotes the duration between two sub-pulses. τ2 shows the net duration of the pulse (figure like [105]).

The expected excitation minimum can be estimated by calculating the duration of one fly-back pulse τ1, the number of sub-lobes used, and the excitation bandwidth for a given CSD. Using a constant excitation bandwidth allows to calculate τ1 for a defined number of sub-lobes. Pulse design was performed by minimizing τ2 to reduce the T_2* losses of the hyperpolarized signal during excitation. The minimum τ1 for the on-resonance at 0 ppm and off-resonance at 35 ppm can be written as

$$\tau 1 = \frac{n_{exc} - 0.5}{CSD} \quad (112)$$

and is correlated with the number of excitation lobes (n_{exc}) used to cover the desired bandwidth (see Figure 41). For a single excitation, $\tau 1_{min} = 0.43\,ms$, showing the smallest possible excitation during a sub-lobe to cover a CSD of 70 ppm, hence leading to a minimum at 35 ppm for the on-resonant excitation at 0 ppm. However, the MR system used is limited by its physical parameters, which are the maximum gradient strength ($G_{max} = 40\,mT\,m^{-1}$) and the gradient slew rate ($s_{max} = 150\,T\,m^{-1}\,s^{-1}$), prohibiting such short pulse lengths. As a consequence, multiple excitations of the repetitive excitation pattern must be used to cover the range of desired frequency. Another limitation is given by the envelope of the applied RF field, which should ideally be Gaussian-shaped to achieve maximum frequency selectivity. Here, the full width at half maximum (FWHM) is $2/\tau_2$. The minimum number of excitations with good spectral and spatial excitation properties was found to be $n_{ex_{min}} = 3$. Since the sampling rate of the sequencer is 4 µs, τ1 must be rounded to a multiple of this value, leading to $\tau 1_{min} = 2.164\,ms$. With the minimum pulse length, the numbers of B1 excitation sub-pulses and spectral excitation bandwidth can be adjusted for different excitation patterns, depending on the application of the pulses (e.g., *in vitro* / *in vivo*, see Figure 42).

For the quantification analysis, pH phosphate buffer phantoms were used and an SPSP was chosen based on pulse design. For *in vitro* and *in vivo* experiments, on-resonant frequency is estimated by the CSD of bicarbonate and CO_2 to a thermal ^{13}C lactate reference. For *in vitro* quantification, an SNR-optimized pulse was designed with maximum excitation at the center frequency and lowest residual excitation (<1 %) at 35 ppm CSD, where the CO_2 resonance is expected. A good SNR allows the performance of phantom measurements and quantification experiments. For *in vivo* application, a second pulse was designed to overcome chemical shift variations due to field inhomogeneities occurring during *in vivo* scans.

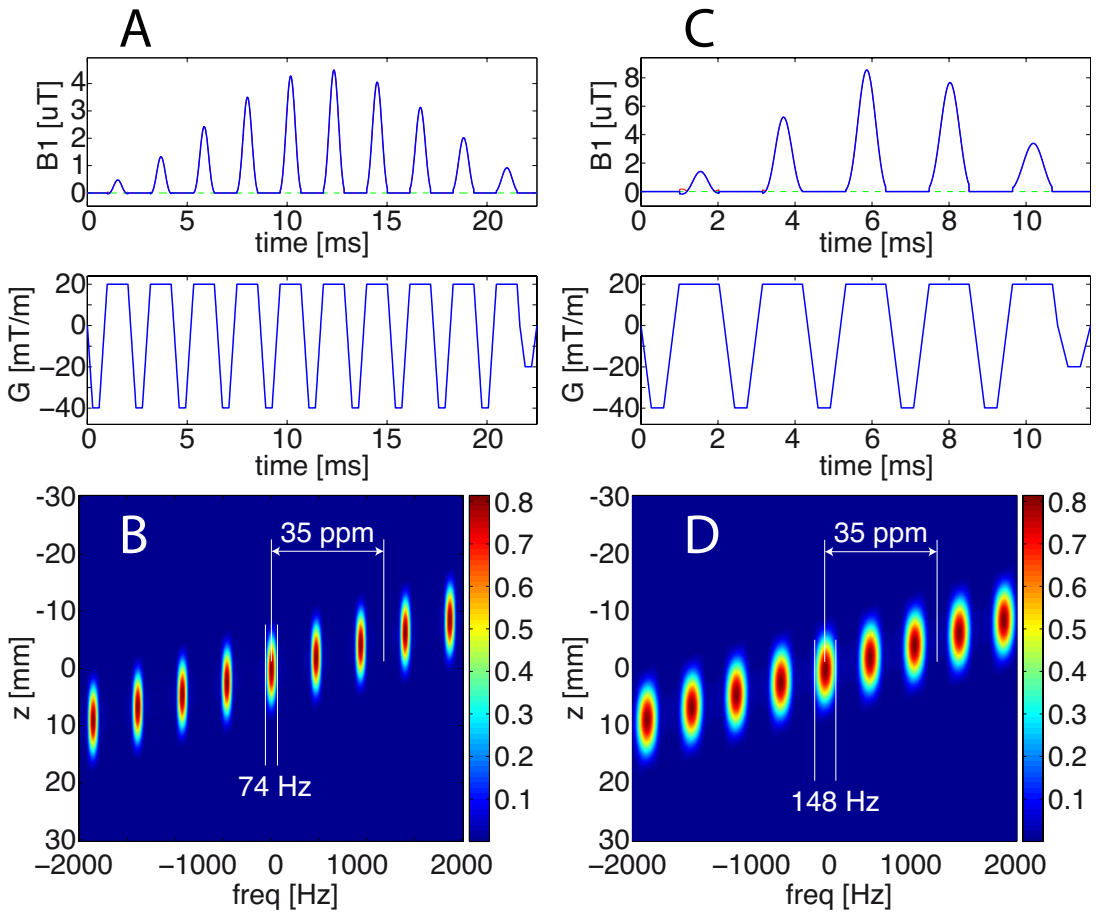

Figure 42: (A, top) 10 RF sub-lobes with a pulse duration of 22 ms. (A, bottom) A fly-back gradient at a maximum field strength of 40 mT/m leading to a spectral profile (B) suitable for *in vitro* measurements with an excitation band of 10 mm spatial and 74 Hz spectral excitation, a maximum at 0 Hz, and a minimum at 1140 Hz. (C, top) 5 RF sub-lobes with a pulse duration of 12 ms. (C, bottom) A fly-back gradient at a maximum field strength of 40 mT/m leading to a spectral profile (D) suitable for *in vivo* measurements with an excitation band of 10 mm spatial and 148 Hz spectral excitation, a maximum at 0 Hz, and a minimum at 1140 Hz.

Despite the fact that SPSP excitation can be very efficient for spectrally selective excitation, the residual signals originating from off-resonant frequencies (see Figure 47) from the broader spectral excitation of the designed *in vivo* pulse might become significant. The effect is usually negligible for small flip angles but has higher impact for larger flip angles. For optimal SNR during *in vivo* measurements, it is desirable to excite CO_2 with 90° pulses, which reflects the worst-case residual excitation error. Furthermore, the bicarbonate concentration is generally higher *in vivo*, because at this time point after injection, the concentration is still accumulated in the blood vessels due to the intravenous injection, which increases the error for the 90° CO_2 excitation even further. It is necessary to quantify the contribution of the residual-excitation bicarbonate to the CO_2 signal and estimate the error on the resulting pH map. This can be achieved by combining SPSP-spiral acquisition with IDEAL encoding steps for the CO_2 acquisition (see Figure 40), which allows separating the residual bicarbonate signal from the acquired CO_2 signal.

Not using the optimal parameters can easily lead to an excitation pulse of lower quality, resulting in excitation schemes with multiple off-resonance bands in the spectral and spatial

dimension (see Figure 43). This could lead to false signal excitation either in the spatial or the spectral domain or both.

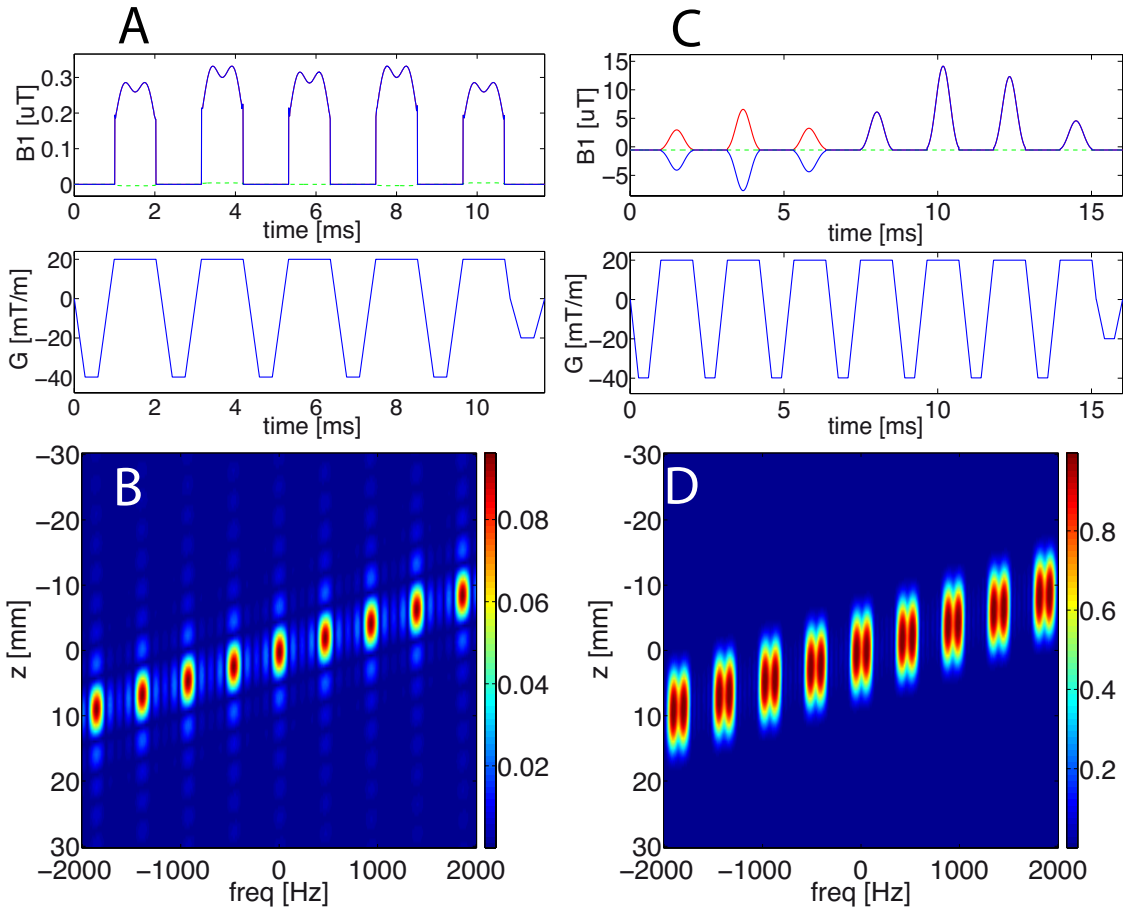

Figure 43: Pulse design for a spectral-spatial excitation and not optimized parameters for a pulse design with on-resonant excitation and an excitation minimum at 35 ppm. (A) The applied RF pulse (top) and gradients (bottom) for the case of an excitation bandwidth of 37 Hz. The excitation pulse is too short to achieve sufficient frequency resolution, which is reflected by the side-lobes in the spectral and spatial domain (B). It is also noteworthy that the maximum B1 is significantly smaller compared with the optimized pulses (see Figure 42). Thus, the on-resonant excitation is ≈0.12 and hence lower than the optimized pulses with excitations of ≈0.8. (C) Pulses and gradients for too many excitation steps (n=7), leading to a non-Gaussian-shaped envelope of the applied RF pulses. The resulting excitation simulation is shown in (D), with two maximum excitation lobes shifted by ±50 Hz, respectively, and a local minimum in between.

To evaluate the real performance of a designed SPSP pulse, thermal measurements were performed using a thermal phantom (NMR tube with a diameter of 10 mm and length of 15 cm). The proton phantom contained H_2O only. The ^{13}C phantoms contained 3M ^{13}C labeled lactate in H_2O and 4% DOTAREM. The phantoms were sampled in 4 Hz steps with the pulses designed in order to evaluate the on- and off-resonance excitation bands (see Figure 44).

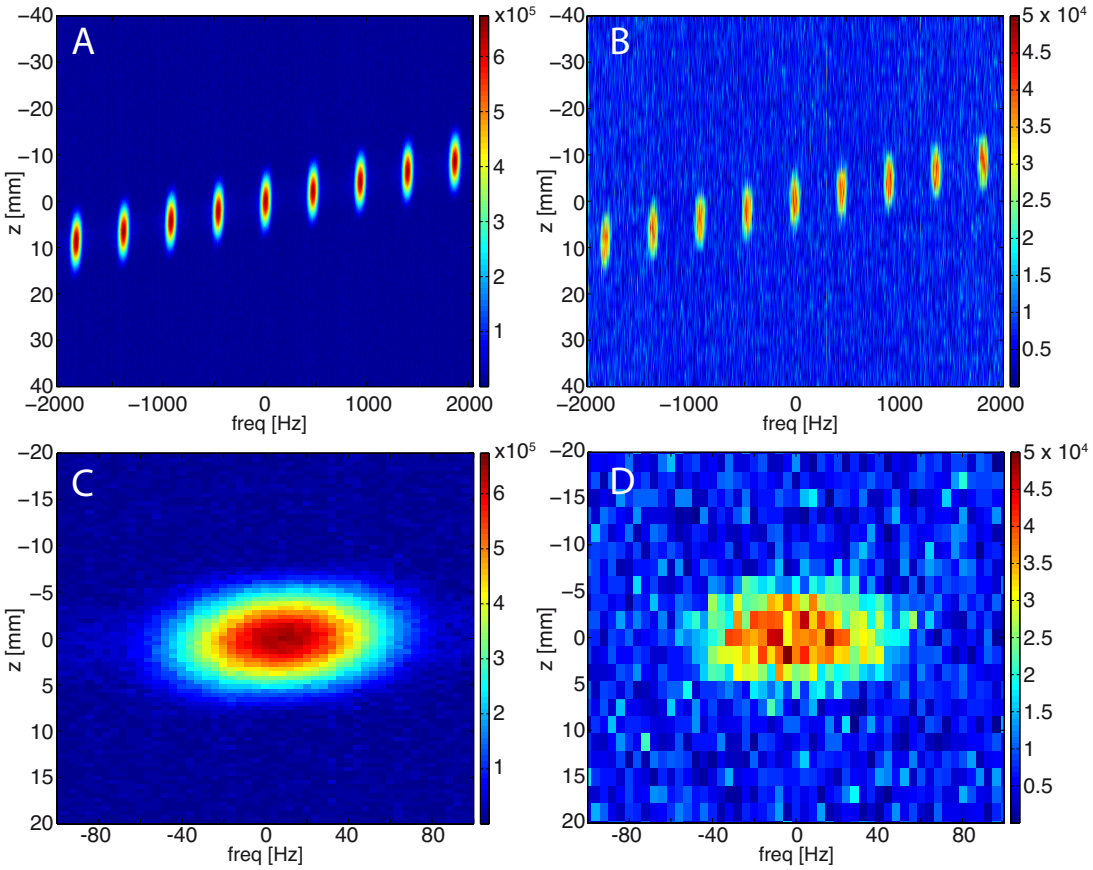

Figure 44: Evaluation of the *in vitro* (74 Hz excitation bandwidth) SPSP pulse performance with ^{1}H imaging on a H_2O phantom (left column, subfigures A and C) and ^{13}C imaging on a ^{13}C-labeled lactate phantom (right side, subfigures B and D). The excitations were performed with 90° each. The lower SNR of the carbon measurement can be explained by the lower concentration of ^{13}C and gyromagnetic ratio γ, compared with that of ^{1}H. The top row shows the full spectral bandwidth and the bottom row display a zoom of the on-resonant frequency band at 0 Hz. Both spectra exhibit good excitation at 0 Hz and low excitation at 1140 Hz, however, the on-resonance maximum is slightly shifted by about 12 Hz. The analysis reveals a good spatial excitation of 10 mm for proton and carbon excitation and a spectral excitation of ~80 Hz.

4.2.2 SPSP pulse performance test

After the successful evaluation of the designed pulses, spectral and image analysis were performed. An acquisition scheme for evaluating spectral and spatial performance of the SPSP pulses is shown in Figure 45.

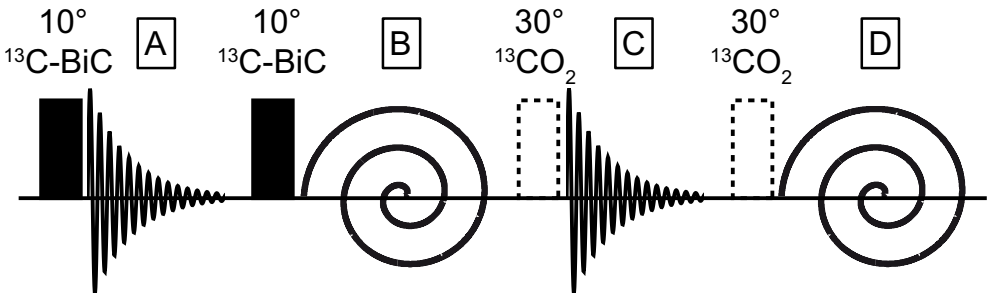

Figure 45: Acquisition scheme for SPSP performance test. The sequence starts with 10° on-resonant excitation of the bicarbonate (solid block), followed by FID readout (A). Subsequent 10° excitation at the bicarbonate resonance frequency with spiral trajectory readout (B). Shift to the CO_2 resonance frequency (dotted block) with 30° excitation and FID readout (C), followed by 30° excitation and spiral readout (D).

500 µl of hyperpolarized bicarbonate solution was added to pH phantoms containing 2.5 ml 0.2 M PBS buffer, set to pH 6 and 7. The excitation flip angles were chosen as 10° for bicarbonate and 30° for CO_2, respectively. After the first excitations for each nucleus, excitation spectral information was gained with FID readout. After the second excitations, image information was obtained with spiral readout trajectory. The results of the spatial analysis are shown in Figure 46.

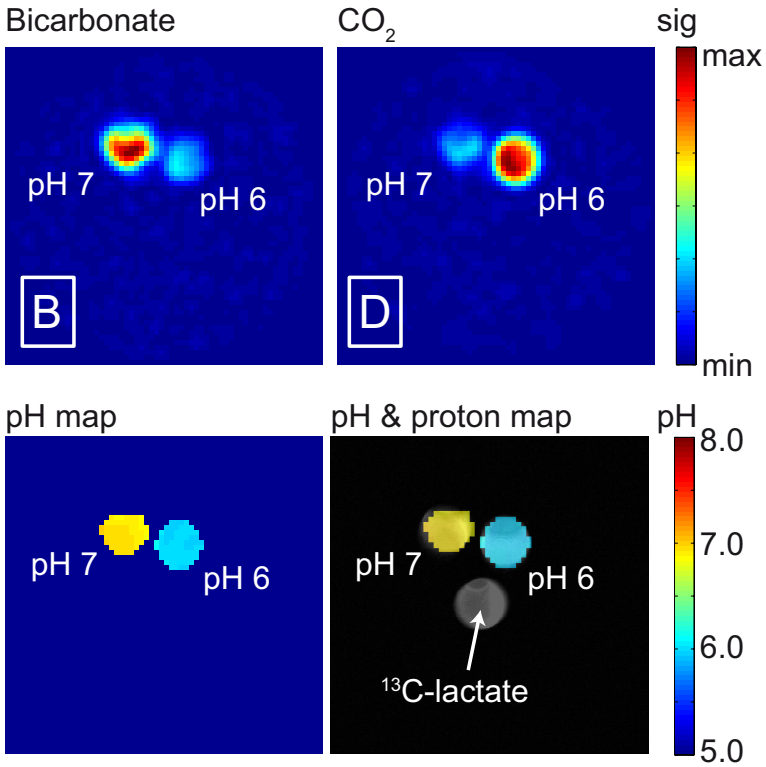

Figure 46: Image analysis of SPSP-excited spiral acquisition, measured at pH phantoms of different pH (values depicted in white numbers) with different flip angles (see acquisition scheme, Figure 45). The slice thickness is 10 mm. The top left figure depicts the signal intensity map of the bicarbonate originating from acquisition (B) in Figure 45. The intensity map shows a gauged shape due to air bubbles within the excited slice. The top right figure depicts the acquired signal intensity map of CO_2 originating from acquisition (D) in Figure 45. As expected, the intensity maps show a larger bicarbonate signal in the pH=7 phantom and for CO_2 in the more acidic phantom of pH=6. The lower left figure displays the calculated ^{13}C pH map from the two images, masked by SNR-based ROI. The lower right figure shows the resulting pH map of the two phantoms, overlaid with a proton map. Here, the additional thermal lactate phantom used for the calibration of the SPSP pulses is also visible.

The image analysis reveals a clear pH differentiation between the two phantoms. Higher concentrations of bicarbonate are measured in the more alkaline phantom (pH=7) compared with the acidic one (pH=6), and the reverse is observed for CO_2, as expected. The overlaying and registration of the ^{13}C data with the previously acquired proton maps lead to a clear distinction between the different pH values and demonstrate good pH estimation compared to the electrode reference values.

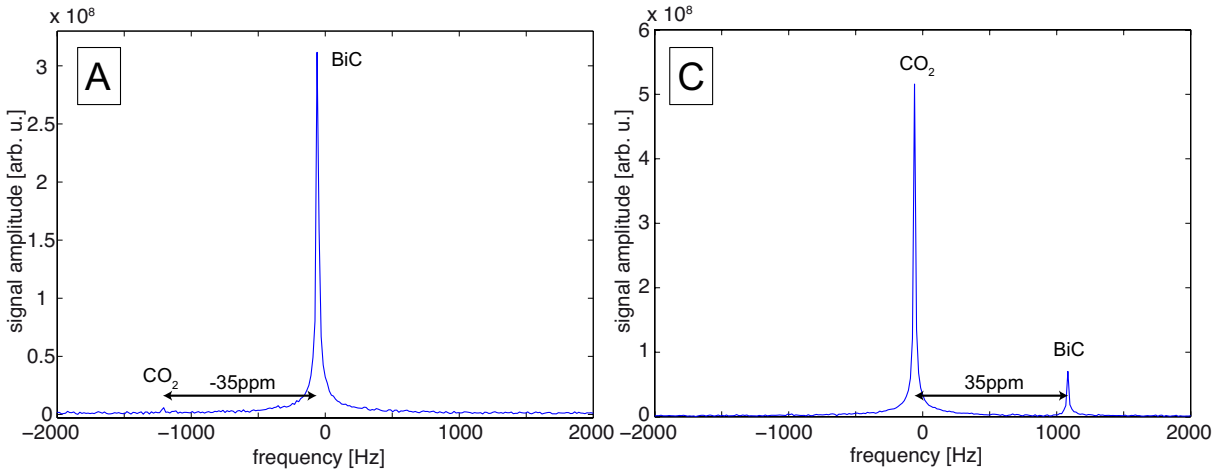

Figure 47: Spectral analysis of the SPSP pulse with different flip-angle excitation and subsequent FID readout. The left figure shows the excitation at the bicarbonate on-resonance frequency with 10° flip angle, originating from acquisition (A) in Figure 45. The spectrum shows large excitation at 0 Hz and almost no residual excitation at -35ppm, originating from CO_2. The right figure depicts the excitation at the CO_2 on-resonance frequency with 30° flip angle, originating from acquisition (C) in Figure 45. The spectrum shows large excitation at 0 Hz and noticeable residual excitation at 35 ppm, originating from bicarbonate.

The FID readout after the image acquisition of the corresponding molecule allows the performance of spectral analysis (Figure 47), which revealed a slight offset (~ -60 Hz) from the on-resonance frequency. This originated from the approximate estimation of the resonance frequencies of bicarbonate and CO_2, determined with the thermal lactate phantom (see Figure 46, lower right figure). The bicarbonate resonance exhibited a very good SNR, even at the low excitation flip angle of 10°. At a CSD of -35 ppm, very low residual excitation of the CO_2 was detectable. The CO_2 resonance also showed good SNR. However, the residual excitation of the bicarbonate was noticeable at 35 ppm CSD. The reason for this is the relatively high concentration of bicarbonate compared with CO_2 at these pH values. Additionally, the excitation flip angle of 30° leads to an almost 3 times larger excitation, which also occurs in the off-resonant regions. To estimate the impact on the resulting pH maps, the residual excitation error was evaluated in chapter 4.2.4.

4.2.3 IDEAL separation - number of signal averages determination

For the separation of two metabolites (e.g., bicarbonate and CO_2) with a chemical shift of $\Delta\omega$, it is necessary to determine the echo time ΔTE for the IDEAL separation. We assume that the signals of the metabolites are m_1, m_2 with chemical shifts $\Delta\omega_1 = 0$ and $\Delta\omega_2 \neq 0$, where m_1 is excited on-resonance, while m_2 shows the off-resonance signal. Measured at different times t_1, t_2, t_3 with a time difference ΔTE, the signals become:

$$s_1 = e^{i\Delta\omega_1 t_1}\rho_1 + e^{i\omega_2 t_1}\rho_2 \quad (113)$$

$$s_2 = e^{i\Delta\omega_1 t_2}\rho_1 + e^{i\omega_2 t_2}\rho_2 \quad (114)$$

$$s_3 = e^{i\Delta\omega_1 t_3}\rho_1 + e^{i\omega_2 t_3}\rho_2 \,. \quad (115)$$

with $\Delta\omega_1 = 0$ and $t_1 = 0$, the first parts of the sum become 1, leading to a signal matrix:

$$\vec{s} = \begin{pmatrix} 1 & 1 \\ 1 & e^{i\omega_2 \Delta TE} \\ 1 & e^{i\omega_2 2\cdot\Delta TE} \end{pmatrix} \cdot \vec{\rho} \quad (116)$$

$$\vec{s} = \mathbf{A} \cdot \vec{\rho} \quad (117)$$

where $\vec{\rho}$ is the intensity vector for each metabolite, which can be calculated by

$$\vec{\rho} = \text{inv}\,\mathbf{A} \cdot \vec{s}\,. \quad (118)$$

The determination of $\vec{s}$ requires at least $n \cdot \Delta TE$ steps to separate the n metabolites. Nevertheless, a higher number of $n \cdot \Delta TE$ steps lead to a better determination. In this work, for two metabolites, three encoding time steps (which correspond to an initial measurement and two echoes) were used to achieve proper determination and spectral separation.

The quality of signal separation and noise determination can be quantified by the number of signal averages (NSA), which is defined by [135,136]:

$$NSA_q = \frac{1}{(E^H E)^{-1}_{q,q}} \quad (119)$$

where H denotes the complex conjugate transpose of the chemical-shift-encoded matrix E of the q-th metabolite. To find the optimal echo time spacing ΔTE of a given frequency difference $\Delta\omega_2 - \Delta\omega_1$, a numerical analysis was performed to achieve the highest NSA, which is comparable to a least squares fit. The best fit is achieved when NSA equals the numbers of acquisitions of a set of measurements, e.g., $NSA = 2$ for two measurements of two metabolites, one on-resonance and one off-resonance. A second limitation in finding the optimum ΔTE is the T_2^* decay, since for n measurements, the signal decays as

$$S_n = S_0 \cdot e^{-\frac{\Delta T\cdot(n-1)}{T_2^*}}, \quad (120)$$

which can be minimized by choosing the shortest ΔTE of the numerical solution. S_n is the signal at the corresponding number of acquisitions n and S_0 is the signal at $t = 0$. For a CSD of 35 ppm at 3 T, as it is for bicarbonate and CO_2, ΔTE is determined as 0.3 ms (Figure 48). Due to the big CSD of 35 ppm (or 1140 Hz at 3 T) for bicarbonate and CO_2, ΔTE is rather short and therefore can be assumed to have a minor influence due to T_2* decay during acquisition.

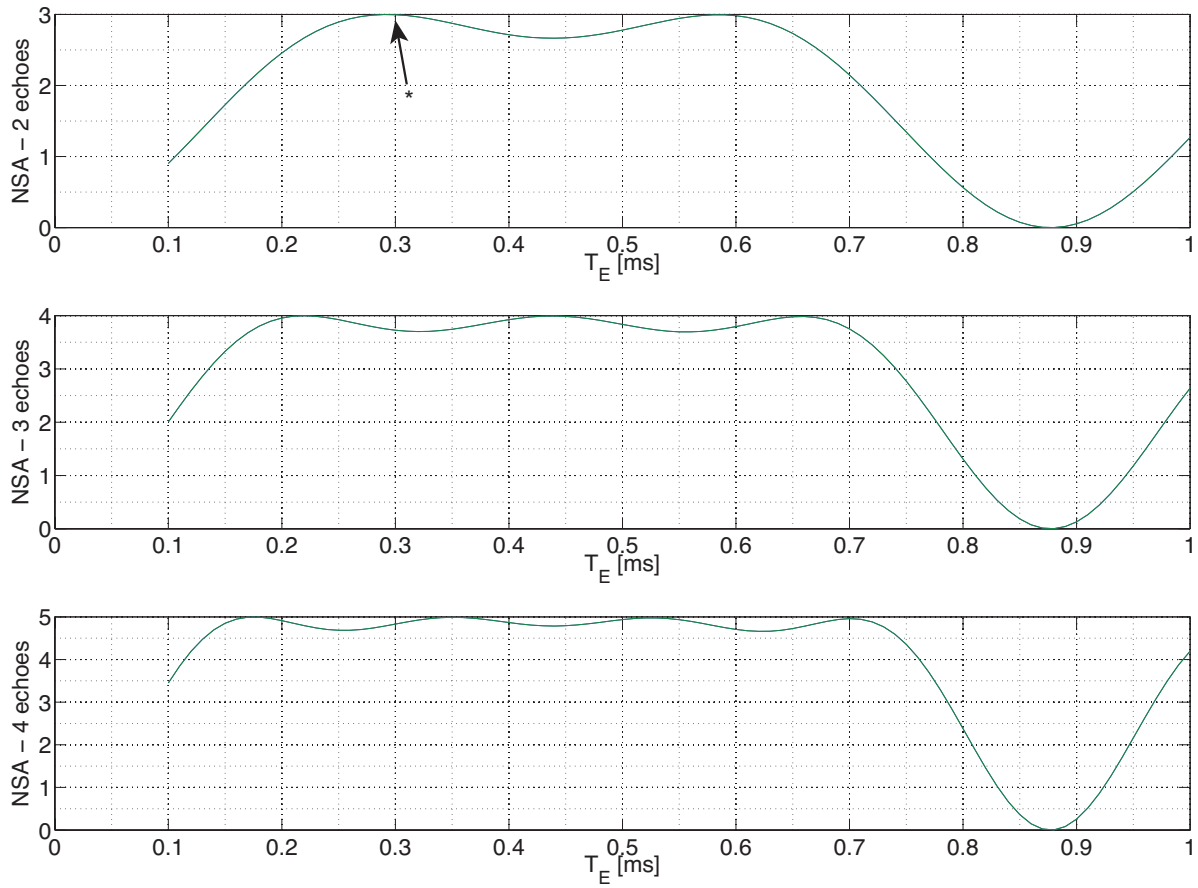

Figure 48: NSA simulation for 2 echoes (top), 3 echoes (middle), and 4 echoes (bottom). The simulations were performed for the on-resonant excitation ($\Delta\omega_1 = 0\ Hz$) and the off-resonance signal ($\Delta\omega_2 = 1140\ Hz$), which is similar to the CSD of bicarbonate and CO_2 of 35 ppm at 3 T. Increasing the number of echoes leads to a broader plateau of good NSA and steeper flanks, resulting in a rectangular appearance. The echo time used for IDEAL separation is marked with * (top) for two echoes, which shows an NSA value of 2.996.

4.2.4 Error estimation results IDEAL-SPSP

Efficient imaging is essential for the signal acquisition with SNR-limited methods, such as hyperpolarized ^{13}C imaging. Combining SPSP excitation and spiral readout builds the base for fast and SNR-preserving measurement conditions. However, this method suffers from residual off-resonant excitation. Since the excitation from off-resonances cannot be avoided completely, it is necessary to quantify the inherent SNR-dependent error, and demonstrate its impact on hyperpolarized ^{13}C bicarbonate pH images. IDEAL separation requires multiple excitations, which was not possible for CO_2 *in vivo*, hence the quantification was performed *in vitro* using pH phantoms and IDEAL-SPSP spiral imaging acquisition.

4.2.4.1 *Preparation of pH phantoms*

The pH buffer phantoms were prepared with sodium phosphate dibasic (Sigma Aldrich) in D_2O and adjusted to a particular pH using 1 mol/L HCl solution to a final concentration of 1 mol/L. The pH levels were adjusted to values from 6.6 to 7.6 with a ΔpH of 0.2 using a ROSS glass microelectrode (Thermo Scientific) connected to a pH meter (Thermo Scientific) as reference. 500 µl of the hyperpolarized bicarbonate solution was mixed with 2.5 ml of the pH-

adjusted phosphate buffer in 3 ml syringes. During the experiments, the phantoms were mixed directly after dissolution with the hyperpolarized liquid and subsequently placed in the volume coil and measured at different times after dissolution. The pH was measured using a glass microelectrode again after mixing.

4.2.4.2 *IDEAL-SPSP separation*

The error in the pH values depends on the residual excitation of bicarbonate and was investigated *in vitro* (see Figure 49). A non-IDEAL pH map was calculated using the first acquisition of the IDEAL-encoding CO_2 step (see acquisition II. in Figure 40) and the bicarbonate measurement (see acquisition I. in Figure 40). The IDEAL-corrected pH map is based on the CO_2 map, as corrected for the residual bicarbonate. The comparison of these maps shows excellent correlation between the pH electrode values and the calculated pH obtained from *in vitro* measurements. Acquisitions were performed 50 s, 60 s, 70 s, and 80 s after dissolution to evaluate the stability of pH measurements over time (see also Figure 50).

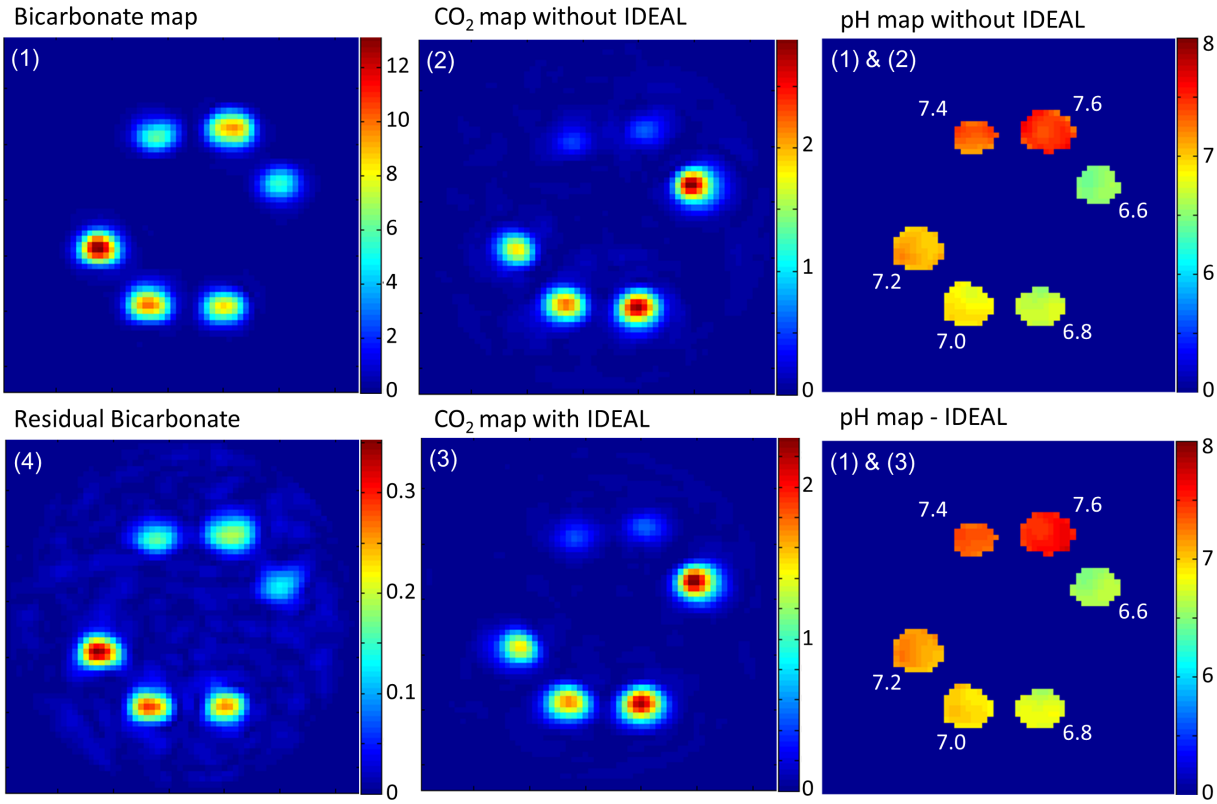

Figure 49: pH phantoms, adjusted with a pH electrode to values ranging from 6.6 to 7.6 in steps of 0.2 (white numbers in the top right and bottom right picture), containing 2.5 ml of 1 mol/L of phosphate buffer with 0.5 ml hyperpolarized bicarbonate added. The left and middle columns show intensity maps of the bicarbonate and CO_2 after SPSP excitation and spiral acquisition. The top right pH map is calculated using intensity maps (1) and (2) without IDEAL correction of the residual bicarbonate signal (4) from SPSP-excited spiral acquisition at the CO_2 resonance frequency. The bottom right pH map, based on maps (1) and (3), was obtained with the IDEAL correction for residual bicarbonate. The signal intensity maps (left and middle column) of the bicarbonate and CO_2 are normalized to the highest signal intensity (dark red). The pH values of the maps are scaled as shown in the color bars next to each panel.

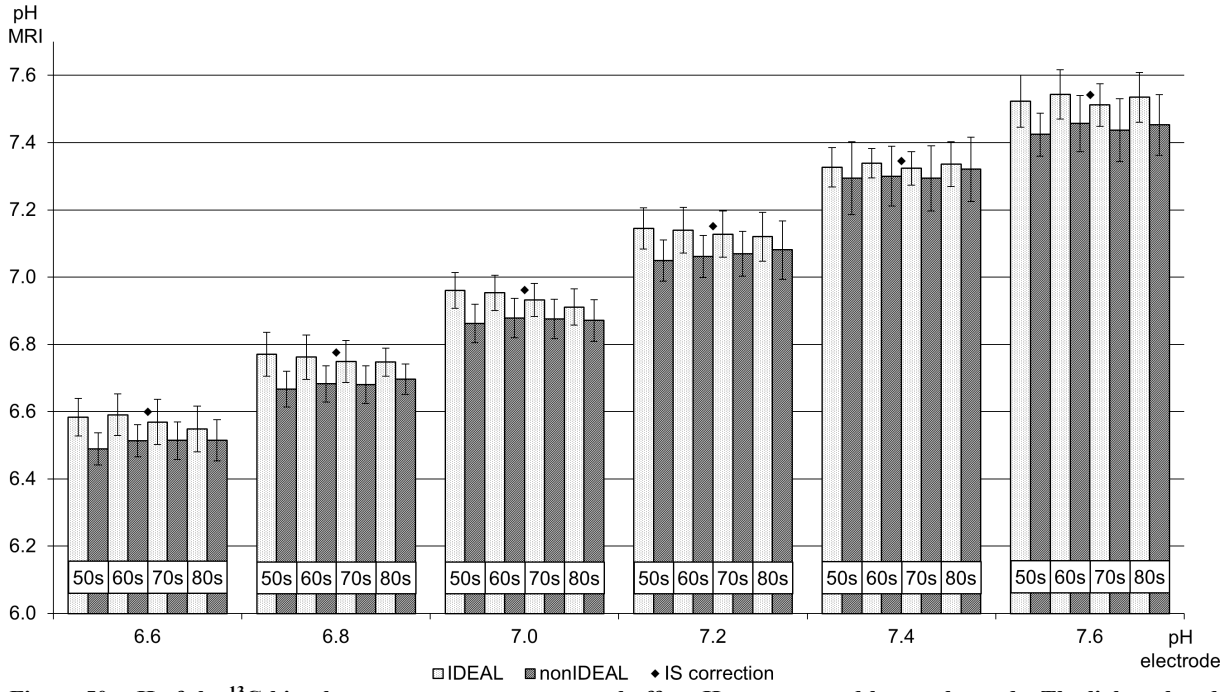

Figure 50: pH of the ^{13}C-bicarbonate measurement versus buffer pH, as measured by an electrode. The light-colored bars show the IDEAL-corrected measurements. The dark bars display non-IDEAL corrected measurements. The error bars reflect the standard deviation within the ROI. Since pH equilibrium requires a time of 40 s without the addition of carbonic anhydrases, measurements were performed after 50 s and in subsequent 10 s steps. Due to the highly concentrated pH buffers, the pH electrode values are biased by the ionic strength (IS) influence. The IS correction was performed for each pH value (black diamonds).

Figure 50 shows that pH values were detected with good time stability over a range of 30 s. The heterogeneity in the regions of interest is small and time-independent. In comparison with the established acceptable range, pH was estimated to a good approximation with the electrode at low pH. All pH values measured by the electrode have an intrinsic error associated with ionic strength due to the high buffer concentrations of 1 mol/L. This error leads to a biased pH value compared with the value estimated with MRI. After correction of the pH electrode values for the positive ionic strength bias, the pH values measured by MR showed excellent correlation with the electrode values within the ROI using the IDEAL correction for the values measured with MR. The separation of the residual bicarbonate signal at the CO_2 excitations via IDEAL shows that there is noticeable residual excitation for the *in vivo* enhanced pulse due to the broader excitation bandwidth. On the other hand, the pH map comparison shows that in the end, the residual excitation has a negligible effect on the mapped pH and only produces a small bias of approximately 0.1 pH units. This bias can be explained from the high CSD of 35 ppm between the bicarbonate and the CO_2. When the residual bicarbonate signal is reconstructed at the frequency of CO_2, the false signal blurs out. The effect increases with larger CSD and therefore the residual bicarbonate signal only leads to a slightly higher noise. The *in vivo* application of IDEAL separation is useful for overcoming a small residual excitation. However, within the scope of this work, considering an experimental setup implementing pH-imaging in a clinical 3 T scanner, the SNR of the CO_2 for *in vivo* measurements is too small for multiple excitations. Hence, IDEAL separation was not applied *in vivo* in the following. Using, for example, higher field strengths, stronger

gradients for a higher resolution, and an improved coil setup (e.g., surface coils) could improve the SNR further and overcome the limitations for the subsequent quantification of the off-resonant error in *in vivo* conditions.

4.2.4.3 *Ionic strength correction*

Measurements with glass electrodes show inherent error sources when measuring highly concentrated ionic solutions. Cations can exchange protons with the glass membrane of the pH electrode, which results in a "false" membrane potential and produces a false pH estimation. Since pH is dependent on proton activity, charged ions have a non-negligible influence on pH measurements at higher ionic concentrations. The influence of ionic strength on activity calculations was implied by the *Debye* and *Hückel* in 1923. Here, the ionic strength I can be calculated by [111]:

$$I = \frac{1}{2}\sum_i z_i^2 m_i \ , \qquad (121)$$

with respect to the molality m_i and charge z_i for the i-th ion. The ionic strengths can subsequently be used to calculate the activity coefficient with:

$$\log a_z = \frac{P_1 |z_+ z_-| \sqrt{\left(\frac{I}{m^\ominus}\right)}}{1 + P_2 \sqrt{\left(\frac{I}{m^\ominus}\right)}} \ , \qquad (122)$$

where the parameter P_1 depends on the dielectric constant of the solvent (= 0.509 for H_2O at 25°C) and P_2 is a dimensionless constant describing the shortest distance between ions. The formula can be simplified to:

$$a_z = 10^{\frac{-0.51\, z^2 \sqrt{I}}{1+\sqrt{I}}} \ , \qquad (123)$$

and the activity of any charged ion is then:

$$a_i = a_z \, m_i \ . \qquad (124)$$

This approach works well for concentrations <0.1 mol/L. For higher concentrations, there are other approaches [137] that calculate the change of activity of the solvent and then recalculate it for every compound c with chemical potential μ_c and amount n_c (Gibbs-Duhem equation):

$$\sum_c n_c \, \mathrm{d}\mu_c = 0 \ . \qquad (125)$$

Calculations of the ionic strength influence were performed for sodium phosphate buffers at different concentrations. The ionic strength influence was low for low concentrations and increases significantly for higher concentrations (see Table 10).

pH	10 mmol/L	100 mmol/L	1 mol/L
6.6	0.0154	0.1840	2.3555
6.8	0.0175	0.2090	2.5509
7.0	0.0198	0.2332	2.6974
7.2	0.0222	0.2527	2.8030
7.4	0.0243	0.2682	2.8725
7.6	0.0260	0.2791	2.9191

Table 10: Ionic strength calculation for sodium phosphate buffers at different pH and concentrations.

In addition to the increasing influence at increased concentrations, the ionic strength also increases with increasing pH of the buffer. This can be explained by the chemical properties of the buffer: sodium phosphate buffers are set to distinct pH values by the following chemical equilibrium of the monobasic and dibasic form:

$$Na_2\mathrm{HPO_4} \underset{\mathrm{pH}}{\Leftrightarrow} \mathrm{NaH_2PO_4}\,. \qquad (126)$$

At increased pH, higher concentrations of disodium phosphate lead to a higher influence of the charged ions (here, Na^+) and thus higher impact of the ionic strength to the pH measurements. Once the pH values measured by the reference electrode are corrected for ionic strength influences, the pH measurements with NMR show very good correlation (see Figure 50).

4.3. pH quantification *in vivo* (healthy)

To obtain information about the *in vivo* behavior of the injected bicarbonate, slice-selective spectral perfusion tests were performed that show the signal evolution after systemic injections (chapter 4.3.1). These properties allowed the application of the previously presented imaging modalities to image bicarbonate *in vivo* (chapter 4.3.2) and derive T_1 for different organs (chapter 4.3.3).

4.3.1 Different slices – perfusion test

It is possible to investigate different slices of different organs of a rat with one single injection by injecting the hyperpolarized substance via the tail vein. From the point of injection, the hyperpolarized liquid spreads through the whole body of the rat until it reaches the targeted organ. Although this distribution is fast, owing to the fast heart rate 300-400 bpm of a narcotized rat, the kinetics of the distribution is different for different organs. This has a significant impact for bicarbonate, since pH is dependent of the established ratio between bicarbonate and CO_2 equilibrium, which is disturbed by the injection of the bicarbonate. Hence, the signal evolution was tested for systemic injections via the tail vein.

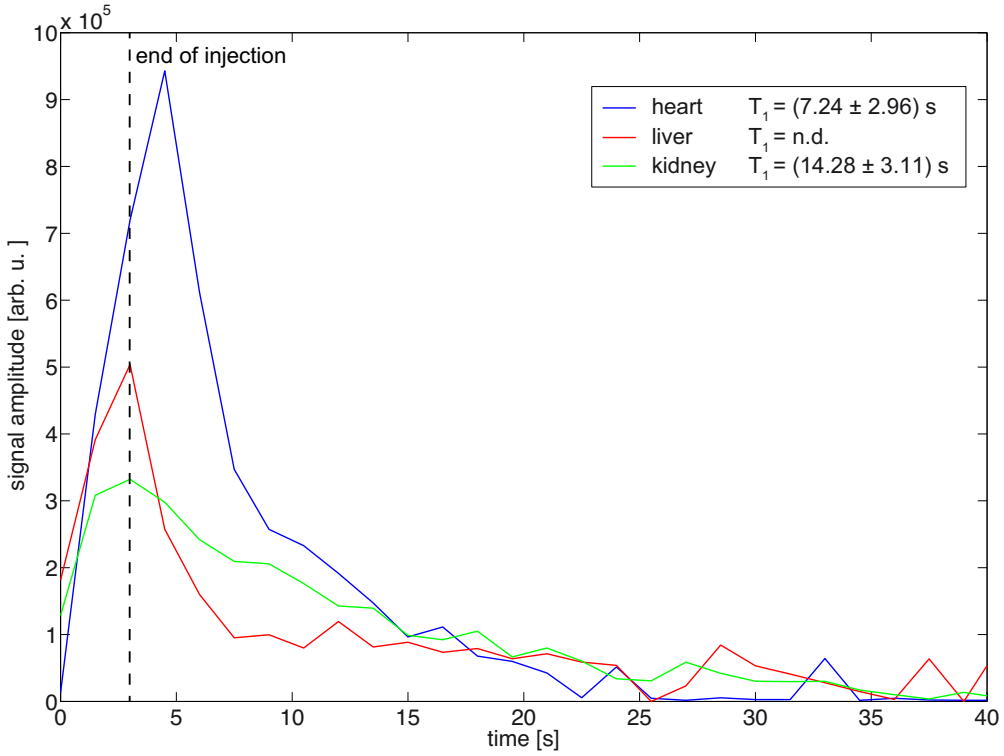

Figure 51: Hyperpolarized bicarbonate signal evolution. Acquisition of different organ slices of a healthy Lewis rat with a slice thickness of 10 mm. Soft pulse sequence with FA=15° excitation and acquisition with subsequent FID readout with a TR=1.5 s. Peak integration was performed with the AMARES algorithm. The injection and start of measurement were performed 24 s after the end of dissolution (t=0 s). The end of the injection was at t=3 s (marked with the dotted line). T_1 was estimated 6 s after bolus. The errors reflect 95% confidence bounds of the mono-exponential fit. The liver T_1 could not be fitted with mono-exponential decay.

As can be seen from Figure 51, the injection bolus could be tracked by the hyperpolarized signal. The injection volume was 2.5 ml per kg rat weight. After 3.5 s, the injection was finished and the decay was observed. The maximum signal intensity was located in the heart, which can be explained by the highest blood volume in the acquired slice. The maximum for the liver and kidney signal was observed at an earlier time point. This can be explained by the venous injection via the tail vein: the bolus moved from the tail directly to the heart and, from the positioning of the rat, it first passed the kidney and liver slice before arriving in the heart slice. The behavior of the T_1 decay shows similar values, as described in chapter 4.3.3. The liver signal showed the fastest decay and hence no mono-exponential fit could be applied. This can be explained by the high ratio of intravascular signal within the slice: after the bolus has decayed, most of the signal has decayed. The kidneys showed the lowest maximum signal intensity. In contrast, it showed a slower T_1 decay. Comparing the signal decays leads to the following order: $decay_{liver} > decay_{heart} > decay_{kidney}$. This indicates a higher ratio of the extravascular signal, which is more robust against bolus decay. Since pH mapping is highly SNR-limited, the injection volume was subsequently increased to the maximum allowed value of 5 ml per kg rat weight (see Figure 52). The injection time increased from 6 to 13 s. The maximum signal intensity was again visible in the heart, followed by the liver and kidneys. However, the signal intensities of liver and kidneys showed similar values. To investigate the signal behavior during and after injection for the different slices, the injection was stopped between t=5 s - 8 s and resumed afterwards. This led to a signal drop in the liver and heart slices, whereas the liver slice seemed again to be affected earlier than the heart slice. It is noticeable that the drop in signal was not visible for the kidney slice. This supports the previously stated assumption that the hyperpolarized bicarbonate signal from the kidney slice is not predominantly dependent on the signal of the main blood vessels, mainly the *vena cava*, but on the extravascular signal. T1 determination was not possible due to the higher flip-angle excitation and corresponding large error during the flip-angle correction for perfusion and diffusion effects.

Comparing the maximum signal amplitudes of the two injections leads to an interesting effect: normalized to the heart signal, the maximum signal amplitudes lead to the following signal ratio: $\text{signal}_{heart} = 1 : \text{signal}_{liver} = 0.54 : \text{signal}_{kindey} = 0.35$. Doubling the injection volume and the injection time resulted in a changed ratio: $\text{signal}_{heart} = 1 : \text{signal}_{liver} = 0.71 : \text{signal}_{kidney} = 0.64$, which indicated an almost doubled signal for the kidney slice. An explanation for this observation could be the previously mentioned impact of the bolus signal. Due to the temporary injection stop, this resulted in an overall decreased signal in the heart and liver slice, but not in the kidney slice.

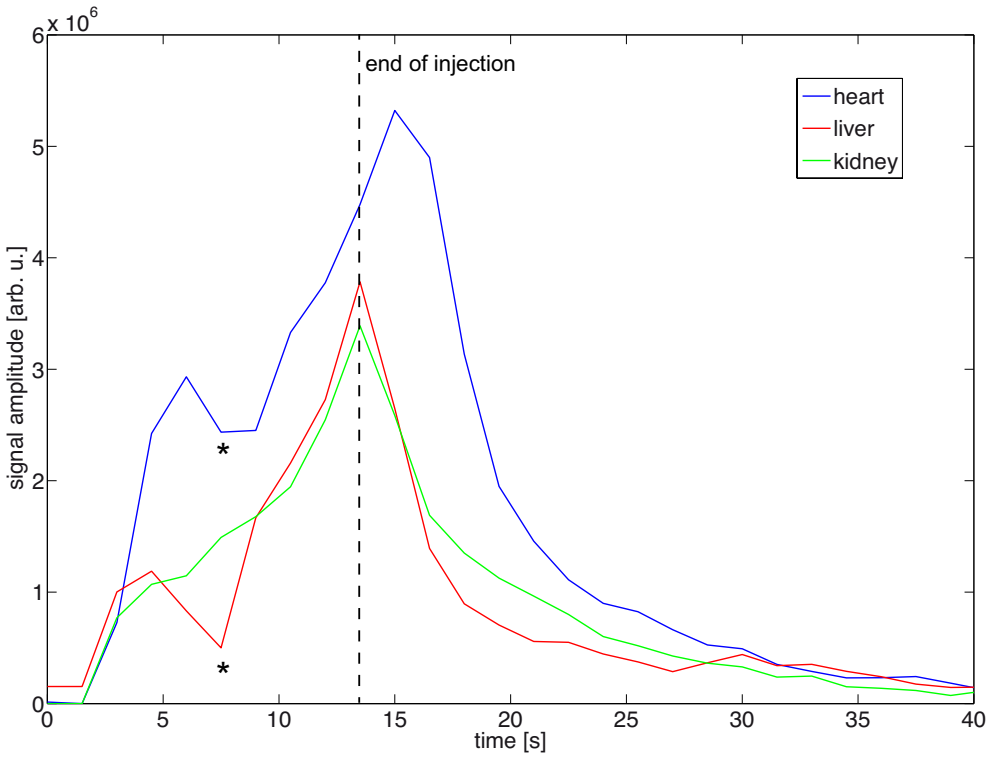

Figure 52: Hyperpolarized bicarbonate signal evolution. Different organ slices of a healthy Lewis rat with a slice thickness of 10 mm soft pulse sequence with FA=30° excitation and acquisition with subsequent FID readout with a TR=1.5 s. Peak integration was performed with the AMARES algorithm. The injection and start of measurement were performed 18 s after the end of dissolution (t=0 s). The end of the injection was at t=13.5 s (marked with dotted line). The injection was stopped at t=5 s for 3 s and subsequently continued. This resulted in a drop of signal (marked with *) in the heart and liver slice.

4.3.2 Maps of organs

Since the measurement were performed with a volume coil instead of a surface coil, it was possible to acquire different slices of organs with a single injection of hyperpolarized bicarbonate. It is beneficial to compare different bicarbonate distributions in different organs simultaneously, since this reduces several variables of a hyperpolarized measurement compared with multiple experiments; examples include different bicarbonate batch properties and different physiological conditions (e.g., heart rate and breathing) of the rat at different time points. Owing to the presence of carbonic anhydrases and the corresponding immediate bicarbonate to CO_2 equilibrium, the best time point of pH measurement can be defined as the point where the bicarbonate is well distributed in the tissue of interest and still exhibits sufficient SNR. The injections were performed through the tail vein of the rat, hence the distribution of bicarbonate was different for organs of different distribution within the body. In addition, some organs were better perfused (e.g., kidneys) than others (e.g., skeleton muscles). Therefore, before acquiring organ pH maps, it is necessary to perform a distribution analysis (see Figure 53).

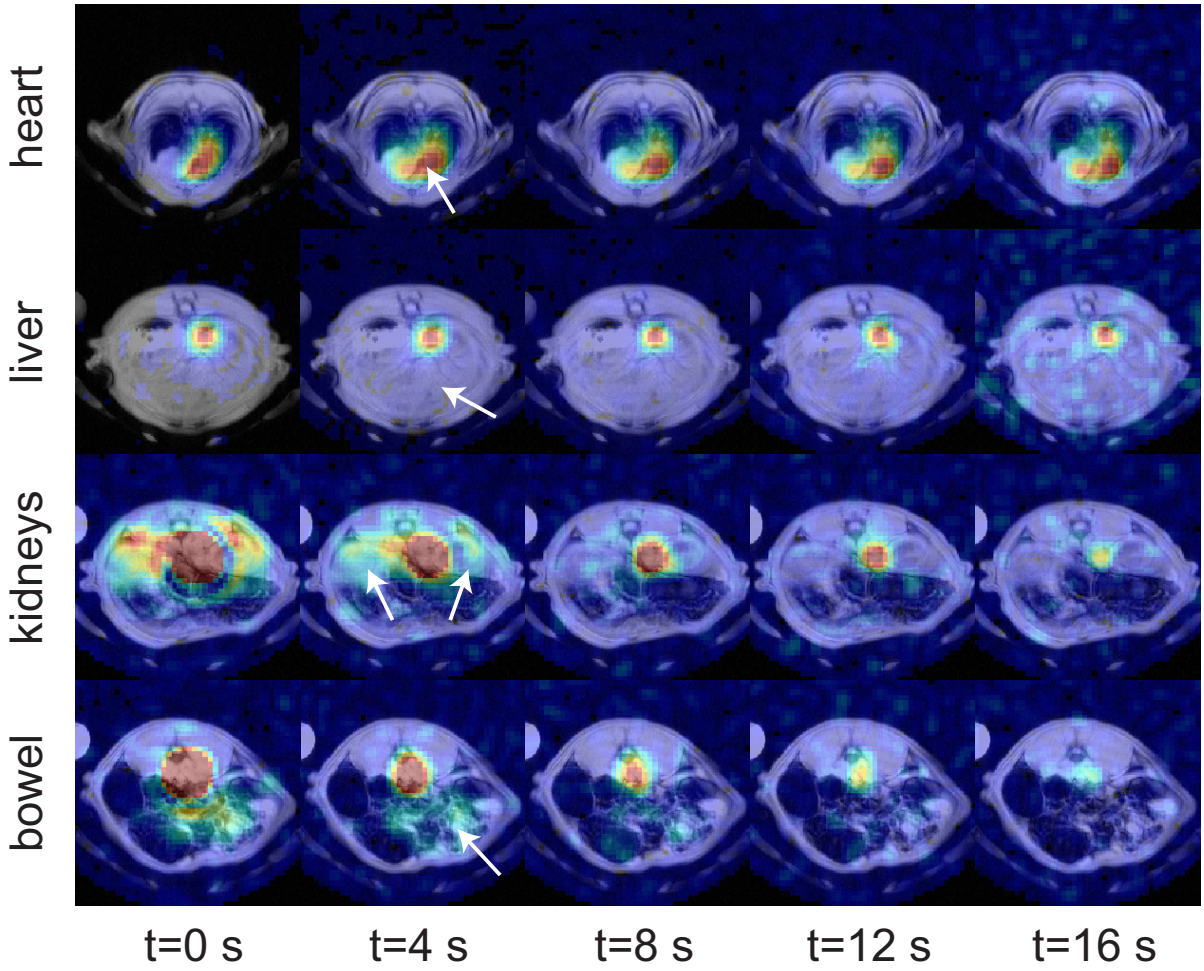

Figure 53: ^{13}C-bicarbonate signal after a tail-vein injection (21 s after dissolution) of approximately 1 ml hyperpolarized solution at different times for different cross sections. The positions of organs are marked with white arrows in the t = 4 s series. A 10° flip-angle excitation was used, with frequency-selective SPSP pulses applied on-resonant at the ^{13}C-bicarbonate resonance frequency, and subsequent spiral trajectory readout. Cross section thickness = 10 mm, FOV = 8 cm · 8 cm. The signals from the heart and liver were normalized to the maximum peak intensity. The signals from the kidney and bowel were normalized to a fixed value for better visibility of the bicarbonate in the peripheral tissue.

Hyperpolarized ^{13}C-bicarbonate solution was injected via a tail vein and data acquisition began immediately after injection. The bicarbonate kinetics was acquired with $\Delta t = 4$ s for four cross sections: heart, liver, kidney, and bowel. Voxel-wise signal intensity analysis was performed for intravascular bicarbonate. The bicarbonate *in vivo* signal decay changed during acquisition, leading to different T_1 (see Figure 57). This is an indication for different perfusion parameters within the organs. The heart cross section, measured directly after injection (t = 0 s), showed a distribution of bicarbonate only in the right ventricle, where it arrived after injection, as expected. It then spread to the left ventricle with increasing time. The kidney, and bowel sections exhibited bicarbonate concentrations predominantly in the *vena cava*. The liver sections only showed bicarbonate in the *vena cava*. Although the liver was well perfused, no bicarbonate signal was visible. Since the liver is an essential part of homeostasis, this might be due to bicarbonate conversion in the liver during urea production (see Figure 54) [138]. The kidney section showed a maximum bicarbonate concentration

directly after injection. This reflects the high perfusion of the kidneys. The bowel tissue was well perfused at t = 0 s and the signal decayed with increasing time. The decay of the ^{13}C-bicarbonate signal can be attributed to multiple factors: the hyperpolarized signal decays *in vivo* with a T_1 of approximately 10 s. In addition, the hyperpolarized signal is consumed for every excitation. Meanwhile, the bicarbonate is filtered by the kidneys, converted by the liver, constantly converted to CO_2 in the blood and tissue, and subsequently exhaled.

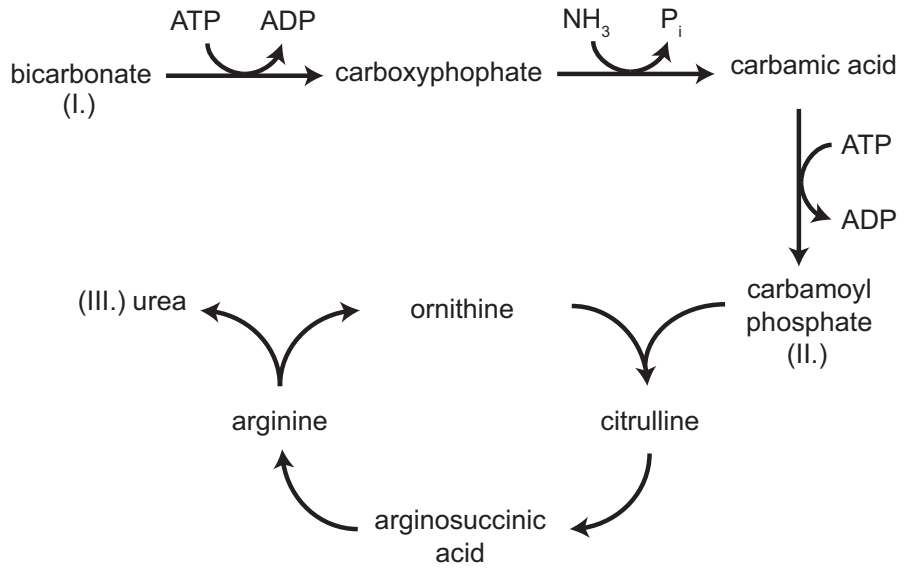

Figure 54: Schematic view of urea cycle with bicarbonate (I.), which binds ammonia (NH_3) and acts as a carbon source for the carbamoyl phosphate (II.). This is subsequently fed into the cycle reaction, in which urea (III.) is produced.

This could make bicarbonate an interesting liver disease marker for cases where functionality is disturbed, e.g., at hepatocellular carcinoma or liver cirrhosis. Hence, the spatial bicarbonate accumulation could indicate a changed bicarbonate consumption behavior and a corresponding disorder.

The distribution of the bicarbonate is dependent on the target organ, which makes it difficult to estimate an ideal measurement timeframe and must be investigated in each case. In general, bolus detection should be avoided to minimize errors that arise from the variation of perfusion between organs. Owing to the very low $^{13}CO_2$ signal intensity, multiple excitations and the acquisition of $^{13}CO_2$ kinetics was not feasible. Therefore, the imaging is limited to acquisition schemes using configurations such as a 90° flip-angle excitation for the $^{13}CO_2$. To determine spatial pH, a high SNR for both the bicarbonate and CO_2 signals is needed. Hence, it is crucial to determine the ideal moment of acquisition, when the hyperpolarized ^{13}C-bicarbonate is diffused to the targeted tissue and the signal has not decayed. This moment is again dependent on tissue perfusion and on where in the body the injection is performed.

4.3.3 Determination of ^{13}C-bicarbonate T_1 *in vivo*

The longitudinal signal evolution of the hyperpolarized ^{13}C-bicarbonate was investigated with the intention of identifying the appropriate time to begin image acquisition. The bicarbonate

signal intensity of the highest intensity voxel at $t = 0\ s$ is different for different organs (see Figure 55).

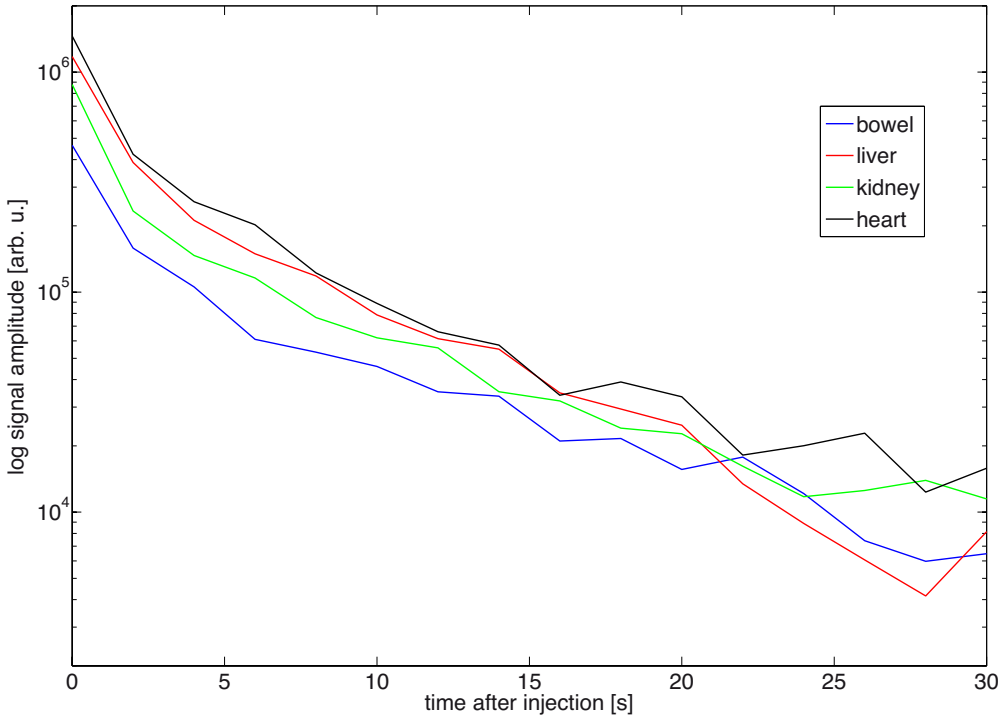

Figure 55: Intravascular ^{13}C-bicarbonate signal intensities for different *in vivo* cross sections. The vertical axis shows the signal intensities. The signal intensities exhibit different maximum values for each organ.

The determination of this T_1 decay was performed by using the highest intensity voxel at t = 0 s within the acquired intensity map (see Figure 53), which was assumed to be mainly intravascular because of the bolus. After the bicarbonate injection via the tail vein, a rapid decay of the hyperpolarized signal of the bicarbonate can be observed (Figure 56). Accordingly, this decay may occur owing to the bolus injection, which leads to a high intravascular bicarbonate concentration. This initial rapid decay is dominated by the fading of the bolus signal and hence is perfusion-dominated. Additional contributions to the signal decay are due to the diffusion and transport in the peripheral tissue, kidney filtration, and CO_2 conversion and exhalation.

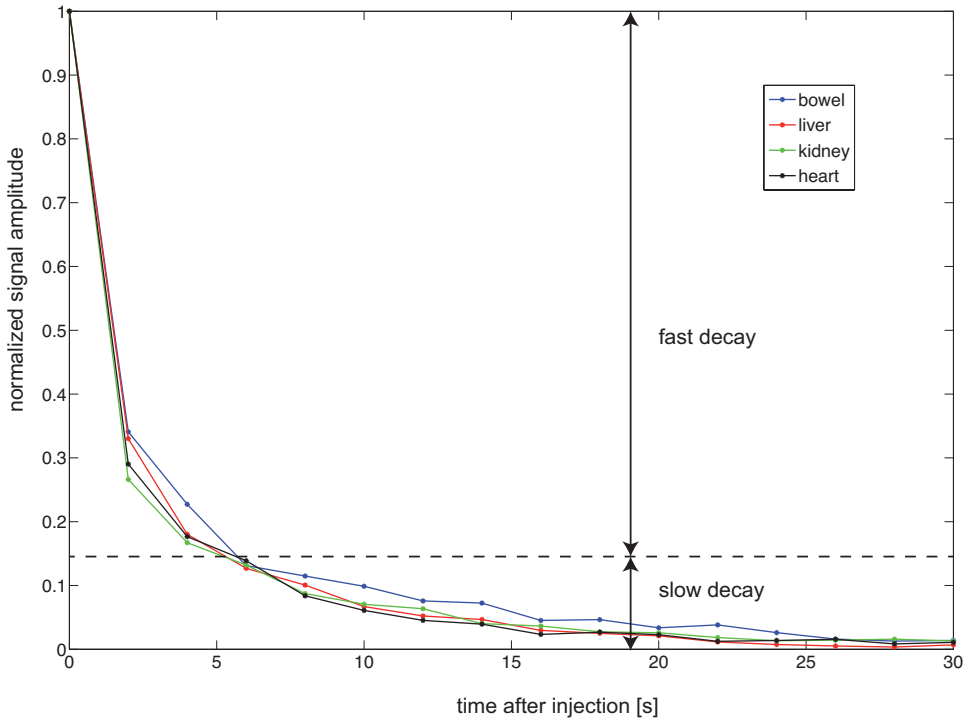

Figure 56: Intravascular ^{13}C-bicarbonate signal intensities for different *in vivo* cross sections. The vertical axis shows the signal intensities, normalized to the highest intensity at t = 0 s. The horizontal axis shows the time after the injection in seconds. After 6 s, 85% of the hyperpolarized signal has decayed (dotted line), which is comparable to an apparent T_1 of approximately 1 s. This region is dominated by bolus decay. Additional contribution to decay is owing to diffusion from intravascular into extravascular and intracellular regions. The remaining 15% of the signal decays with a T_1 of 10 s, which is the region that may be used for pH detection.

From this dataset, the bicarbonate perfusion equilibrated at around 6 s, reaching a steady state, after which the *in vivo* pH measurements should be performed. After the injection bolus has passed, the signal decayed with a T_1 of around 10 s for all cross sections (see Figure 57). These values are comparable with previously published *in vivo* values [53].

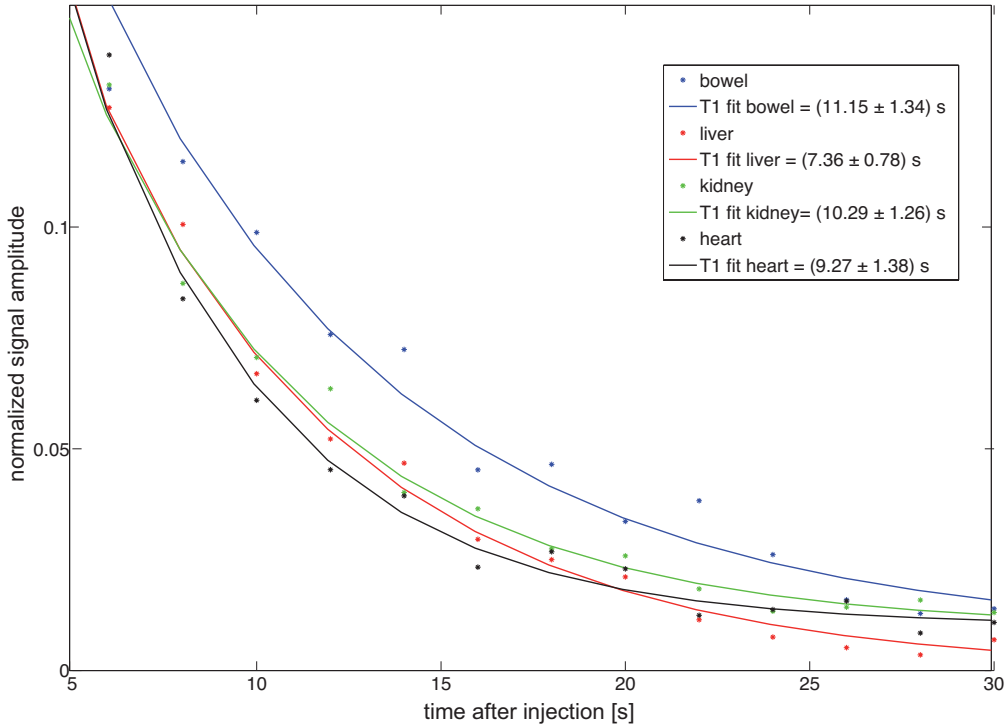

Figure 57: *In vivo* T_1-decay of ^{13}C-bicarbonate, measured for different organ cross sections in a healthy rat. The error was calculated using 95% confidence boundaries of the mono-exponential fit.

The overall SNR outside the *vena cava* (SNR_{ex}) was significantly smaller compared with the data, which were collected from inside the *vena cava* (SNR_{intr}): $SNR_{intr} \approx 27 \cdot SNR_{extr}$. The signal drops below the SNR limit after 14 s. After the bolus has passed, the signal decays with the same T_1 and could be divided into a fast, perfusion-dominated decay in the beginning and a non-perfusion-dominated T_1 decay after $8\,s$. Hence, most of the bicarbonate signal mainly originates from the blood vessels of the investigated tissue. This needs to be taken into account as an error source for pH determination experiments, which require pH estimation in the extravascular space for disorder characterization. The selection of a voxel, which originates from the extravascular space, led to a decay plot, displayed in Figure 58. The maximum bicarbonate signal was detected with a 2 s delay, which can be explained by the longer perfusion time from the *vena cava* to the smaller vessels.

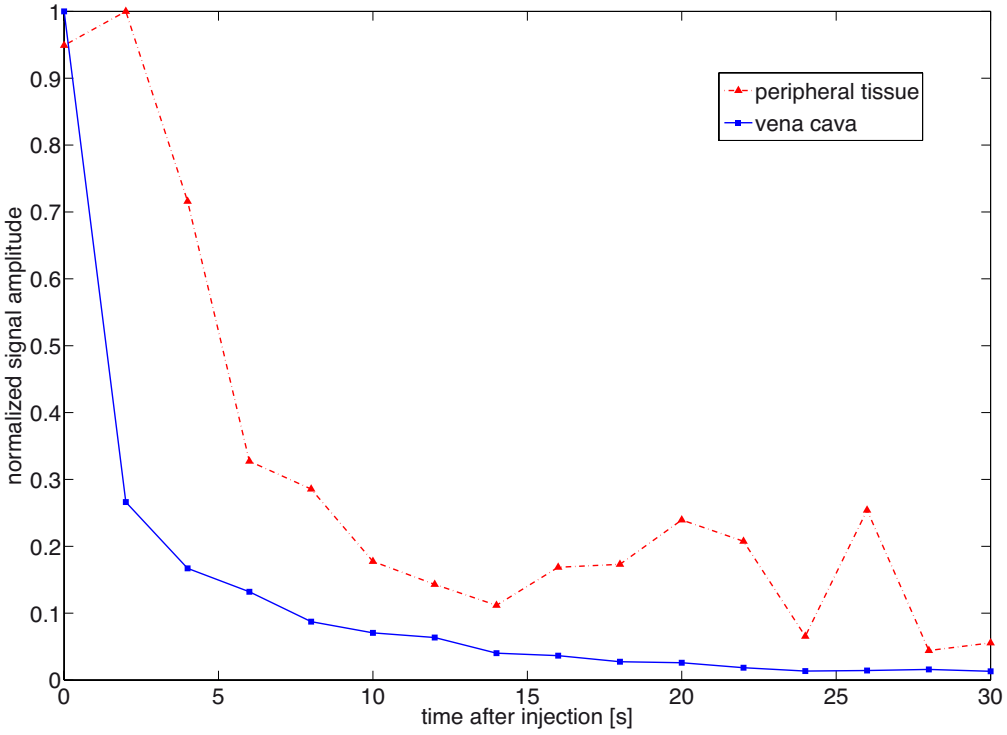

Figure 58: Voxel signal intensity analysis of a rat kidney slice of 10 mm. The figure depicts voxel intensities, positioned inside the *vena cava* (blue curve) and outside, in the peripheral tissue (red curve). The maximum signal is shifted by 2 s owing to perfusion of the hyperpolarized bicarbonate into smaller blood vessels.

4.4. pH quantification *in vivo* (diseases)

Finally, the successful *in vivo* parameter analysis allowed the investigation of pH changes for different diseases in comparison with the healthy state. pH changes of tumors were shown in the spectral domain (chapter 4.4.1) and pH imaging for acute metabolic alkalosis (chapter 4.4.2) and inflammation disease models (chapter 4.4.3) was performed in rats.

4.4.1 Tumor spectral

Cancer is one of the most investigated disorders worldwide. It has a large variety of phenotypes, affecting a broad range of organs. Investigations of tumors have been performed using different MR modalities [40,139,140]. The pH investigation of tumors is an expanding field of research, since pH functions as a key parameter in cancer biochemistry for extracellular cell matrix degradation, proliferation, angiogenesis, and treatment response [19,20,26,141]. Theoretical models support tumors' extracellular acidification [142], which is induced by an increased glycolytic activity of the carcinogenic cells [143]. Hence, it is a valuable target and the very first *in vivo* hyperpolarized ^{13}C bicarbonate imaging has been demonstrated in mouse lymphomas [53].

To investigate *in vivo* performance, spectral investigations were first performed on subcutaneous MATBIII tumors. 1 cm thick slices were measured to obtain hyperpolarized spectra from tumors and compared to spectra of healthy tissue (Figure 59).

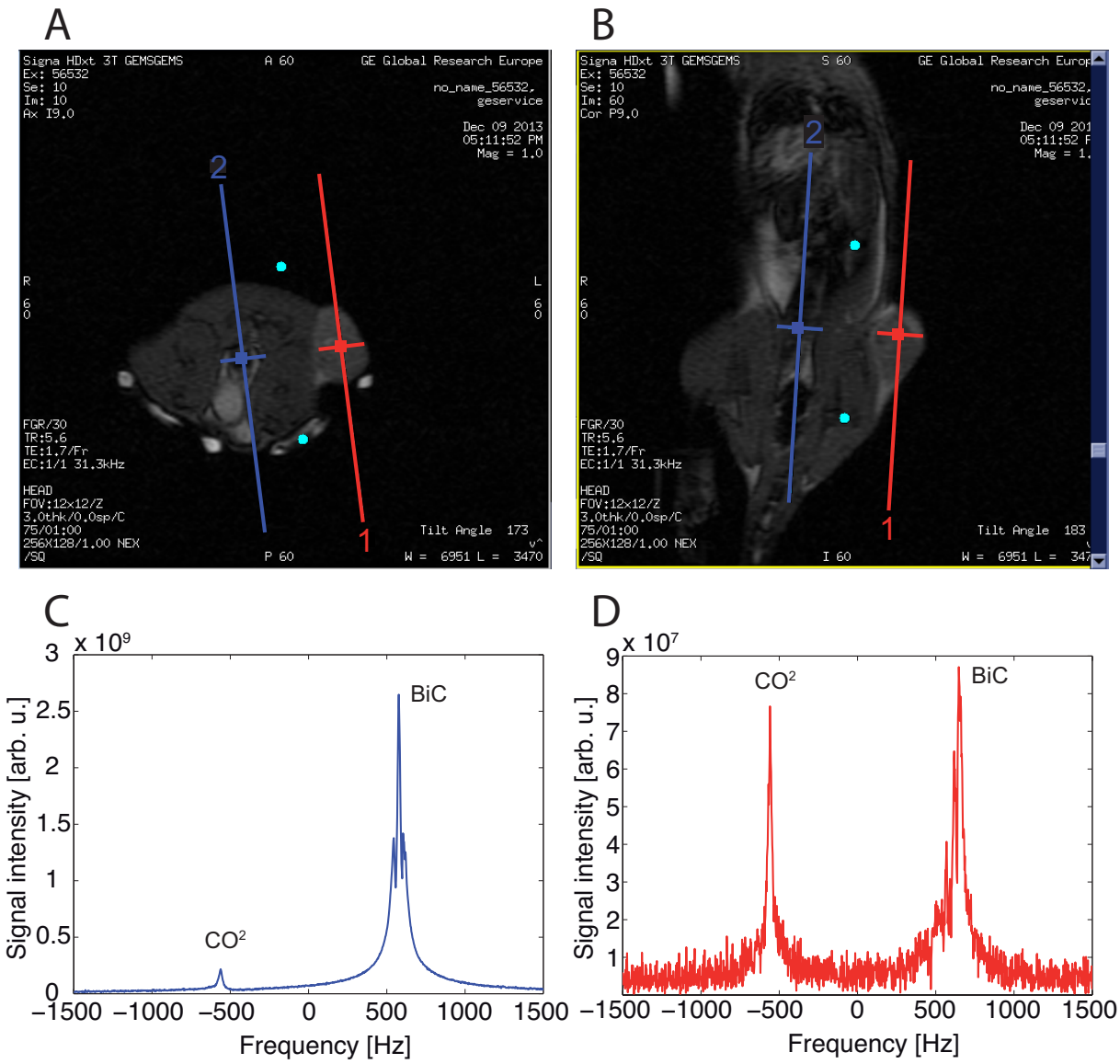

Figure 59: (A) Axial view (FRFSE proton map, FOV=12 cm, slice thickness=3 mm) of the MATBIII tumor-bearing rat. The subcutaneous tumor is clearly visible in the right leg of the rat. (B) A coronal view (FRFSE, FOV=12 cm, thick=3 mm) of the same rat. The ^{13}C slice positions are marked in blue and red. Slice 1 is positioned in a manner that only the tumor tissue is measured. Slice 2 is positioned through the whole rat, as a reference for the ^{13}C signal. The ^{13}C slices show a slice thickness of 1 cm, so that the entire tumor can be spectrally measured. The spectral ^{13}C acquisition was performed using a soft pulse excitation, centered between the bicarbonate and CO_2 resonances, with a slice thickness of 10.1 mm and a 90° flip angle. The spectra were acquired 10 s after injection. (C) The resulting spectrum for the entire rat slice, leading to a pH of 7.4, which equals literature values for blood pH. The bicarbonate shows a broadened appearance, as discussed in chapter 3.2.2.1, which occur when bicarbonate is dissolved in higher concentrations (>360 mmol/L). (D) The resulting spectrum for the tumor slice, showing a more acidic pH of 6.25.

It can clearly be seen that the subcutaneous MATBIII tumor showed acidic pH values, which are assumed to be extracellular. Subsequent pH imaging could not performed owing to the insufficient SNR of the CO_2.

4.4.2 Acute metabolic alkalosis

Homeostasis is crucial for any *in vivo* system, which is reflected in the abundance of acid-base regulating systems *in vivo* [144]. The regulation of any acid-base disorder is antagonized by changes in kidney filtration and breathing [145]. The excretion of acids and bases is one of the most important regulating mechanisms and is usually performed via kidney filtration. This fact, as well as their good perfusion and sufficient size, makes the kidneys valuable targets for hyperpolarized ^{13}C-bicarbonate pH mapping.

The filtration of the bicarbonate in the nephron lumen is nearly 100%. However, the body tries to preserve as much bicarbonate as possible and therefore, an effective resorption mechanism is needed to restore the bicarbonate into the blood. In a healthy system, the resorption of bicarbonate takes place in the proximal convoluted tubule of the nephron (see Figure 60).

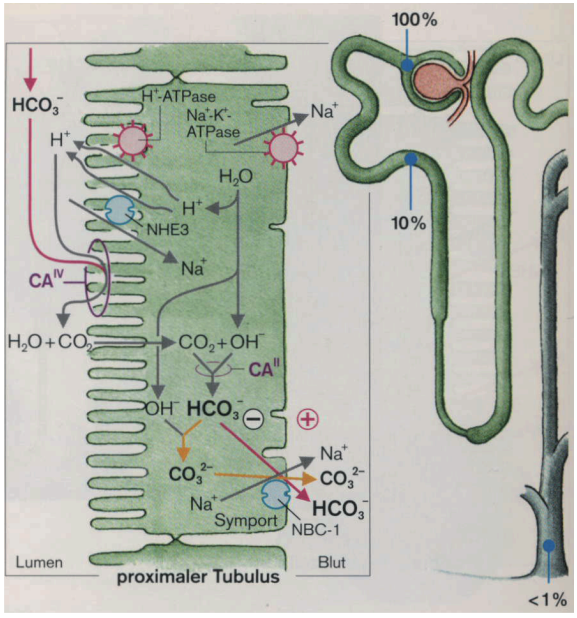

Figure 60: Scheme of biological bicarbonate filtration in the kidney nephron. On the right side, an overview of the nephron is presented, showing the concentrations of bicarbonate in the lumen. On the left side: Scheme of bicarbonate resorption mechanisms in the proximal tubule, leading to an almost complete bicarbonate resorption. Figure from [146].

The driving force of bicarbonate filtration is the secretion of H^+ in the proximal tubule. Membrane-bound CA IV leads to a fast conversion of the bicarbonate to H_2O and CO_2, which diffuses into the tubule cell. Here, cytoplasmic CA II results in conversion into bicarbonate again, which is transported back into the blood. This transfer occurs either by three bicarbonates being transported together with one Na^+ with a passive symport carrier NBC-1 or via the electrically neutral HCO_3^-/CO_2 antiporter. During alkalosis, H^+ secretion is reduced, resulting in a higher amount of bicarbonate remaining in the lumen of the nephron. Another regulating mechanism is exchanging cells that are a regulatory part of the H^+ secretion into the nephron lumen. At the alkaline metabolite state, the cells can secrete bicarbonate back into the lumen and simultaneously actively transport protons back into the blood via ATPase active transporters. This leads to an acidification of the blood and an

alkalization of the urine, which can show increased values of pH up to 8.2. Thus, blood pH is regulated to normal values again.

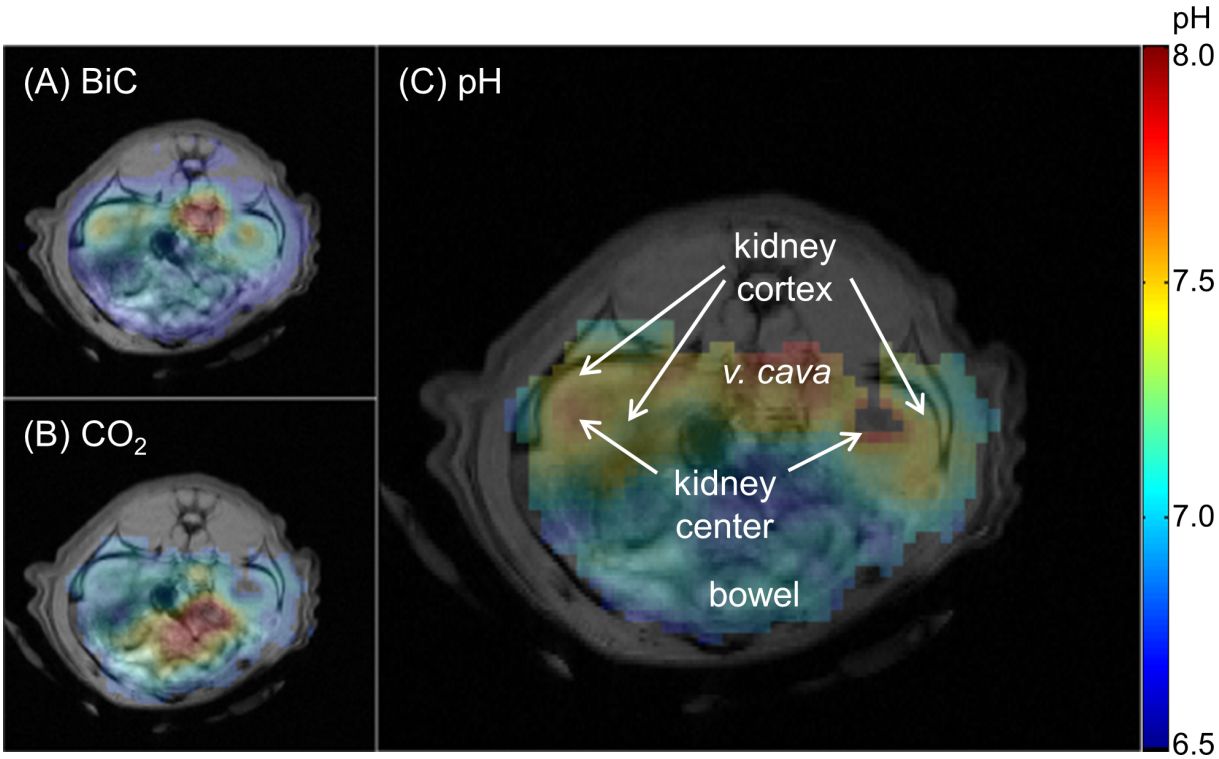

Figure 61: Healthy rat pH map (single SPSP excitation and spiral acquisition) of an axial kidney slice with a 10 mm slice thickness. (A) BiC signal. (B) CO_2 signal. BiC occured mainly in the *vena cava* and the center of the kidneys. CO_2 was mainly present in the cortex of the kidneys and the bowel region. (C) The resulting pH map with an increased pH of 7.5-7.7 in the *vena cava*, which is caused by BiC administration. The bowel region showed a low pH of around 7. The kidneys exhibited a pH gradient from the center (pH 7.5) to the cortex (pH 7.2). The ROI was estimated using ^{13}C signal intensity threshold masks for bicarbonate and CO_2. The pH map was masked by intersectional regions of the bicarbonate and CO_2 maps, both exceeding the signal thresholds. The signal intensity maps (figures A and B) of the bicarbonate and CO_2 were normalized to the highest signal intensity (dark red). The pH map (figure C) was scaled according to the color bar adjacent to the figure.

To assess the sensitivity and accuracy of SPSP spiral acquisition *in vivo*, healthy rats (n = 5) and animals with acute sterile inflammation (n = 4) were studied. Figure 61 depicts a representative dataset acquired in healthy Buffalo rats after an intravenous injection of hyperpolarized bicarbonate. Three slices were acquired (liver, kidney, and hind leg). In all slices, the *vena cava* exhibits the largest bicarbonate signal, followed by the well-perfused kidneys. In the kidney cortex, a high CO_2 accumulation is visible (see Figure 61 A), whereas the bicarbonate is more apparent in the hilum region of the kidney (see Figure 61 B). This particular distribution can be attributed to the bicarbonate filtration through the kidneys leading to a pH gradient that shows a pH decrease from center to cortex. The increased blood pH provides evidence of acute metabolic alkalosis. This conclusion is also supported by the observation of a reduced breathing rate directly after bicarbonate administration, which recovers to normal levels within 5 minutes. Owing to the reduced breathing, less CO_2 is exhaled and it remains in the blood. During acute metabolic alkalosis, the body tries to retain as much CO_2 as possible to regulate back to a blood pH of around 7.4.

4.4.3 Inflammation

Inflammation is the reaction of an *in vivo* system to harmful influences, such as biological, chemical, or physical damage. Acute inflammation is detectable by typical signs as swelling, reddening, and heating of the affected tissue. Diverse vascular changes occur during inflammation, induced by inflammatory mediators. One important effect is vasodilatation and, connected with it, hyperaemia. Certain groups of histamines, prostaglandins, and kinines increase the permeability of the cell membranes, leading to local blood stasis of the tissue. This effect allows different proteins, e.g., macrophages, to enter the inflamed region and start the cellular immune reaction to the threat. The inflammatory reaction results in increased hydrogen concentration and subsequently to a decreased pH in the inflamed region [147-150]. Acute sterile inflammation was induced at the right leg of the Buffalo rats with concanavalin A and was measured 2 h after induction, which was assumed to be the maximum achievable amount of inflammation, following the procedure described in [151]. After dissolution, a dose of 5 ml/kg of the dissolved bicarbonate solution was injected into the tail vein of Buffalo rats with acute sterile inflammation. The injection time was around 10 s and the average weight was 350 mg. Subsequent SPSP-spiral acquisition produced the bicarbonate and CO_2 maps, from which the corresponding pH map was derived (see Figure 62).

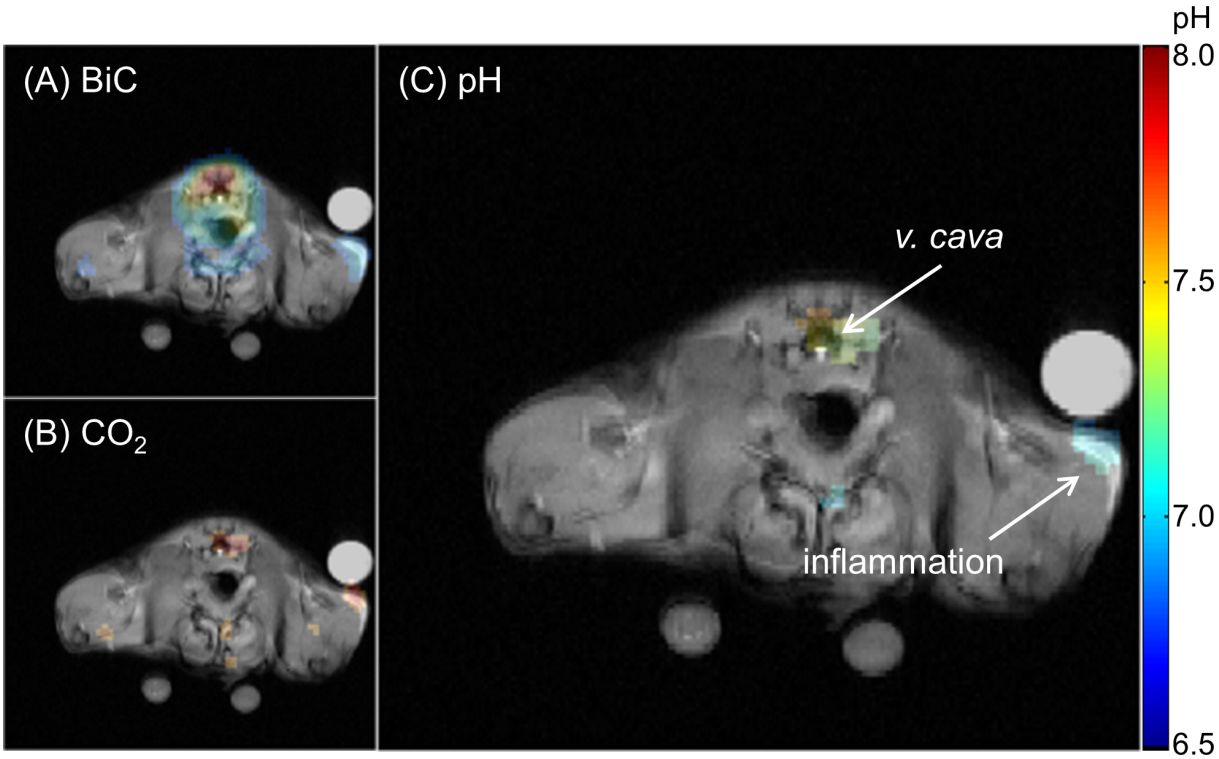

Figure 62: Inflammation induced in the right leg of a healthy rat, measured in an axial slice with 10 mm slice thickness and single SPSP excitation and spiral acquisition. (A) BiC signal. (B) CO_2 signal. The BiC concentration was high in the *vena cava* and at the inflamed tissue. The inflammation was clearly visible in gradient echo (GRE) proton images and confirmed by histological analysis. The *vena cava* showed a normal blood pH of 7.4. A lower pH of 7.0 was found in the inflamed tissue. The ROI was estimated using ^{13}C signal intensity threshold masks for bicarbonate and CO_2. The pH map was masked by intersectional regions of the bicarbonate and CO_2 maps, both exceeding the signal thresholds. The signal intensity maps (figures A and B) of the bicarbonate and CO_2 were normalized to the highest signal intensity (dark red). The pH map (figure C) was scaled according to the color bar adjacent to the figure.

Rats with induced sterile inflammation showed increased bicarbonate and CO_2 signals at the inflamed region. Decreased pH values were observed in the inflamed regions compared to the normal pH values in the *vena cava*.
To confirm the state of inflammation, histological analysis was performed and the results of staining are shown in Figure 63 and Figure 64.

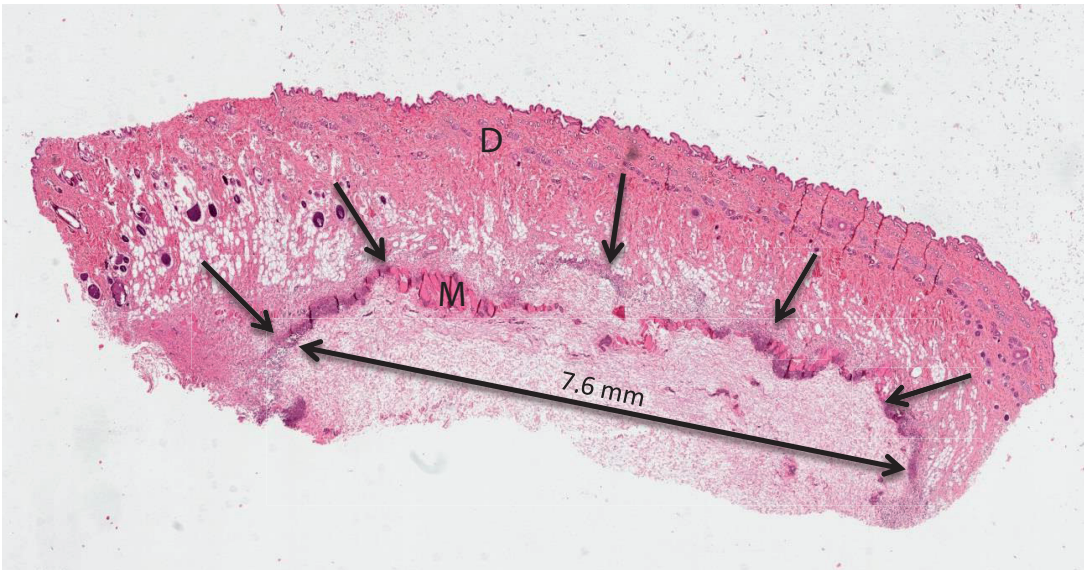

Figure 63: Immunohistological stain of a sterile subcutaneous inflammation, induced with concanavalin A, two hours after induction. Necrosis is demarcated with arrows. The epidermis and dermis (D) were unchanged. The inflammation started in the region of the panniculus muscle (M). The maximum diameter of the inflammational alteration was 7.6 mm.

The staining showed clear subcutaneous inflammations with a homogenous morphology with maximum diameters of 4.5 mm to 7.6 mm. The lesion spots showed central necrosis, predominantly in the state of lysis of collagen in the subcutaneous conjunctive tissue, which was confined by a predominantly mixed cell inflammation infiltration and edema. Inflammational alterations started in the region of the panniculus muscle and extended through the whole depth of the subcutaneous tissue to the subjacent muscle.

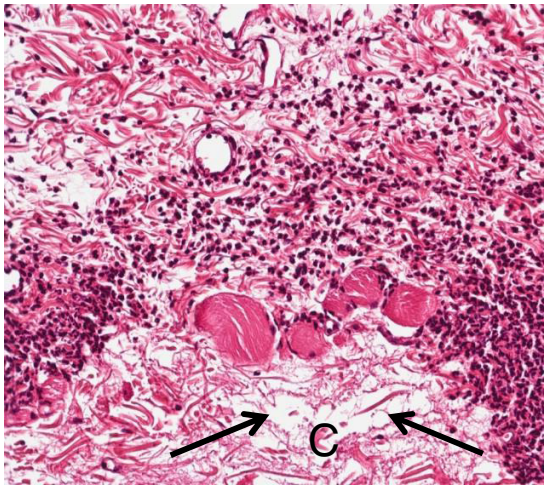

Figure 64: Enlarged view of the mixed cell infiltration at the transition from the hypodermis to subcutis after the induction of inflammation. Conjunctive tissue (C) with demarcated cell degradation (arrows).

5. Conclusions

In this work, the method of pH mapping with hyperpolarized bicarbonate was successfully optimized in terms of preparation and dissolution experimental parameters. The goal of this work was to increase the robustness of pH mapping with hyperpolarized ^{13}C-bicarbonate for subsequent *in vivo* application in different disorders that are influenced by alterations of pH. In comparison with earlier bicarbonate work, which focused more on the proof of concept, a detailed in-depth analysis of the method was performed, including parameter evaluations and assessment of inherent systematic errors, which have been so far overlooked.

5.1. Summary

The first aim of this work was the establishment and modification of the preparation and experimental execution procedure for ^{13}C-labeled bicarbonate. This included the successful verification of a synthesis procedure, investigations of different counter ions, and the influence of OXO63 radical and Gd (chapter 3.1). No systematic and detailed investigation of the preparation parameters has been published until now and it is missing from the current ^{13}C-bicarbonate research.

Additionally, the dissolution DNP procedure was analyzed in detail and subsequently optimized to achieve the best SNR (chapter 3.2) in order to provide a complete setup investigation. The principle and influence of filtration was introduced, which is not limited to the work on hyperpolarized bicarbonate, since most compounds use OXO radicals and/or ions of increased toxicity that must be removed. This resulted in an optimization of the preparation and the achievement of improved SNR and T_1 values for the hyperpolarized bicarbonate compared with those in previously published work. Most of the *in vitro* experiments performed in this work were aimed at signal preservation and SNR enhancement. Since cesium offers better properties for an increased concentration and polarization level, the optimization was performed for this counter ion. Because the characterization was performed with cesium, subsequent *in vivo* pH mapping was also performed with this ion. However, cesium is more toxic than sodium and, for subsequent clinical application, it would be preferable either to develop a method with a less toxic counter ion or establish filtration before injection as a standard procedure. The data analysis of SNR-dependent ROI estimation was successfully performed and implemented to improve the reliability of the acquired pH maps (chapter 3.3) compared with previously published work. The method was designed to obtain all required information from a single acquisition. If the boundary condition of a single data image used as the source of ROI is neglected, the design can be changed to obtain noise information by acquiring the ^{13}C signal at later time points or after crushing gradients, after all the hyperpolarized signal has decayed. This would lead to an improved noise level evaluation, since no artifact information is included in these images.

With the presented experimental procedure, high-SNR *in vitro* tests allowed to evaluate the bicarbonate signal and the pH-mapping performance at cell environments for multiple

changing parameters, e.g., varying field strengths and different pH environments. Furthermore, the first intensive sensitivity analysis of pH mapping was performed, which is essential for the evaluation of the method's performance and the estimation of its competitive capability compared with other pH-mapping modalities (chapter 4.1).
The validation of advanced pH-imaging methods, such as SPSP excitation with spiral readout, allows fast acquisition and signal-preserving conditions, where bicarbonate and CO_2 excitations can be adjusted separately (chapter 4.2). In contrast to other hyperpolarized work, where SNR-optimized imaging modalities are already used, advanced acquisition methods have not been established for ^{13}C-bicarbonate pH mapping before. A major advantage of using different flip angle excitation for each compound is the flexibility to modify the acquisitions for a specific organ or disease, when different excitation flip angles are needed to achieve optimum SNR conditions. Moreover, IDEAL frequency separation allowed the error estimation of the applied methods and resulting pH maps. The evaluation led to a detailed examination of the new method's performance, which was first presented in this work. In previously published work, imaging was performed with surface coils to ensure an increased SNR. In comparison, the increased SNR achieved in the present work due to the modifications of the experimental design allowed to use slice-selective volume coil acquisition and hence to investigate arbitrary volumetric slices of a rat.
The application of these advanced methods allowed the investigation of the *in vivo* perfusion behavior of the hyperpolarized ^{13}C-bicarbonate and organ-specific *in vivo* T_1 analysis, which has not been presented before (chapter 4.3).
Finally, significant pH changes could be demonstrated in tumors during acute metabolic alkalosis in the kidneys and in the case of induced sterile inflammation (chapter 4.4), which have not been shown before. The increased robustness of the method will provide the opportunity to apply pH mapping to other disorders influenced by pH changes, such as hypoxia and ischemia [152], for which the spatial pH evolution is unknown and might give significant additional information about organ condition during the progress of the disease.

5.2. Challenges

The method of hyperpolarized ^{13}C-bicarbonate pH mapping involves a concentration-independent pH marker, which is a major advantage against most of the other pH-imaging modalities. The concentration independence holds true for the case that sufficient bicarbonate and CO_2 signals are acquired. However, these signals undergo influences from different sources, which still tend to degrade the pH information. First of all, the signal is highly dependent of perfusion. Sufficient perfusion is necessary to transport the hyperpolarized bicarbonate to the target tissue, as for all hyperpolarized-labeled substances. Owing to systemic injections, more bicarbonate is located in the blood vessels and a certain spatial resolution is required to avoid overlapping of the vessels of the peripheral tissue within the acquired slice thickness of interest. This "mean" pH within the slice is highly dependent on the influence of tissue perfusion.

The administration of the OXO63 radical, as well as Gd and Cs, are all limitations for the application of the method to clinical work. Filtration of these compounds is necessary to achieve clinical translation.

One inherent problem of working with hyperpolarized substances using dissolution DNP is the reproducibility of the results. Since the method is based on one-shot experiments, comparing consecutively acquired experimental data is difficult. Multiple parameters of the experimental preparation and execution are error-prone and could influence the acquired data. The complexity of experiments increases even further when moving to *in vivo* experiments, as living systems bear a plethora of parameters that could change before, during, and after acquisition, which could change the final pH-mapping results. SPSP is highly sensitive to off-resonance and needs very good shimming and center frequency adjustment. Lost signal may not be recovered by reconstruction. This may limit the robustness of the technique. In hyperpolarized research, attempts have already been made, like uniform injections via an automated injection system and possible multiple injections with performed by a clinical polarizer (GE SpinLab), to reduce the variations during experiments and increase the reproducibility by performing multiple measurements with a single target.

Hyperpolarization is inherently limited to single- or few-shot acquisitions, since the signal decays fast ($T_1 \approx 10$ s) *in vivo* after injection. Hence, the method suffers a spatial resolution with voxel sizes of $5 \cdot 5 \cdot 10$ mm, compared with other pH-imaging modalities, e.g., CEST, where multiple excitations allow achieving higher SNRs and resolutions that are 100 times smaller. These limitations can be overcome by higher gradients and a stronger hyperpolarized signal. This can be achieved by higher polarizations and increased T_1, as demonstrated in this work. The above-mentioned boundaries limit the method's applicability to fairly large targets with diameters of >5 mm, like larger tumors or spots of inflammation. Furthermore, the heterogeneity within these targets cannot be determined, leading to an averaged signal and pH information over the entire voxel. This is a drawback, because tumors often show a heterogeneous occurrence [20]. On the other hand, compared to other methods, hyperpolarized ^{13}C-bicarbonate pH mapping uses a non-toxic labeled molecule and is applicable for clinical-field strengths and RF pulses, in contrast, e.g., to CEST. The time window of pH detection is inimitable, with a time frame of 0-120 s. This allows investigations of direct pH responses (e.g., after treatments) on a short time scale, which cannot be observed by any other method.

A major challenge in bicarbonate work is the absence of intracellular information (see chapter 4.1.2). Although the conditions of signal detection for the gradient-based diffusion of the bicarbonate to the intracellular space were sufficient, no intracellular signal could be determined. Previous published work argues that bicarbonate is mainly extracellular because of the short time scale in which pH is determined. However, many cellular bicarbonate-transporting mechanisms exist (see Figure 33) that allow the bicarbonate to traverse cell membrane. Furthermore, CO_2 is able to diffuse freely through membrane. Since carbonic anhydrases are also present in the intracellular space, it is likely that the conversion of CO_2 to bicarbonate will take place there. Because bicarbonate and CO_2 show different behavior of T_1

for different environments, there should be a non-negligible impact on the bicarbonate to CO_2 signal ratio.
As explained in chapter 2.2.4, carbonic anhydrases show different rate constants for different pH, which should influence the measured *in vivo* ratios of bicarbonate and CO_2. A reduced buildup constant at a very acidic environment, combined with a fast acquisition after injection, could lead to an incompletely established bicarbonate/CO_2 equilibrium and hence to false pH information.

5.3. Outlook

Although the method shows fairly good results *in vivo*, increasing the SNR remains one of the main challenges in increasing the rather rough spatial resolution. CO_2 detection, which is the obstacle in acquiring high-quality pH maps, is dependent on a high SNR and on any signal-preserving method, for example, improved acquisition techniques. This would also allow measuring the time evolution of the CO_2 distribution after injection.
An important task on the road to clinical application is the successful removal of any toxic compounds from the injection liquid, which can also have SNR-enhancing effects, as some compounds, like the OXO radical, exhibit increased T_1 relaxation.
One of the main drawbacks, compared to other pH-imaging methods, is the undetermined intracellular/extracellular signal contribution of bicarbonate and CO_2. Bicarbonate already shows sufficient SNR for a diffusion-based determination. This could provide an initial indication of how much of the hyperpolarized signal is intracellular. However, determining intracellular CO_2 will be rather more challenging, owing to the inherent low signal.
Further improvements and *in vivo* applications will facilitate the development of new concepts regarding the role of pH in diverse disorders and close the knowledge gap in the research on non-invasive clinical pH imaging in the future.

6. Appendix

6.1. pH error derivation

Inserting the values y = pH, x1 = signal of the bicarbonate = sig_BiC, x2 = signal of CO_2 = sig_CO_2, u_{x1}= uncertainty of the bicarbonate signal = u_{BiC}, u_{x2} = uncertainty of the CO_2 signal = u_{CO2}, the equation can be written as follows:

$$u_{pH} = \sqrt{\left(\frac{\partial pH}{\partial sig\_BiC} \cdot u_{BiC}\right)^2 + \left(\frac{\partial pH}{\partial sig\_CO2} \cdot u_{CO2}\right)^2} \quad (127)$$

where u_{pH} is the error for pH. Using the derivation of the Henderson-Hasselbalch equation for pH calculations:

$$pH = pKs + log_{10}\left(\frac{sig\_BiC}{sig\_CO2}\right) \quad (128)$$

leads to:

$$\frac{\partial pH}{\partial sig\_BiC} = \frac{\partial}{\partial sig\_BiC}\left(pKs + log_{10}\left(\frac{sig\_BiC}{sig\_CO2}\right)\right) \quad (129)$$

$$\frac{\partial pH}{\partial sig\_CO2} = \frac{\partial}{\partial sig\_CO2}\left(pKs + log_{10}\left(\frac{sig\_BiC}{sig\_CO2}\right)\right) \quad (130)$$

with:

$$log_{10}\left(\frac{sig_{BiC}}{sig_{CO2}}\right) = log_{10}(\mathrm{sig_{BiC}}) - \log_{10}(sig_{CO2}) \quad (131)$$

(129) and (130) become:

$$\frac{\partial pH}{\partial sig\_BiC} = \frac{\partial}{\partial sig\_BiC}(pKs + (log_{10}(\mathrm{sig_{BiC}}) - \log_{10}(sig_{CO2}))) \quad (132)$$

$$\frac{\partial pH}{\partial sig\_CO2} = \frac{\partial}{\partial sig\_CO2}(pKs + (log_{10}(\mathrm{sig_{BiC}}) - \log_{10}(sig_{CO2}))) \quad (133)$$

with $\log_a(x) = \frac{\ln(x)}{\ln(a)}$ and $\frac{d}{dx}\ln(x) = \frac{1}{x}$; (132) and (133) can be written as:

$$\frac{\partial pH}{\partial sig\_BiC} = \frac{1}{ln10 \cdot sig\_BiC} \quad (134)$$

$$\frac{\partial pH}{\partial sig\_CO2} = \frac{-1}{ln10 \cdot sig\_CO2} \quad (135)$$

Inserting equations (134) and (135) in equation (127) leads to the final equation (111).

6.2. Ethics approvals

The animal studies were approved by the local governmental committee for animal protection and welfare (Tierschutzbehörde, Regierung von Oberbayern) with respect to the ethics approvals AZ 55.2-1-54-2531-79-08 and AZ 55.2-1-54-2532-5-09.

References

1. Gerlach W, Stern O. Der experimentelle nachweis der richtungsquantelung im magnetfeld. Zeitschrift für Physik A Hadrons and Nuclei 1922;9(1):349-352.
2. Bloch F. Nuclear induction. Physical review 1946;70(7-8):460.
3. Purcell EM, Torrey H, Pound RV. Resonance absorption by nuclear magnetic moments in a solid. Physical review 1946;69(1-2):37.
4. Mansfield P, Grannell PK. NMR'diffraction'in solids? Journal of Physics C: solid state physics 1973;6(22):L422.
5. Lauterbur PC. Image formation by induced local interactions: examples employing nuclear magnetic resonance. Nature 1973;242(5394):190-191.
6. Haase A, Frahm J, Matthaei D, Hanicke W, Merboldt K-D. FLASH imaging. Rapid NMR imaging using low flip-angle pulses. Journal of Magnetic Resonance (1969) 1986;67(2):258-266.
7. Matthaei D, Frahm J, Haase A, Hanicke W. Regional physiological functions depicted by sequences of rapid magnetic resonance images. The Lancet 1985;326(8460):893.
8. Zhang S, Uecker M, Voit D, Merboldt K-D, Frahm J. Real-time cardiovascular magnetic resonance at high temporal resolution: radial FLASH with nonlinear inverse reconstruction. Journal of Cardiovascular Magnetic Resonance 2010;12(1):39.
9. Ogawa S, Lee TM, Nayak AS, Glynn P. Oxygenation‐sensitive contrast in magnetic resonance image of rodent brain at high magnetic fields. Magnetic resonance in medicine 1990;14(1):68-78.
10. Chaddock-Heyman L, Erickson KI, Voss MW, Knecht AM, Pontifex MB, Castelli DM, Hillman CH, Kramer AF. The effects of physical activity on functional MRI activation associated with cognitive control in children: a randomized controlled intervention. Frontiers in human neuroscience 2013;7:72.
11. Ardenkjaer-Larsen JH, Fridlund B, Gram A, Hansson G, Hansson L, Lerche MH, Servin R, Thaning M, Golman K. Increase in signal-to-noise ratio of > 10,000 times in liquid-state NMR. Proceedings of the National Academy of Sciences of the United States of America 2003;100(18):10158-10163.
12. Ardenkjaer-Larsen JH, Jóhannesson H, Petersson JS, Wolber J. Hyperpolarized molecules in solution. In vivo NMR Imaging: Springer; 2011. p 205-226.
13. Adrogué HJ, Madias NE. Management of life-threatening acid–base disorders. New England Journal of Medicine 1998;338(1):26-34.
14. Grinstein S, Swallow CJ, Rotstein OD. Regulation of cytoplasmic pH in phagocytic cell function and dysfunction. Clinical biochemistry 1991;24(3):241-247.
15. Vaupel P, Kallinowski F, Okunieff P. Blood flow, oxygen and nutrient supply, and metabolic microenvironment of human tumors: a review. Cancer research 1989;49(23):6449-6465.
16. Lardner A. The effects of extracellular pH on immune function. Journal of leukocyte biology 2001;69(4):522-530.
17. Warburg O. On the Origin of Cancer Cells. Science 1956;123(3191):309-314.
18. Gillies RJ, Raghunand N, Garcia-Martin ML, Gatenby RA. pH imaging. Engineering in Medicine and Biology Magazine, IEEE 2004;23(5):57-64.
19. Bhujwalla Z, Artemov D, Ballesteros P, Cerdan S, Gillies R, Solaiyappan M. Combined vascular and extracellular pH imaging of solid tumors. NMR in Biomedicine 2002;15(2):114-119.
20. Gillies RJ, Schornack PA, Secomb TW, Raghunand N. Causes and effects of heterogeneous perfusion in tumors. Neoplasia (New York, NY) 1999;1(3):197.
21. Stubbs M, Rodrigues L, Howe FA, Wang J, Jeong KS, Veech RL, Griffiths JR. Metabolic consequences of a reversed pH gradient in rat tumors. Cancer research 1994;54(15):4011-4016.
22. Rozhin J, Sameni M, Ziegler G, Sloane BF. Pericellular pH affects distribution and secretion of cathepsin B in malignant cells. Cancer research 1994;54(24):6517-6525.
23. Glunde K, Guggino SE, Solaiyappan M, Pathak AP, Ichikawa Y, Bhujwalla ZM. Extracellular acidification alters lysosomal trafficking in human breast cancer cells. Neoplasia (New York, NY) 2003;5(6):533.
24. Schornack PA, Gillies RJ. Contributions of cell metabolism and H+ diffusion to the acidic pH of tumors. Neoplasia (New York, NY) 2003;5(2):135.
25. Shi Q, Le X, Wang B, Abbruzzese JL, Xiong Q, He Y, Xie K. Regulation of vascular endothelial growth factor expression by acidosis in human cancer cells. Oncogene 2001;20(28):3751-3756.
26. Gatenby RA, Gawlinski ET, Gmitro AF, Kaylor B, Gillies RJ. Acid-mediated tumor invasion: a multidisciplinary study. Cancer research 2006;66(10):5216-5223.
27. Raghunand N, Gillies RJ. pH and drug resistance in tumors. Drug Resistance Updates 2000;3(1):39-47.
28. Izuishi K, Kato K, Ogura T, Kinoshita T, Esumi H. Remarkable tolerance of tumor cells to nutrient deprivation: possible new biochemical target for cancer therapy. Cancer research 2000;60(21):6201-6207.
29. Raghunand N, He X, Van Sluis R, Mahoney B, Baggett B, Taylor C, Paine-Murrieta G, Roe D, Bhujwalla Z, Gillies R. Enhancement of chemotherapy by manipulation of tumour pH. Br J Cancer 1999;80(7):1005.
30. Wike-Hooley JL, Haveman J, Reinhold HS. The relevance of tumour pH to the treatment of malignant disease. Radiotherapy and Oncology 1984;2(4):343-366.

31. Hassan M, Riley J, Chernomordik V, Smith P, Pursley R, Lee SB, Capala J, Gandjbakhche AH. Fluorescence lifetime imaging system for in vivo studies. Molecular imaging 2007;6(4):229.
32. Vāvere AL, Biddlecombe GB, Spees WM, Garbow JR, Wijesinghe D, Andreev OA, Engelman DM, Reshetnyak YK, Lewis JS. A novel technology for the imaging of acidic prostate tumors by positron emission tomography. Cancer research 2009;69(10):4510-4516.
33. Senda M, Alpert NM, Mackay BC, Buxton RB, Correia JA, Weise SB, Ackerman RH, Dorer D, Buonanno FS. Evaluation of the 11CO2 positron emission tomographic method for measuring brain pH. II. Quantitative pH mapping in patients with ischemic cerebrovascular diseases. Journal of Cerebral Blood Flow & Metabolism 1989;9(6):859-873.
34. Brooks D, Lammertsma A, Beaney R, Leenders K, Buckingham P, Marshall J, Jones T. Measurement of regional cerebral pH in human subjects using continuous inhalation of/sup 11/CO/sub 2/and positron emission tomography. J Cereb Blood Flow Metab;(United States) 1984;4(3).
35. Zhang X, Lin Y, Gillies RJ. Tumor pH and Its Measurement. Journal of Nuclear Medicine 2010;51(8):1167-1170.
36. Hashim AI, Zhang X, Wojtkowiak JW, Martinez GV, Gillies RJ. Imaging pH and metastasis. NMR in biomedicine 2011;24(6):582-591.
37. Mason RP. Transmembrane pH gradients in vivo: measurements using fluorinated vitamin B6 derivatives. Current medicinal chemistry 1999;6(6):481-500.
38. Stubbs M, Bhujwalla ZM, Tozer GM, Rodrigues LM, Maxwell RJ, Morgan R, Howe FA, Griffiths JR. An assessment of 31P MRS as a method of measuring pH in rat tumours. NMR in Biomedicine 1992;5(6):351-359.
39. Schroeder MA, Swietach P, Atherton HJ, Gallagher FA, Lee P, Radda GK, Clarke K, Tyler DJ. Measuring intracellular pH in the heart using hyperpolarized carbon dioxide and bicarbonate: a 13C and 31P magnetic resonance spectroscopy study. Cardiovascular Research 2010;86(1):82-91.
40. Gillies R, Liu Z, Bhujwalla Z. 31P-MRS measurements of extracellular pH of tumors using 3-aminopropylphosphonate. American Journal of Physiology-Cell Physiology 1994;267(1):C195-C203.
41. van Sluis R, Bhujwalla ZM, Raghunand N, Ballesteros P, Alvarez J, Cerdan S, Galons J-P, Gillies RJ. In vivo imaging of extracellular pH using 1 H MRSI. Magnetic resonance in medicine 1999;41(4):743-750.
42. García-Martín M-L, Hérigault G, Rémy C, Farion R, Ballesteros P, Coles JA, Cerdán S, Ziegler A. Mapping Extracellular pH in rat Brain Gliomas in vivo by H Magnetic Resonance Spectroscopic Imaging: Comparison with maps of metabolites. Cancer research 2001;61(17):6524-6531.
43. Raghunand N, Howison C, Sherry AD, Zhang S, Gillies RJ. Renal and systemic pH imaging by contrast‐enhanced MRI. Magnetic resonance in medicine 2003;49(2):249-257.
44. Raghunand N, Zhang S, Sherry AD, Gillies RJ. In vivo magnetic resonance imaging of tissue pH using a novel pH-sensitive contrast agent, GdDOTA-4AmP. Academic radiology 2002;9(2):S481-S483.
45. Garcia‐Martin ML, Martinez GV, Raghunand N, Sherry AD, Zhang S, Gillies RJ. High resolution pHe imaging of rat glioma using pH‐dependent relaxivity. Magnetic resonance in medicine 2006;55(2):309-315.
46. Martinez GV, Zhang X, García‐Martín ML, Morse DL, Woods M, Sherry AD, Gillies RJ. Imaging the extracellular pH of tumors by MRI after injection of a single cocktail of T1 and T2 contrast agents. NMR in Biomedicine 2011;24(10):1380-1391.
47. Castelli DD, Terreno E, Longo D, Aime S. Nanoparticle-based chemical exchange saturation transfer (CEST) agents. NMR Biomed 2013;26(7):839-849.
48. Castelli DD, Boffa C, Giustetto P, Terreno E, Aime S. Design and testing of paramagnetic liposome-based CEST agents for MRI visualization of payload release on pH-induced and ultrasound stimulation. Journal of biological inorganic chemistry : JBIC : a publication of the Society of Biological Inorganic Chemistry 2013.
49. Woods M, Woessner DE, Sherry AD. Paramagnetic lanthanide complexes as PARACEST agents for medical imaging. Chemical Society Reviews 2006;35.
50. Ward K, Balaban R. Determination of pH using water protons and chemical exchange dependent saturation transfer (CEST). Magnetic resonance in medicine 2000;44(5):799-802.
51. Delli Castelli D, Ferrauto G, Cutrin JC, Terreno E, Aime S. In vivo maps of extracellular pH in murine melanoma by CEST-MRI. Magnetic resonance in medicine : official journal of the Society of Magnetic Resonance in Medicine / Society of Magnetic Resonance in Medicine 2014;71(1):326-332.
52. Martin NK, Robey IF, Gaffney EA, Gillies RJ, Gatenby RA, Maini PK. Predicting the safety and efficacy of buffer therapy to raise tumour pHe: an integrative modelling study. Br J Cancer 2012;106(7):1280-1287.
53. Gallagher FA, Kettunen MI, Day SE, Hu D-E, Ardenkjaer-Larsen JH, Zandt Rit, Jensen PR, Karlsson M, Golman K, Lerche MH, Brindle KM. Magnetic resonance imaging of pH in vivo using hyperpolarized 13C-labelled bicarbonate. Nature 2008;453(7197):940-943.
54. Deane N, Smith HW. THE APPARENT FIRST DISSOCIATION CONSTANT, pK1', OF CARBONIC ACID IN THE HUMAN ERYTHROCYTE. Journal of Biological Chemistry 1957;227(1):101-106.
55. Gallagher FA, Kettunen MI, Brindle KM. Imaging pH with hyperpolarized 13C. NMR in Biomedicine 2011;24(8):1006-1015.
56. Wiesinger F, Weidl E, Menzel MI, Janich MA, Khegai O, Glaser SJ, Haase A, Schwaiger M, Schulte RF. IDEAL spiral CSI for dynamic metabolic MR imaging of hyperpolarized [1‐13C] pyruvate. Magnetic Resonance in Medicine 2012;68(1):8-16.
57. Schulte RF, Sperl JI, Weidl E, Menzel MI, Janich MA, Khegai O, Durst M, Ardenkjaer-Larsen JH, Glaser SJ, Haase A, Schwaiger M, Wiesinger F. Saturation-recovery metabolic-exchange rate imaging with hyperpolarized

[1-13C] pyruvate using spectral-spatial excitation. Magnetic resonance in medicine : official journal of the Society of Magnetic Resonance in Medicine / Society of Magnetic Resonance in Medicine 2013;69(5):1209-1216.
58. Twieg DB. The k‐trajectory formulation of the NMR imaging process with applications in analysis and synthesis of imaging methods. Medical Physics 1983;10(5):610-621.
59. Kumar A, Welti D, Ernst RR. NMR Fourier zeugmatography. Journal of Magnetic Resonance (1969) 1975;18(1):69-83.
60. Cooley JW, Tukey JW. An algorithm for the machine calculation of complex Fourier series. Mathematics of computation 1965;19(90):297-301.
61. Witte C, Schröder L. NMR of hyperpolarised probes. NMR in Biomedicine 2013;26(7):788-802.
62. Goodson BM. Nuclear magnetic resonance of laser-polarized noble gases in molecules, materials, and organisms. J Magn Reson 2002;155(2):157-216.
63. Walker TG, Happer W. Spin-exchange optical pumping of noble-gas nuclei. Reviews of Modern Physics 1997;69(2):629.
64. Oros A-M, Shah NJ. Hyperpolarized xenon in NMR and MRI. Physics in medicine and biology 2004;49(20):R105.
65. Schröder L, Lowery TJ, Hilty C, Wemmer DE, Pines A. Molecular imaging using a targeted magnetic resonance hyperpolarized biosensor. Science 2006;314(5798):446-449.
66. Schröder L, Meldrum T, Smith M, Lowery TJ, Wemmer DE, Pines A. Temperature Response of Xe 129 Depolarization Transfer and Its Application for Ultrasensitive NMR Detection. Physical review letters 2008;100(25):257603.
67. Schröder L, Chavez L, Meldrum T, Smith M, Lowery TJ, Wemmer DE, Pines A. Temperature‐Controlled Molecular Depolarization Gates in Nuclear Magnetic Resonance. Angewandte Chemie International Edition 2008;47(23):4316-4320.
68. Schilling F, Schröder L, Palaniappan KK, Zapf S, Wemmer DE, Pines A. MRI thermometry based on encapsulated hyperpolarized xenon. ChemPhysChem 2010;11(16):3529-3533.
69. Kunth M, Döpfert J, Witte C, Rossella F, Schröder L. Optimized use of reversible binding for fast and selective NMR localization of caged xenon. Angewandte Chemie International Edition 2012;51(33):8217-8220.
70. Bowers CR, Weitekamp DP. Nuclear magnetic resonance by measuring reaction yield of spin symmetry species. Solid state nuclear magnetic resonance 1998;11(1-2):123-128.
71. Natterer J, Bargon J. Parahydrogen induced polarization. Progress in Nuclear Magnetic Resonance Spectroscopy 1997;31(4):293-315.
72. Duckett SB, Mewis RE. Application of Para hydrogen Induced Polarization Techniques in NMR Spectroscopy and Imaging. Accounts of chemical research 2012;45(8):1247-1257.
73. Frossati G. Polarization of< sup> 3</sup> He, D< sub> 2</sub>(and possibly< sup> 129</sup> Xe) using cryogenic techniques. Nuclear Instruments and Methods in Physics Research Section A: Accelerators, Spectrometers, Detectors and Associated Equipment 1998;402(2):479-483.
74. Biškup N, Kalechofsky N, Candela D. Spin polarization of xenon films at low-temperature induced by 3He. Physica B: Condensed Matter 2003;329:437-438.
75. Abragam A, Goldman M. Principles of dynamic nuclear polarisation. Reports on Progress in Physics 1978;41(3):395.
76. Abragam A, Goldman M. Nuclear magnetism: order and disorder: Clarendon Press Oxford; 1982.
77. Overhauser AW. Polarization of nuclei in metals. Physical Review 1953;92(2):411.
78. Carver T, Slichter C. Polarization of nuclear spins in metals. Physical Review 1953;92(1):212.
79. Abragam A, Proctor W. Spin temperature. Physical Review 1958;109(5):1441.
80. Shimon D, Hovav Y, Feintuch A, Goldfarb D, Vega S. Dynamic nuclear polarization in the solid state: a transition between the cross effect and the solid effect. Physical Chemistry Chemical Physics 2012;14(16):5729-5743.
81. Serra SC, Rosso A, Tedoldi F. Electron and nuclear spin dynamics in the thermal mixing model of dynamic nuclear polarization. Physical Chemistry Chemical Physics 2012;14(38):13299-13308.
82. Golman K, Ardenkjær-Larsen JH, Petersson JS, Månsson S, Leunbach I. Molecular imaging with endogenous substances. Proceedings of the National Academy of Sciences 2003;100(18):10435-10439.
83. Golman K, Thaning M. Real-time metabolic imaging. Proceedings of the National Academy of Sciences 2006;103(30):11270-11275.
84. Day SE, Kettunen MI, Gallagher FA, Hu D-E, Lerche M, Wolber J, Golman K, Ardenkjaer-Larsen JH, Brindle KM. Detecting tumor response to treatment using hyperpolarized 13C magnetic resonance imaging and spectroscopy. Nature medicine 2007;13(11):1382-1387.
85. Merritt ME, Harrison C, Storey C, Jeffrey FM, Sherry AD, Malloy CR. Hyperpolarized 13C allows a direct measure of flux through a single enzyme-catalyzed step by NMR. Proceedings of the National Academy of Sciences 2007;104(50):19773-19777.
86. Schroeder MA, Cochlin LE, Heather LC, Clarke K, Radda GK, Tyler DJ. In vivo assessment of pyruvate dehydrogenase flux in the heart using hyperpolarized carbon-13 magnetic resonance. Proceedings of the National Academy of Sciences 2008;105(33):12051-12056.
87. Gallagher F, Kettunen M, Brindle K. Biomedical applications of hyperpolarized< sup> 13</sup> C magnetic resonance imaging. Progress in Nuclear Magnetic Resonance Spectroscopy 2009;55(4):285-295.
88. Gallagher FA, Kettunen MI, Hu D-E, Jensen PR, Karlsson M, Gisselsson A, Nelson SK, Witney TH, Bohndiek SE, Hansson G. Production of hyperpolarized [1, 4-13C2] malate from [1, 4-13C2] fumarate is a marker of cell

necrosis and treatment response in tumors. Proceedings of the National Academy of Sciences 2009;106(47):19801-19806.
89. Harris T, Eliyahu G, Frydman L, Degani H. Kinetics of hyperpolarized 13C1-pyruvate transport and metabolism in living human breast cancer cells. Proceedings of the National Academy of Sciences 2009;106(43):18131-18136.
90. Bohndiek SE, Kettunen MI, Hu D-e, Witney TH, Kennedy BW, Gallagher FA, Brindle KM. Detection of tumor response to a vascular disrupting agent by hyperpolarized 13C magnetic resonance spectroscopy. Molecular cancer therapeutics 2010;9(12):3278-3288.
91. Lau AZ, Chen AP, Ghugre NR, Ramanan V, Lam WW, Connelly KA, Wright GA, Cunningham CH. Rapid multislice imaging of hyperpolarized 13C pyruvate and bicarbonate in the heart. Magnetic resonance in medicine 2010;64(5):1323-1331.
92. Wilson DM, Keshari KR, Larson PEZ, Chen AP, Hu S, Criekinge MV, Bok R, Nelson SJ, Macdonald JM, Vigneron DB, others. Multi-compound polarization by DNP allows simultaneous assessment of multiple enzymatic activities in vivo. Journal of Magnetic Resonance 2010;205(1):141-147.
93. Witney T, Brindle K. Imaging tumour cell metabolism using hyperpolarized 13C magnetic resonance spectroscopy. Biochemical Society Transactions 2010;38(5):1220.
94. Brindle KM, Bohndiek SE, Gallagher FA, Kettunen MI. Tumor imaging using hyperpolarized 13C magnetic resonance spectroscopy. Magnetic Resonance in Medicine 2011;66(2):505-519.
95. von Morze C, Larson PE, Hu S, Keshari K, Wilson DM, Ardenkjaer‐Larsen JH, Goga A, Bok R, Kurhanewicz J, Vigneron DB. Imaging of blood flow using hyperpolarized [13C] urea in preclinical cancer models. Journal of Magnetic Resonance Imaging 2011;33(3):692-697.
96. Witney TH, Kettunen MI, Brindle KM. Kinetic modeling of hyperpolarized 13C label exchange between pyruvate and lactate in tumor cells. Journal of Biological Chemistry 2011;286(28):24572-24580.
97. Chen AP, Hurd RE, Schroeder MA, Lau AZ, Gu YP, Lam WW, Barry J, Tropp J, Cunningham CH. Simultaneous investigation of cardiac pyruvate dehydrogenase flux, Krebs cycle metabolism and pH, using hyperpolarized [1,2-(13)C2]pyruvate in vivo. NMR Biomed 2012;25(2):305-311.
98. Clatworthy MR, Kettunen MI, Hu D-E, Mathews RJ, Witney TH, Kennedy BW, Bohndiek SE, Gallagher FA, Jarvis LB, Smith KG. Magnetic resonance imaging with hyperpolarized [1, 4-13C2] fumarate allows detection of early renal acute tubular necrosis. Proceedings of the National Academy of Sciences 2012;109(33):13374-13379.
99. Schroeder MA, Atherton HJ, Dodd MS, Lee P, Cochlin LE, Radda GK, Clarke K, Tyler DJ. The Cycling of Acetyl-Coenzyme A Through Acetylcarnitine Buffers Cardiac Substrate Supply A Hyperpolarized 13C Magnetic Resonance Study. Circulation: Cardiovascular Imaging 2012;5(2):201-209.
100. Laustsen C, Østergaard JA, Lauritzen MH, Nørregaard R, Bowen S, Søgaard LV, Flyvbjerg A, Pedersen M, Ardenkjær‐Larsen JH. Assessment of early diabetic renal changes with hyperpolarized [1‐13C] pyruvate. Diabetes/metabolism research and reviews 2013;29(2):125-129.
101. Schroeder MA, Lau AZ, Chen AP, Gu Y, Nagendran J, Barry J, Hu X, Dyck JR, Tyler DJ, Clarke K. Hyperpolarized 13C magnetic resonance reveals early-and late-onset changes to in vivo pyruvate metabolism in the failing heart. European journal of heart failure 2013;15(2):130-140.
102. Eichhorn TR, Takado Y, Salameh N, Capozzi A, Cheng T, Hyacinthe J-N, Mishkovsky M, Roussel C, Comment A. Hyperpolarization without persistent radicals for in vivo real-time metabolic imaging. Proceedings of the National Academy of Sciences 2013.
103. Hu S, Lustig M, Chen AP, Crane J, Kerr A, Kelley DA, Hurd R, Kurhanewicz J, Nelson SJ, Pauly JM. Compressed sensing for resolution enhancement of hyperpolarized< sup> 13</sup> C flyback 3D-MRSI. Journal of magnetic resonance 2008;192(2):258-264.
104. Meyer CH, Pauly JM, Macovski A, Nishimura DG. Simultaneous spatial and spectral selective excitation. Magnetic resonance in medicine : official journal of the Society of Magnetic Resonance in Medicine / Society of Magnetic Resonance in Medicine 1990;15(2):287-304.
105. Lau AZ, Chen AP, Hurd RE, Cunningham CH. Spectral–spatial excitation for rapid imaging of DNP compounds. NMR in Biomedicine 2011;24(8):988-996.
106. Dixon WT. Simple proton spectroscopic imaging. Radiology 1984;153(1):189-194.
107. Costa DN, Pedrosa I, McKenzie C, Reeder SB, Rofsky NM. Body MRI Using IDEAL. American Journal of Roentgenology 2008;190(4):1076-1084.
108. Bandura AV, Lvov SN. The ionization constant of water over wide ranges of temperature and density. Journal of physical and chemical reference data 2005;35(1):15-30.
109. Mortimer CE, Müller U. Chemie das Basiswissen der Chemie ; 520 Formelbilder, 125 Tabellen. Stuttgart: Thieme; 2003. XVIII, 766 S. p.
110. Otto M. Analytische Chemie. Weinheim: Wiley-VCH; 2006. XXIII, 733 S. p.
111. Kapitel 10 - Elektrochemie im Gleichgewicht. In: Atkins PW, Höpfner A, Schleitzer A, editors. Physikalische Chemie. 3., korrigierte Aufl., 1. Nachdr ed. Weinheim [u.a.]: Wiley-VCH; 2004. p XXIII, 1106 S.
112. Weast RC. Handbook of chemistry and physics : a ready reference book of chemical and physical data, 1981-1982. Boca Raton: CRC press; 1981.
113. Kapitel 8 - Enzyme: Grundlegende Konzepte und Kinetik. In: Berg JM, Tymoczko JL, Stryer L, Gatto GJ, editors. Biochemie. 7. Aufl. ed. Berlin [u.a.]: Springer Spektrum; 2013. p XLI, 1196 S.
114. Kapitel 9 - Katalytische Strategien. In: Berg JM, Tymoczko JL, Stryer L, Gatto GJ, editors. Biochemie. 7. Aufl. ed. Berlin [u.a.]: Springer Spektrum; 2013. p XLI, 1196 S.

115. Khalifah RG. The carbon dioxide hydration activity of carbonic anhydrase I. Stop-flow kinetic studies on the native human isoenzymes B and C. Journal of Biological Chemistry 1971;246(8):2561-2573.
116. Eigen M, Kruse W, Maass G, De Maeyer L, Porter G. Progress in Reaction Kinetics. G Porter, ed 1964;2:287.
117. Gibbons BH, Edsall JT. Rate of Hydration of Carbon Dioxide and Dehydration of Carbonic Acid at 25 Degrees. The Journal of biological chemistry 1963;238:3502-3507.
118. Supuran CT. Carbonic anhydrases: novel therapeutic applications for inhibitors and activators. Nat Rev Drug Discov 2008;7(2):168-181.
119. Hilvo M, Baranauskiene L, Salzano AM, Scaloni A, Matulis D, Innocenti A, Scozzafava A, Monti SM, Di Fiore A, De Simone G. Biochemical characterization of CA IX, one of the most active carbonic anhydrase isozymes. Journal of Biological Chemistry 2008;283(41):27799-27809.
120. (NIST) MSDotNIoSaT. Volume 2014.
121. ECHA ECA-. Volume 2014.
122. Kapitel 2 - Der erste Hauptsatz: Grundlagen. In: Atkins PW, Höpfner A, Schleitzer A, editors. Physikalische Chemie. 3., korrigierte Aufl., 1. Nachdr ed. Weinheim [u.a.]: Wiley-VCH; 2004. p XXIII, 1106 S.
123. Simons EL, Cairns EJ, Sangermano LD. Purification and preparation of some caesium compounds. Talanta 1966;13(2):199-204.
124. Ellis KJ, Morrison JF. Buffers of constant ionic strength for studying pH-dependent processes. Methods in enzymology 1981;87:405-426.
125. Miéville P, Ahuja P, Sarkar R, Jannin S, Vasos PR, Gerber‐Lemaire S, Mishkovsky M, Comment A, Gruetter R, Ouari O. Scavenging free radicals to preserve enhancement and extend relaxation times in NMR using dynamic nuclear polarization. Angewandte Chemie 2010;122(35):6318-6321.
126. Davis D, Murphy E, London R. Uptake of cesium ions by human erythrocytes and perfused rat heart: a cesium-133 NMR study. Biochemistry 1988;27(10):3547-3551.
127. Yilmaz A, Yurdakoc M, Işik B. Influence of transition metal ions on NMR proton T1 relaxation times of serum, blood, and red cells. Biological trace element research 1999;67(2):187-193.
128. Merck. MSDS. 2013.
129. Scholz DJ. Quantitative pH analysis with sodium 13C-Bicarbonate at small pH variations. Proceedings ESMRMB, 2012; Lisbon.
130. Scholz DJ, Janich MA, Köllisch U, Schulte RF, Ardenkjaer‐Larsen JH, Frank A, Haase A, Schwaiger M, Menzel MI. Quantified pH imaging with hyperpolarized 13C‐bicarbonate. Magnetic Resonance in Medicine 2014, DOI: 10.1002/mrm.25357
131. Schilling F, Duwel S, Kollisch U, Durst M, Schulte RF, Glaser SJ, Haase A, Otto AM, Menzel MI. Diffusion of hyperpolarized (13) C-metabolites in tumor cell spheroids using real-time NMR spectroscopy. NMR Biomed 2013;26(5):557-568.
132. Sogaard LV, Schilling F, Janich MA, Menzel MI, Ardenkjaer-Larsen JH. In vivo measurement of apparent diffusion coefficients of hyperpolarized (13) C-labeled metabolites. NMR Biomed 2014;27(5):561-569.
133. e.V. DIfN. Fundamentals of metrology - Part 4: Evaluation of measurements; uncertainty of measurement. Volume DIN 1319-41999.
134. Naressi A, Couturier C, Castang I, De Beer R, Graveron-Demilly D. Java-based graphical user interface for MRUI, a software package for quantitation of in vivo/medical magnetic resonance spectroscopy signals. Computers in biology and medicine 2001;31(4):269-286.
135. Reeder SB, Brittain JH, Grist TM, Yen YF. Least‐squares chemical shift separation for 13C metabolic imaging. Journal of Magnetic Resonance Imaging 2007;26(4):1145-1152.
136. Levin Y, Mayer D, Yen YF, Hurd R, Spielman D. Optimization of fast spiral chemical shift imaging using least squares reconstruction: application for hyperpolarized 13C metabolic imaging. Magnetic Resonance in Medicine 2007;58(2):245-252.
137. Kapitel 7 - Die Eigenschaften einfacher Mischungen. In: Atkins PW, Höpfner A, Schleitzer A, editors. Physikalische Chemie. 3., korrigierte Aufl., 1. Nachdr ed. Weinheim [u.a.]: Wiley-VCH; 2004. p XXIII, 1106 S.
138. Häussinger D. Liver regulation of acid-base balance. Mineral and electrolyte metabolism 1996;23(3-6):249-252.
139. Gillies RJ, Morse DL. In vivo magnetic resonance spectroscopy in cancer. Annu Rev Biomed Eng 2005;7:287-326.
140. Kettunen MI, Hu DE, Witney TH, McLaughlin R, Gallagher FA, Bohndiek SE, Day SE, Brindle KM. Magnetization transfer measurements of exchange between hyperpolarized [1-13C]pyruvate and [1-13C]lactate in a murine lymphoma. Magnetic resonance in medicine : official journal of the Society of Magnetic Resonance in Medicine / Society of Magnetic Resonance in Medicine 2010;63(4):872-880.
141. Gillies RJ, Robey I, Gatenby RA. Causes and consequences of increased glucose metabolism of cancers. Journal of Nuclear Medicine 2008;49(Suppl 2):24S-42S.
142. Martin NK, Gaffney EA, Gatenby RA, Gillies RJ, Robey IF, Maini PK. A mathematical model of tumour and blood pHe regulation: The HCO3-/CO2 buffering system. Mathematical biosciences 2011;230(1):1-11.
143. Gatenby RA, Gillies RJ. Why do cancers have high aerobic glycolysis? Nature Reviews Cancer 2004;4(11):891-899.
144. Adrogue HE, Adrogue HJ. Acid-base physiology. Respiratory care 2001;46(4):328-341.
145. Worthley LI. Hydrogen ion metabolism. Anaesth Intensive Care 1977;5(4):347-360.
146. Die Funktion der Nieren. In: Klinke R, Pape H-C, Silbernagl S, editors. Physiologie. 5., komplett überarb. Aufl. ed. Stuttgart [u.a.]: Thieme; 2005. p 325-376.

147. Steen KH, Steen AE, Reeh PW. A dominant role of acid pH in inflammatory excitation and sensitization of nociceptors in rat skin, in vitro. The Journal of neuroscience 1995;15(5):3982-3989.
148. Häbler P-DDC. Über den K-und Ca-gehalt von eiter und exsudaten und seine beziehungen zum entzündungsschmerz. Klinische Wochenschrift 1929;8(34):1569-1572.
149. Revici E, Stoopen E, Frenk E, Ravich RA. The painful focus. II. The relation of pain to local physiochemical changes. Bull Inst Appl Biol 1949;1(2):1.
150. Jacobus WE, Taylor GJ, HOLLIS DP, NUNNALLY RL. Phosphorus nuclear magnetic resonance of perfused working rat hearts. 1977.
151. Colditz IG, Cybulsky MI. Some characteristics of inflammation induced by muramyl dipeptide, endotoxin, and concanavalin A. Inflammation 1987;11(1):1-11.
152. Merritt ME, Harrison C, Storey C, Sherry AD, Malloy CR. Inhibition of carbohydrate oxidation during the first minute of reperfusion after brief ischemia: NMR detection of hyperpolarized 13CO2 and H13CO 3−. Magnetic Resonance in Medicine 2008;60(5):1029-1036.

List of publications

Journals

D. J. Scholz, M. A. Janich, U. Köllisch, R. F. Schulte, J. H. Ardenkjaer-Larsen, A. Frank, A. Haase, M. Schwaiger, M. I. Menzel. *Quantified pH Imaging with Hyperpolarized ^{13}C-Bicarbonate.* Magnetic Resonance in Medicine 2014, DOI: 10.1002/mrm.25357

D. J. Scholz, A. M. Otto, J. Hintermair, F. Schilling, A. Frank, U. Köllisch, M. A. Janich, R. F. Schulte, M. Schwaiger, A. Haase, M. I. Menzel. *Parameterization of hyperpolarized ^{13}C-bicarbonate-dissolution dynamic nuclear polarization.* Magnetic Resonance Materials in Physics, Biology and Medicine, under revision

Conference Proceedings

D. J. Scholz, M. A. Janich, A. Frank, U. Köllisch, J. H. Ardenkjaer-Larsen, R. F. Schulte, M. Schwaiger, A. Haase, M. I. Menzel *Quantified pH imaging with hyperpolarized ^{13}C-bicarbonate*, "magna cum laude" awarded oral presentation at Joint Annual Meeting of the International Society for Magnetic Resonance in Medicine – ISMRM and the European Society for Magnetic Resonance in Medicine and Biology – ESMRMB, Milan, Italy, 2014

D. J. Scholz, M. A. Janich, M. I. Menzel, A. Haase. *Quantified pH detection with hyperpolarized ^{13}C-bicarbonate*, oral presentation at 4th Annual Meeting of the International Society for Proton Dynamics in Cancer – ISPDC, Garching, Germany, 2013

D. J. Scholz, O. Khegai, A. Otto, R. F. Schulte, M. Schwaiger, S. Ziegler, A. Haase, M. I. Menzel. *Quantitative pH analysis with sodium ^{13}C-Bicarbonate at small pH variations*, traditional poster presentation at 29th Annual Scientific Meeting of the European Society for Magnetic Resonance in medicine and Biology – ESMRMB, Lisbon, Portugal, and at the 1st International Kick-Off Meeting by the BMBF consortium German Medical Imaging in Motion – GMIM, Johns Hopkins University, Baltimore, USA, 2012

D. J. Scholz, M. Schwaiger, A. Haase, M. I. Menzel. *Quantitative spectral pH-detection in vivo via ^{13}C*, oral presentation at 3rd GSISH Colloquium on Biomedical Imaging, Klinikum rechts der Isar, Garching, Germany, 2012

D. J. Scholz, S. Ziegler, A. Haase, M. I. Menzel. *pH-detection with ^{13}C-bicarbonate*, oral presentation at Molecular Biotechnology Center – MBC, Turin, Italy, 2011

D. J. Scholz, O. Khegai, E. Kubala, A. Otto, M. Schwaiger, R. F. Schulte, A. Haase, M. I. Menzel. *Hyperpolarization of ^{13}C-bicarbonate for spatial MRI pH-detection*, oral presentation at 2nd Annual Meeting of the International Society for Proton Dynamics in Cancer – ISPDC, Nice, France, 2011

D. J. Scholz. *Quantitative pH-detection in vivo via ^{13}C magnetic resonance*, oral presentation at 1st GSISH Colloquium on Biomedical Imaging, Klinikum rechts der Isar, Munich, Germany, 2011

Acknowledgements

Starting from the scratch, overcoming all the challenges of elaborating a PhD in a new environment would have never successfully happened without amazing support from many sides. Here I gratefully would like to thank all the people that supported me during the thesis, inside the lab and outside:

- *Prof. Dr. Axel Haase* for his motivation from the beginning and support and trust throughout the years as my scientific supervisor.

- *Dr. Marion Menzel* for all the effort and always constructive in-depth feedback, which made this work possible.

- *Dr. Martin Janich* for his diligent and intensive feedback throughout a year and later on.

- *Dr. Rolf Schulte* for his help and efforts in explaining challenging MR techniques.

- *Dr. Timo Schirmer* for supplying a great working environment at the GEGRC.

- *Dr. Angela Otto* and *Joseph Hintermair* for their valuable support at biological questions.

- *Prof. Dr. Sibylle Ziegler*, *Prof. Dr. Markus Schwaiger*, *Annette Frank* and all the other people from Klinikum rechts der Isar for their *"in vivo* support".

- *Prof. Dr. Jan Henrik Ardenkjaer-Larsen* and *Dr. Sean Bowen* for their support and kindness during my stay in Denmark.

- *Ursula, Katharina* and *Petra* for all-embracing support of the GSISH over the years and the opportunity to explore fruitful discussions all over the world.

- *Franz, Marika, Alex, Stephan* and *Concetta* for being great colleagues inside and outside the office at the IMETUM and GRC.

- *Uli, Markus* and *Tim* for having exciting meetings.

- All the people of the GEGRC and the IMETUM for the friendly working atmosphere.

- *Tom* not only for being a great colleague but also a karaoke partner meeting japanese standards and for exploring Tokyo, New York, Nornhm and the Isar.

- My parents *Uli* und *Martina* for their unconditional love and support from the school cone to the mortarboard.

- *Peggy* simply for brightening my life.

Furthermore I would like to acknowledge all the financial and material support I received from the GSISH, GEGRC, IMETUM and BMBF (Grant # 13EZ1114).